EFFECTS OF COMPRESSOR ENDWALL SUCTION AND BLOWING ON STABILITY ENHANCEMENT

by

Norman K.W. Lee

GTL Report No. 192 January 1988

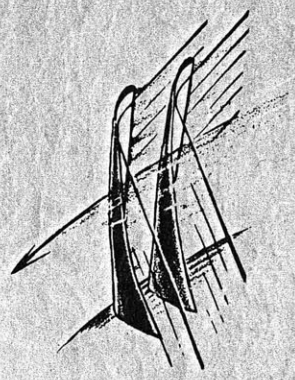

GAS TURBINE LABORATORY
MASSACHUSETTS INSTITUTE OF TECHNOLOGY
CAMBRIDGE, MASSACHUSETTS

EFFECTS OF COMPRESSOR ENDWALL SUCTION AND BLOWING ON STABILITY ENHANCEMENT

by

Norman K.W. Lee

GTL Report No. 192 January 1988

Research supported by Allison Gas Turbine Division of General Motors, Dr. A.K. Sehra project monitor, and by the Air Force Office of Scientific Research under contract F49-620-85-C-0018, Dr. J.D. Wilson program monitor.

ABSTRACT

An experimental investigation was carried out to examine the effects on stall margin of flow injection into, and removal out of, the endwall region of an axial compressor blade row. A main goal was to identify the mechanism by which wall treatment suppresses stall in turbomachines. To simulate the relative motion between blade and treatment, the injection and removal took place through a slotted hub rotating beneath a cantilevered stator row. Overall performance data and detailed (time-averaged) flowfield measurements were obtained.

Both injection and removal increased the stalling pressure rise, but neither was as effective as the complete treatment. This implies that removal of high blockage flow is not the only reason behind the observed stall margin improvement in a casing or hub treatment, and that injection also contributes to stall suppression. The results also indicated that, for a given variation of injection, the increase in stall pressure rise is linked to the streamwise momentum of the injected flow.

ACKNOWLEDGEMENTS

I wish to express my gratitude to Prof. E.M. Greitzer for his encouragement, guidance and support in all phases of the project, not to mention his patience in going through the never-ending drafts of this thesis. His vigorous approach in solving problems has also made an impact on me in the past two years.

I am very much indebted to P.L. Lavrich for his advice and help in areas ranging from the development of software to the use of hot wire anemometry. The time he spent in solving my problems is much appreciated. I am also grateful to D.A. Fink for his help in the laboratory, and also the permission to use his steam ejector calibration data. The efforts of R. Andrews, V. Dubrowski, J. Lewis and J. Nash in the mechanical aspects of the project are also appreciated.

Special thanks are extended to Dr. C.S. Tan for his valuable insights, especially in the area of classical aerodynamics which I consider a work of art.

This work was supported by Allison Gas Turbine Division of General Motors, Dr. A.K. Sehra, project monitor, and by the Air Force Office of Scientific Research, Dr. J.D. Wilson, program monitor. This support is gratefully acknowledged.

This program would never have been completed without the prayer support and encouragement from members of the Boston Chinese Bible Study Group and the Boston Chinese Evangelical Church. To them I express my gratitude. Finally, I wish to dedicate this thesis to my parents who sacrificed much in giving me the opportunity to see more of the world.

TABLE OF CONTENTS

TABLE OF CONTENTS (Cont.)

LIST OF TABLES

LIST OF FIGURES

LIST OF FIGURES (Cont.)

NOMENCLATURE

Chapters 1.0 - 6.0

A_{op}	Area of orifice
B	Ratio of orifice area to duct area
$\underline{C_x}$	Axial velocity at stator inlet
C_x	Average axial velocity through compressor
DP	Static pressure rise across stator
$\dot{m}$	Mass flow rate through orifice
U	Mean blade speed of rotor
$\underline{V}_{in}$	Stator inlet velocity
V_{in}	Mean stator inlet velocity
α_d	Discharge coefficient of orifice
$\underline{\beta}_{in}$	Stator inlet angle
β_{in}	Mean stator inlet angle
ΔP	Static pressure drop across orifice
ρ	Density of air

Appendix A

$\underline{A}$	Area per stator passage perpendicular to compressor axis
C_x/U	Flow coefficient as defined in Chapters 1.0 - 6.0
DP	Difference between inlet and exit pressures
G	Angle between velocity and compressor axis
$\dot{m}$	Mass flow rate into a stator passage
P	Pressure
s	Endwall suction rate per stator passage as a fraction of $\dot{m}$
V	Velocity
ρ	Density

Subscripts

1	Stator inlet
2	Stator exit without suction
2'	Stator exit with suction

Appendix B

For diffuser model:

A	Area normal to velocity
b	Ratio of injection rate to mass flow rate at inlet
$\dot{m}_j$	Mass injection rate
P	Pressure
V	Velocity
V_{abs}	Absolute velocity of jet
β	Angle jet makes with x-axis in x-y plane
ρ	Density
ϕ	Angle jet makes with x-y plane

For compressor:

A_c	Area of compressor normal to its axis
C_x	Average axial velocity through compressor
U	Mean blade speed
α	Angle between stator velocity and compressor axis

Subscripts:

1	Inlet
2	Exit
a	After mixing, before expansion

Appendix D

D	Diameter of hub
$\dot{m}_j$	Overall mass injection rate
M_t	Total flux of momentum injection per rotor passing
$\hat{\underset{\sim}{s}}$	Unit vector in the direction of the main flow at a flow coefficient of 0.342
V_{absj}	Jet velocity in the stator reference frame
V_{hub}	Hub velocity
V_{rad}	Radial velocity measured at a stationary point close to the rotating hub surface
V_{radj}	Radial velocity of each jet
V_{relj}	Jet velocity relative to the moving hub
β	Angle jet makes with the OXY plane
θ	Angle between the component of the jet in the OXY plane and the x-axis
ρ	Density of air
σ	Ratio of open area to hub surface area
ℓ	Length of slots (in z direction)

1.0 INTRODUCTION

1.1 Introduction

It is well known that the presence of grooves or slots (commonly known as "casing treatment") over the tips of compressor rotor blades can improve compressor stall margin. Not only is the stall point moved to a lower mass flow rate, but the pressure rise at which stall appears is also increased. Figure 1 illustrates one example of such improvement [1].

The improvement in stall margin, however, is generally accompanied by a decrease in compressor efficiency [2], [3]. The overall trend is that those types of treatment that work better in suppressing stall tend to cause higher efficiency penalties. Investigations have therefore been carried out over the years to understand the basic mechanism of casing treatment operation, with the goal of designing more effective and efficient treatments.

In examining compressor performance, it is often useful to categorize the mode of stall into two types: blade stall and wall stall. The former originates from the separation of the boundary layer on the blade suction surface whereas the latter refers to the substantial thickening of the boundary layer near the endwall, Fig. 2. As a direct application of this concept, it has been found that casing treatment is successful only in cases where wall stall occurs, [1], [4], [5], [6].

In the past decade many different treatment configurations have been tested (see, for example, [2], [3] and [7]). The results show that certain configurations are particularly effective in delaying stall. One of these, known as axial skewed grooves, was investigated extensively by Smith and Cumpsty [5]. Using this same configuration, but applying it on a rotor hub underneath a set of cantilevered stator blades, Cheng et al. [8] also saw a marked improvement in stall margin. This "hub treatment" has the advantage of

allowing the use of stationary instrumentation, making it much easier to obtain blade-to-blade flow measurements. Figure 3 shows the extent of improvement of the static-to-static pressure rise with the application of hub treatment. In this it should be noted that the experimental setup was designed so that the flow was similar to that in the tip region of a rotor; this was seen from both overall and detailed measurements.

1.2 MIT GTL Single Stage Compressor: Previous Work

As described, Cheng et al. [8] demonstrated the usefulness of hub treatment (treatment applied to a rotating hub) in retarding stall, Fig. 3, on the MIT GTL single stage compressor. Johnson subsequently examined the flow associated with the smooth (untreated) and treated hubs, [9], [10]. His results showed that, with the smooth hub, blockage appeared in the middle of the stator flow passage near the trailing edge just before stall. This can be seen in Figs. 4a and 5a. The first displays the (time-averaged) velocity field in a radial plane close to the hub. The second is a projection onto a plane parallel to the blade stagger angle, 38% of the pitch from the pressure surface. This pattern of flow as shown in the figures was consistent with findings in [4] and [5], which were investigations of rotor flows.

With hub treatment, the blockage disappeared when tested at the same flow coefficient. There was a high velocity jet near the leading edge, and flow removal near the trailing edge. These phenomena can be clearly seen in Figs. 4b and 5b. The jet (also cited in [2], [5] and [7]) had previously been believed to be the principal agent responsible for delaying stall, possibly by momentum addition to the endwall fluid. Johnson's data, however, showed that the jet travelled across the blade passage, impinged on the pressure surface and then travelled towards the stator exit on the blade surface without coming close to the area of high blockage that existed in the smooth build. The flow

removal, however, occurred in the area occupied by the blockage in the smooth build. Because of this, Johnson argued that it was the removal of the retarded flow near the hub trailing edge, and not the jet at the leading edge, that delayed the onset of stall. Although Johnson's arguments are plausible, this data did not give conclusive support of his hypothesis.

The next step along this line of investigation was therefore to test the validity of the hypothesis, by carrying out a control experiment in which the jet and the flow removal are examined separately. A study of this type is described in this report.

1.3 Objective and Overall Questions to be Answered

The main purpose of the project was to identify the stall-suppressing mechanism in a hub-treated compressor. This was done by separately simulating: 1) the jet at the front of the stator passage, and 2) the flow removal at the rear. To investigate the endwall flowfield in the case of injection, as well as to provide a check on the accuracy of simulation, a detailed blade-to-blade velocity map was obtained using hot wire anemometry. Variation of compressor performance with the amount of endwall flow addition or removal was also documented.

If Johnson's hypothesis were correct, little or no stall margin improvement should result upon simulation of the jet. In contrast, with flow removal there should be a large increase in stall margin, similar to the actual hub treatment. The present (first-of-a-kind) investigation is therefore a diagnostic experiment to quantify the relative roles of the jet and the flow removal in delaying rotating stall.

2.0 DESCRIPTION OF FACILITY

2.1 MIT GTL Single Stage Compressor

The design of the compressor is documented in detail in [8] and [11], but the following is a brief description of the features of the configuration used in the experiments:

1) Stagger angles of the rotor and stator are chosen such that the former is lightly loaded relative to the latter, i.e., the stator stalls first.

2) The stator row is designed to have the hub region highly loaded so that stall originates from this region.

3) The root clearance and the stagger of the stator were selected according to the criteria presented in [15] to promote the requirement of wall stall.

4) A large axial distance (roughly 1.1 span) was left between rotor and stator, to decouple the rotor from the stator and to allow room for the rotor wakes to mix out.

5) Low rotor twist ensured that the total pressure rise across the rotor hub was small compared to that across the tip. The total pressure was thus much lower (roughly one-half the dynamic head based on mean velocity) near the hub, so that the stator essentially operated with a hub radial distortion.

Table 1 lists the geometry of the rotor and stator blades.

The compressor was equipped with an inlet bellmouth with screen-honeycomb combination, a row of inlet guide vanes, a discharge throttle, a plenum/exhaust duct, and a downstream fan. Figure 6 shows an overall view of the system.

In the treated configuration, the compressor had slots cut into its rotating hub. The slots are described in Section 2.2.1. One modification of the compressor itself was the redesign of a seal separating the rotating hub from the rest of the compressor; the design of this is discussed in Section

2.2.2.

2.2 Modifications of Facility

The major modifications to the facility (compared to the configuration described in [8]) included:

1) Hub treatment

2) Seal (as mentioned earlier)

3) Flow injection-removal system

4) Orifice to measure injection-removal rate

These are described in the following sections.

2.2.1 Design of Hub Treatment

The aim of the experiments is to examine blowing and suction separately, and it is desirable to do this using the same treatment configuration as tested in [8] and [9] so that results could readily be compared. Previous geometry was 60 degree axial skewed slots with approximately 70% open area (dimensions are shown in Fig. 7). That treatment had been formed by gluing pieces of plexiglass in a groove machined on the surface of the hub. For the present experiment, exact similarity of slot dimensions could not be maintained, because it was not possible to machine similar open-ended slots. As a result, the open area was decreased to 50%. (As will be seen, this had little effect on the aerodynamic performance.)

A total of four aluminum hubs were fabricated. All had 60 degree axial skewed slots, but the axial length and location on the hub varied (see Fig. 8 for the one designated "full 90% slots"). The slots extended radially all the way through the hubs, so that they were open to the distribution plenum. Two of the four hubs were subsequently modified to yield three more configurations, so a total of seven configurations were eventually tested. These are designated as:

Nomenclature	Nominal Extent of Slot (Referred to axial blade chord)
1. Full 90% slots	5% - 95%
2. 22.5% front	5% - 27.5%
3. 22.5% middle front	27.5% - 50%
4. 22.5% skewed middle front	27.5% - 50%
5. 22.5% rear	72.5% - 95%
6. 45% front	5% - 50%
7. 45% rear	50% - 95%

Figure 9 shows locations of the slots in the stator passage. With the "full 90% slots", the slot covers the middle 90% of the axial chord of the stator, similar to the original treatment. The "22.5% rear" had slots, 22.5% of the axial chord in length, located at the rear part of the stator passage, etc. The "22.5% skewed middle front" were constructed so that the front and rear slot edges had a 45-degree angle relative to a plane perpendicular to the compressor axis. Relative flow at slot exit for these slots would then be inclined at 45 degrees to the axial direction, measured in the plane of the slots.

2.2.2 Seal Design

The purpose of the seal was to limit leakage flow through the gap existing between the rotating hub and a stationary downstream flange, Fig. 6. Redesign of the seal was necessary because of the high pressure differences between the injection-removal plenum and the stator passage. The gap was only a quarter axial chord downstream of the stator trailing edge, and it was desirable to limit the leakage flow.

Figure 10 shows details of the seal, made of teflon, because of the heat-resistant and non-abrasive nature of the material. The seal was held to the flange by nylon screws to prevent damage to the mating grooves on the hub in case rubbing occurred.

The lip of the outermost mating groove on each hub was also designed such

that leakage flow would enter the main flow path at 60 degrees from radial, at least one-quarter axial chord downstream of the stator trailing edge. Interference of leakage with stator flow was thus expected to be minimal; as seen below, this was indeed the case.

2.2.3 Flow Injection-Removal System

There were two sources of air supply for the purpose of injection, the GTL oil-free compressor (pressure rise of 650 kPa and maximum flow rate of 0.23 kg/s), and the Nash compressor of the Wright Brothers' Wind Tunnel (pressure rise of 300 kPa and maximum flow of 0.45 kg/s). The air passed through a butterfly control valve, a straightening/smoothing device, an orifice, a manifold and hoses, and finally another set of straightening/smoothing devices before reaching the distribution plenum. The manifold was an aluminum cylinder having an internal diameter of 152mm and a wall thickness of 12.7mm, connected to the test rig via ten flexible hoses. Figure 11 illustrates the main features of the pipe system.

Each straightening/smoothing device in the pipe consisted of a honeycomb structure for eliminating swirl and two perforated screens to suppress non-uniformities in the flow. To distribute the injection air uniformly over the slots on the hub, a screen was also secured at the entrance to the distribution plenum.

Flow removal was accomplished using the GTL steam ejector. Its characteristic is displayed in Fig. 12 (from [16]). The bled air went through the pipe-work described above, in the reverse direction. A separate butterfly valve controlled the flowrate.

2.2.4 Orifice Design

Injection-removal rate was measured by an orifice. The data in [9] showed that the flow in the slots was approximately 3.5% of the compressor

through flow, at a flow coefficient of 0.342. In view of the scheduled parametric studies, injection-removal rate was anticipated to vary between 1% and 7% of the main flow at that flow coefficient (corresponding to 0.04 kg/s and 0.28 kg/s respectively at the test speed of 2600 RPM).

Since flow was meant to occur in both directions, a symmetrical sharp-edged orifice was used with preliminary design based upon orifice data found in [12]. (Note that the orifice was then calibrated so that accuracy was not dependent on this estimation.) Mass flow rate through an orifice is given by

$$\dot{m} = \alpha_d A_{op} \left(\frac{2\rho \Delta P}{1-B^2} \right)^{1/2} \tag{1}$$

where

$\dot{m}$ is mass flow rate through orifice

α_d is discharge coefficient

A_{op} is area of orifice opening

ΔP is pressure drop across orifice

B is area ratio, orifice/pipe

ρ is density of fluid

In choosing B, one has to compromise between the sensitivity of the orifice and the pressure drop across it. A value of 0.3 was chosen for B, and the corresponding sensitivity was such that for $\dot{m}$=0.04 and 0.28 kg/s, ΔP=1.1 and 51.8 inches of water respectively. Since pressure drop was measured by a pressure transducer having a resolution of 0.01 inch of water, the resolution was satisfactory. In addition, for this design the estimated discharge coefficient was virtually independent of the orifice Reynolds number in the relevant flow range.

2.3 Instrumentation

2.3.1 Steady State Pressure Acquisition

Steady state pressures were acquired by 20 total pressure kiel-head probes, 24 hub and casing static pressure taps and 1 pitot-static probe. These were located at five axial stations, as shown in Fig. 13. A Scanivalve measured the pressures via a transducer, the calibration of which can be found in Fig. 14. A detailed description of the pressure instrumentation is given in [11], with the only modifications being the addition of two kiel-head probes and a pitot-static probe at station 1. This was done because six of the original eight kiel-head probes were in wakes of the supporting struts, and thus read total pressure, which was slightly lower than free-stream. The circumferential average total pressure included a correction for the presence of the struts.

An axial velocity traverse was carried out upstream of the IGV to assess the blockage arising from the wall boundary layer [9]. This measurement, together with the total and static pressure at station 1, gave the annulus averaged axial velocity. Pressure in the injection-removal plenum was also monitored.

2.3.2 Hot Wire Data Acquisition

The stator blade-to-blade flowfield was obtained using a hot wire at a number of specified grid points in a flow passage. A full description of the technique is given in [9], and only a brief account is presented here.

2.3.2.1 Data Acquisition Grid

The grid points were confined to within 30% of the blade span next to the hub, as all the main features of hub-treated flow took place in this region. The points were approximately 3mm apart (∿8% of chord) and were regularly spaced so that velocities measured by the hot wire could be projected onto

three families of surfaces containing such points.

Figure 15 shows one of the three types of surfaces: constant radius. Seven of these were stacked an equal distance from each other in the radial direction, with each containing 97 grid points. The lowest one was 2% span away from the hub surface and was within the tip clearance, which was approximately 3% span. Although the surfaces were slightly curved, for convenience in viewing they are flattened out.

The chordal planes, section A-A in Fig. 15, were parallel to the blade stagger angle. Projection of velocities on these planes is useful for giving information about the flow in the streamwise direction.

The axial planes, section B-B in Fig. 15, were perpendicular to the axial direction. There were ten of them in all.

Note that data was also taken in the adjacent passage. These additional points were useful for examining the flow through the blade clearance gap, as well as providing a check on the measurements made in the main passage.

2.3.2.2 Positioning System

The positioning system consisted of a traversing mechanism (screw actuator), a 15/1 reduction gear box, an angular transducer, a stepping motor, a linear transducer and a mechanical link. Figures 16 and 17 show all these save the mechanical link, which was the only non-automated component. The positioning system was responsible for moving the hot wire to locations specified by grid coordinates stored in the computer; detail of its design and operation can be found in [9].

2.3.2.3 Hot Wire Data Acquisition System

A single hot wire probe was used to obtain three-dimensional time-averaged velocity data, based on a method originally devised by Wagner and Okishi [17]. Appendix C contains a detailed description of a modified version of this

method, but a brief discussion is given here.

The basic working principle is that the output of a hot wire is a function of pitch angle, yaw angle and absolute velocity (see Fig. 18 for the definitions of these quantities.) Thus, hot wire signals at three different wire orientations can determine the magnitude and direction of the local flow, provided the hot wire is properly calibrated. The hot wire probe was therefore rotated (about its axis) to three distinct orientations at each grid location. At any one orientation, the time-averaged signal was obtained through an analogue-to-digital converter by averaging the samples taken at 16 khz for 1 second.

2.4 Orifice Calibration Procedure

The orifice was calibrated in situ for both blowing and suction using cobra probe traverses. Each of the two traversing planes was located one diameter away from the orifice plate. To measure the static pressure in either plane, four static pressure taps were equally spaced around the pipe at the wall.

For a particular valve setting, the cobra probe was traversed across the pipe (axisymmetry of the flow had been verified previously). To eliminate error introduced by the blockage due to the presence of the probe, static pressures were obtained before the probe was moved in. Temperatures were also measured from a thermocouple. The mass flow rate was calculated by numerically integrating the velocity over the cross-section of the pipe.

At the same valve setting, the average pressure drop across the orifice was measured via eight corner taps (four on each side) located at the intersection of the orifice plate and the pipe. The valve setting was then changed manually and the traversing process repeated. This was done a number of times, so that for each mass flow rate (and orifice Reynolds number), there

was a corresponding orifice pressure drop. The results were curve-fitted, and are shown in the next section. Potential flow calculations showed that errors due to streamline curvature at the traversing stations were small (radial velocities less than 1% of axial velocities, static pressure non-uniformity less than 2% of the mean dynamic pressure).

2.5 Orifice Calibration Results

A typical velocity profile upstream of the orifice plate is shown in Fig. 19. The discharge coefficient, α_d, is presented as a function of the Reynolds number, Re, evaluated at the orifice opening for both blowing and suction. For blowing:

$$\alpha_d = 1 - 0.1996\ Re^{0.0447}$$

and for suction:

$$\alpha_d = 1 - 0.2491\ Re^{0.0299}$$

Although these may look functionally different, in the range of interest the difference in α_d was approximately 0.02, so that in fact both sets of data could be fitted by a single curve with very little loss in accuracy.

Figures 20 and 21 show the two curves fitted onto the data. The slight disagreement in the two coefficients (3%) may be due to differences in upstream profiles. Mass flow rate calculated with the measured quantities via Eq. (1) had an estimated error of ±5%.

3.0 DESCRIPTION OF EXPERIMENT

There were two parts to the present experiment. The first was a parametric study of the pressure characteristics (based on the outer wall static pressure rise), commonly known as speedlines, with endwall flow injection-removal. The second focussed on the detailed stator flow field measurement in the presence of injection.

3.1 Pressure Rise Characteristics

The conduct of this parametric study can be summarized as follows:

All speedlines were taken at a compressor speed of 2600 rpm, corresponding to a rotor tip Mach number of 0.24 and a Reynolds number based on blade chord at the stator midspan of $1.0*10^5$. Previous tests showed that Reynolds number effects were not significant with the baseline hub treatment and smooth wall configurations [8].

The smooth hub and the full 90% slots were first tested without injection or removal. Since these slots were open to the plenum, a run was also made with the bottom of the slots sealed to eliminate the interactions between the latter and the plenum. The performance of hub treatment with and without the plenum could then be compared.

Different hubs were also tested with the injection-removal rate varied; the maximum was 6% of the main flow. The 22.5% slots, however, were only tested to suction rates of 3.6%, since for these the plenum pressure was so low that damage was caused to the seal. (Again, for reference, the measured mass flow (in and out) through the original hub treatment was approximately 3.5%.) In the tests, the flow near the stator hub was monitored by a hot wire to identify the stall point.

Control experiments were carried out frequently to verify that leakage through the seal had no effects on the speedlines. This was accomplished by

acquiring smooth hub speedline while applying positive and negative pressures representative of those under conditions of injection and removal respectively. (With the same plenum pressure, leakage flow in both the control and actual experiments should then be the same.)

3.2 Time-Averaged Stator Flow Field Measurement

Time-averaged three-dimensional stator flow field measurements were obtained for the 22.5% front slots at a blowing rate of 2.8%, expressed as percentage of the through flow at a flow coefficient of 0.342. This was done to simulate the jet in an actual hub treatment. The results documented in Chapter 4 show that this configuration also had one of the highest stall-delaying potential for a given mass injection rate.

Only time-averaged flow field measurements were obtained since unsteadiness had been found to occupy only a small region close to the hub and near the leading edge, as illustrated in Fig. 23 from [9]. This figure is for a location at mid-passage near the leading edge. A rapid decay in unsteadiness is seen, due to mixing of the outcoming jets. Figure 22, also from [9], shows the small level of unsteadiness near the trailing edge where flow removal took place.

4.0 EXPERIMENTAL RESULTS

4.1 Compressor Performance: Speedlines

Speedlines were taken for all of the hubs as described in Chapter 3. Data showing the dependence of the stator static-to-static pressure rise on injection-removal rate is presented in this chapter. Pressure rise, DP, is non-dimensionalized in two alternative ways, by $0.5\rho U^2$ and $0.5\rho\overline{V}_{in}^2$, where U is the mean blade speed, $\overline{V}_{in}$ is the mean stator inlet absolute velocity and ρ is the density. Compressor flow rate is presented as flow coefficient, $\overline{C}_x/U$, where $\overline{C}_x$ is the average axial velocity measured upstream of the inlet guide vanes. Injection-removal rate is given as percentage of the compressor main flow at $\overline{C}_x/U=0.342$, which was the near-stall point for the smooth wall. Although there is no absolute criterion for selecting the normalizing compressor flow rate, 0.342 is used because it is the flow coefficient at which hot wire measurements were taken.

$\overline{V}_{in}$ is calculated from $\overline{C}_x$ and the mean stator inlet angle, $\overline{\beta}_{in}$. The stator inlet angle, β_{in}, is documented in [8]. Figure 24 (from [8]) shows the spanwise variation of β_{in} at $\overline{C}_x/U=0.305$ and 0.345. The profile is skewed from hub to tip and this distribution also varies with the flow coefficient. Since measurements of β_{in} between $\overline{C}_x/U=0.305$ and $\overline{C}_x/U=0.345$ were not documented in [8], inlet angles at other values of $\overline{C}_x/U$ were obtained by linearly interpolating the $\overline{\beta}_{in}$'s at $\overline{C}_x/U=0.305$ and 0.345. $\overline{V}_{in}$ can then be defined from $\overline{C}_x/U$, U and $\overline{\beta}_{in}$ via

$$\overline{V}_{in} = \frac{\overline{C}_x}{\cos\overline{\beta}_{in}} \qquad (2)$$

Note that in the present experiment the magnitude of the stator inlet velocity varies strongly from hub to tip, and there is no clear criterion for

the "proper" normalizing dynamic pressure. The conventional one is perhaps based on the area-averaged inlet velocity. This, however, would require the knowledge of profiles of β_{in} and C_x at all conditions, and it was not possible to obtain measurements of all such profiles to do the averaging. The alternative followed here is thus to use $\bar{V}_{in}$ given by Eq. (2).

The estimated measurement uncertainties of $DP/0.5\rho U^2$ and $DP/0.5\rho\bar{V}_{in}^2$ were ±2% and ±3% of the stalling value of the smooth wall build respectively. For the flow coefficient the measuring error was ±1%.

4.1.1 Speedlines: Baseline Runs

The smooth build and the 90% hub treatment slots, sealed at the slot bottom, are selected to be the baselines by which the effectiveness of various slots are assessed. This section presents results obtained with these configurations. Discussions will be given in Chapter 5.

The smooth wall speedline is displayed in Figs. 25a,b, together with two cases tested with the 90% slots, one with the slot bottom sealed and one with the slot bottom unsealed. The occurrence of stall is marked by the solid flagged point on every speedline. The stall points are at or very near the peak of the pressure rise curve. This is also true for the other configurations described below. With the smooth build, stall occurs at the same pressure rise seen in [9] at $DP/0.5\rho U^2=0.083$, although there is a slight shift in speedline and stall point,i.e., these are roughly 2% lower in $\bar{C}_x/U$ than that given in [9]. Possible explanations for the small shift might be the installation of the new seal, or the improved rotor assembly and alignment procedure. In any event, 1) the speedlines for the present series of builds were repeatable, and 2) the stalling pressure rise was the same as that documented in [9], $DP/0.5\rho U^2=0.083$ and $DP/0.5\bar{V}_{in}^2=0.268$.

The same figures show results from the 90% slots, sealed at the bottom.

In this case stall occurs at $\overline{C}_x/U=0.297$, a 10% change from the smooth build. The stalling $DP/0.5\rho U^2$ and $DP/0.5\rho\overline{V}_{in}^2$ are equal to 0.137 and 0.461, corresponding to 66% and 72% improvement over the smooth wall build respectively. There is an abrupt drop in pressure rise at stall.

With the 90% slots unsealed, stall appears at a slightly lower $\overline{C}_x/U$ of 0.294. The stalling $DP/0.5\rho U^2=0.138$, with $DP/0.5\rho\overline{V}_{in}^2 = 0.465$. The abruptness of the drop at stall is similar to that with the sealed slots.

For reference, the stall points reported in [9] were at $\overline{C}_x/U=0.295$, $DP/0.5\rho U^2=0.145$ and $DP/0.5\rho\overline{V}_{in}^2=0.488$ with the sealed treatment. Those slots had 17% more open area, and this is viewed as the probable cause of the 5% extra gain in stalling pressure rise over the 90% sealed slots in the present experiment.

Leakage through the seal downstream of the stator was found to have negligible effects on the pressure rise characteristics. Figures 26a,b display three smooth wall speedlines: one with positive pressure in the injection-removal plenum, one with negative pressure, and one without application of pressure. The positive and negative pressure levels corresponded to plenum conditions in those cases with high injection and removal rates. Within experimental error the speedlines thus obtained all lie on top of each other, implying no change in the overall stator passage endwall flow due to the downstream leakage.

4.1.2 Speedlines: All Other Hub Geometries

Figures 27a,b present speedlines obtained with no net injection or removal, for all the different hub geometries. The baselines are included for comparison. Compared to the peak pressure rise of the smooth build, the 22.5% slots give improvements in $DP/0.5\rho U^2$ and $DP/0.5\rho\overline{V}_{in}^2$ of at most 10%, whereas the two 45% slots achieve 40%. Slots at the front of the stator in general

perform better than slots at the rear. The sudden drop in performance of the 45% slots at stall is similar to that of the 90% slots.

Figures 28a,b through 32a,b show the pressure rise characteristics of the 22.5% and 45% slots with different suction rates. The speedlines from each build are shown together. Compared to the smooth-wall baseline, stall is suppressed at all suction rates. In addition, the speedlines are displaced from the smooth-wall baseline and also from the zero-flow curves, even in the pre-stall regions, by amounts depending on the rate of removal. This will be discussed further in Chapter 5 and Appendix A. A point to note in passing is that a large hysteresis loop appears at 6% suction through the 45% slots. Having secondary importance in the experiment, it was not pursued any further.

Speedlines obtained with different injection rates are shown in Figs. 33a,b through 38a,b. Injection at the stator hub increases the stalling pressure rise, with injection at the front of the passage being generally more effective than injection at the rear. The displacement in the pre-stall portion of the speedlines away from the smooth-wall baseline is smaller than that found with removal; this will be elaborated in Chapter 5 and Appendix B.

4.1.3 Effects of Slot Flow Rate on Stalling Pressure Rise

Figures 39a,b show stalling pressure rise plotted with injection-removal rate for all of the hubs. Six different curves (actually straight line segments), together with the baseline stall points, are shown in each plot. Stalling pressure rise is expressed as percentage increase over the smooth-wall value. Injection and removal rate is, as previously, normalized by the compressor flow at the flow coefficient of 0.342. The effects of slot flow rate and injection-suction location on the onset of stall is clearly seen in these plots.

Several observations can be made from these two figures. First, for flow

removal:

1) Stalling pressure rise of the 22.5% slots and 45% front slots increases monotonically with suction rate over the whole suction range. However, this is not the case with the 45% rear slots. With no suction, the increase in stalling pressure rise of the latter is roughly 35%. As suction increases from zero, there is an initial drop in the stalling pressure rise, reaching the lowest at around 1.5% suction; after which performance improves with no further drop. The zero-suction value is reattained at 2.2% suction.

2) Effectiveness of the 45% front slots differs considerably from the 45% rear slots at low suction rates. The 45% front slots have good capability to delay stall at low suction rates (around 1.5% removal, say), giving a 55% increase in stall margin.

3) Figures 39a,b show little difference between data for the 22.5% front and rear slots, which are the two most ineffective slots tested for suction. Effectiveness of the 22.5% middle front slots surpasses these two by approximately 10%, up to a level of suction roughly 3%.

4) All curves intersect at approximately 3.5% suction rate, which is the amount of slot flow in the hub treatment in [8] and [9]. The stalling $DP/0.5\rho U^2$ and $DP/0.5\rho\overline{V}_{in}^2$ of the 45% rear slots match the full slot performance at 4.7% and 4.9% suction respectively.

For flow injection:

1) The slot effectiveness varies over the whole range investigated. This is in contrast to suction, where the curves intersect at 3.5% removal.

2) With the 45% slots, the decrease in effectiveness as injection rate increases from zero to 1.5% occurs in both front and rear slots. The stalling pressure rise of all the 22.5% slots, however, increases monotonically with blowing rate.

3) The 22.5% middle front out-performs all other 22.5% slots at all blowing rates, and the 45% ones at blowing rates higher than 2%.

4) The 22.5% skewed middle front is considerably less effective than the 22.5% front or middle front.

5) The stalling pressure rise of the full 90% slot is equalled by the 22.5% middle front slots at 3.3% injection.

4.2 Detailed Flowfield Measurements

It was noted in Chapter 1 that flow injection occurs near the leading edge of the stator passage in the case of a hub (or casing) treatment. The experiment involving hot wire measurements is to study the injection of the jet and its effects on the endwall flowfield.

Figure 40 shows the velocity vector projected onto a radial plane at 2% span above the hub surface. The convention adopted is that a circle and a cross at the root of a velocity vector represent flow coming out of and going into the paper respectively. The jet is seen to traverse across the blade passage, impinging on the pressure side of blade 1. Figure 41, an axial plane looking downstream at 8% axial chord, shows another view of this. Even though the magnitude of the simulated jet is roughly only 3/4 of that in Johnson's treatment (compare Fig. 40 with Fig. 4b), the overall endwall flow pattern associated with Johnson's jet is reproduced.

One feature of the flow that has not been given attention in the past is also seen in the present experiment. This is the circulation at the rear of the stator passage, illustrated in Fig. 42, which shows an axial plane at 78% axial chord from the leading edge. This will be examined in detail in the next chapter. Additional figures showing the endwall flowfield can be found in Appendix E. These also bear out the similarity between the flow in the front of the passage with hub treatment and the situation with injection from the hub.

5.0 DISCUSSIONS AND CONCLUSIONS

5.1 Figure of Merit

The figure of merit adopted to assess the effectiveness of various slots is the non-dimensional stalling pressure rise attained, $DP/0.5\rho\overline{V}_{in}^2$. Although one can debate the use of this criterion, its basis is that it is the endwall regions which give rise to stall, and what we are assessing is the ability of the flow in these regions to cope with a given non-dimensional pressure rise. Note that relying on the flow coefficient at the stall point is somewhat ambiguous because the flow coefficient depends on the measurement station. The flow coefficient used is measured upstream of the stator. Had it been measured downstream, however, the speedlines with flow removal would have shifted to the left (that is, towards lower $\overline{C}_x/U$) and those with flow injection to the right. (This speedline shift was also mentioned by Koch [13] in a similar experiment involving casing boundary layer control via blowing and suction.)

$DP/0.5\rho\overline{V}_{in}^2$ is by no means the only figure of merit that can be used. If it is desired to assess performance of the stator in terms of the pressure rise only, $DP/0.5\rho U^2$ is the one to use. However the latter does not really carry information of inlet conditions, and so from a "fluid mechanic" point of view, normalizing by the inlet dynamic head is a better choice. This is also an adoption of the common convention used in the case of a simple diffuser with blowing and suction applied to its diverging section. It should be emphasized that the trends appear similar with either non-dimensionalization, so that conclusions based on either $DP/0.5\rho U^2$ or $DP/0.5\rho\overline{V}_{in}^2$ will also be similar. The term "performance" will hereafter refer to the stalling pressure rise normalized by the stator inlet dynamic head, unless otherwise stated. A high stalling $DP/0.5\rho\overline{V}_{in}^2$ thus indicates good "performance".

5.2 Performance With No Net Injection or Removal

Performance of the 90% slots is 5% lower than that of the hub treatment used in [9] or [10]. In both these hub treatments, low momentum flow at the rear end of the stator passage is sucked into the slots, has work done on it by the hub, and emerges at the front as a high momentum jet. There is no hot wire data for the 90% slots, so the exact amount of slot flow in this build is uncertain, but the similar performance of the 90% slots and the treated hub of [9] and [10] suggests that slot flow in the former is near the value of 3.5% measured in the latter.

With the 45% slots, performance drops to half of the value reached by the 90% slots. Even so, the increase in stall margin implies that there is still some internal injection and removal, similar to the 90% slots as described in the previous paragraph. For the 22.5% slots, the speedlines are very similar to the smooth wall baseline, and one can conjecture that little internal injection or removal occurs in these slots.

5.3 Performance With Flow Removal

First consider flow removal at the rear. Referring back to the performance curves of the 22.5% and the 45% rear slots (Figs. 39a and b), the success of these two slots in suppressing stall supports Johnson's hypothesis regarding endwall flow removal [9]. The basic idea is that the removal of low momentum fluid at the rear of hub or casing treatment slot helps delay stall. If so, one might expect the amount of stall suppression to increase with suction rate, and this is generally the case, as confirmed by the data for the 22.5% rear slot and for the 45% rear slot at high suction rates. Behaviour of the 45% rear slots at low suction rates will be addressed subsequently.

Consider now local suction at the front half of the stator passage, through the 22.5% front and 22.5% middle front slots. Figures 4a and 5a

indicate that blockage does not appear at the front half of the passage, so it does not appear appropriate to talk about the direct action of removal on the blockage. Rather, as in the case of suction not far from the leading edge of an airfoil, removal at the front half of the passage may alter the development of the endwall layer downstream of the location of suction. Both mechanisms, corresponding to suction at the rear and at the front, appear effective, as Figs. 39a,b show little difference in the performance of the 22.5% front and rear slots over the whole suction regime.

Behaviour of the 45% front and rear slots can be rationalized as follows. With no suction they operate like conventional hub treatments, drawing in low total pressure flow at the rear, doing work on it, and ejecting it as a jet at the front. As the suction gradually increases, there is a change from circulating flow (at zero suction rate) to non-circulating (totally outward) at high values of removal, and this explains the form of the two curves in Figs. 39a,b.

At 3.5% suction, the approximate amount of circulating slot flow in the 90% slots, the stalling $DP/0.5\rho\overline{V}_{in}^2$ of all slots is 55% higher than that of the smooth build, but is less than the 70% level attained by the 90% slots. This implies that suction is not the sole cause of the increase in stall margin and that the jet is also responsible for the observed improvement.

As an adjunct to this discussion concerning suction, Appendix A provides a simple estimate of the pressure rise in a diffusing cascade with suction. The calculated values agree well with experimental data, given in Table A.1.

The effects of flow removal cause the pressure rise with suction to be higher than the smooth wall value at a given flow coefficient in the unstalled regime. It should be emphasized, however, that the gain in stalling pressure

rise is not due to some inviscid effect of increased diffusion only. To see this, suppose suction were applied through slots located at the outer casing, instead of at the rotating hub. The increase in pressure rise due to inviscid diffusion effects in this thought experiment should be the same as that in the real experiment having the same suction rate. Since the hub boundary layer in the thought experiment was not acted upon by suction, the stalling pressure rise causing the breaking-down of the boundary layer, however, would not differ from the smooth wall value. The increase in stalling value of pressure rise is thus due to a change in the hub boundary layer.

5.4 Flow Injection

With endwall flow injection, there is much more variation in effectiveness among the slots. Also, the analysis of Appendix B demonstrates that the static pressure rise due to mixing of the jet with the stator main flow is small compared to the observed improvement in stall margin. (This is consistent with the small departure of those speedlines with injection from the unstalled portion of the smooth wall speedline.) The improvement is thus not just the by-product of the mixing of the jet with the main flow, but rather is the result of some other mechanism.

5.4.1 Location and Orientation of Injection

With injection, both the jet location and the jet momentum govern the amount of improvement (Figs. 39a,b). Injection through the 22.5% front and 22.5% middle front is much more effective than that through slots of the same size at the rear. (Comparison with the 22.5% skewed middle front is excluded for the present because of its different configuration.)

Figure 43 plots the performance of all of the 22.5% slots with injection as a function of the absolute (or total) momentum flux of injection. Data is

the same as that of Fig. 39b for blowing except that the momentum flux is used rather than the mass flow rate. (The former has been normalized by the momentum flux of the main flow at a flow coefficient of 0.342.) Details of the additional information needed for this are documented in Appendix D.

Performance of the 90% slots is represented as the solid bar in Fig. 43, because the momentum flux of the jet in this case was only estimated based on the measurements in [9]. The resulting estimate for the performance of the 90% slots is thus accompanied by an uncertainty band.

The superior performance of the 22.5% middle front is again visible in Fig. 43. The 22.5% front achieves 15% less than the the 90% slots at 9% momentum flux, whereas the 22.5% middle front is slightly more effective than the baseline. Re-orienting the jet at the middle front location so that it has less alignment with the main flow (corresponding to injection through the 22.5% skewed middle front), however, results in poor performance. More specifically, the 22.5% skewed middle front, which was designed to channel 40% less streamwise momentum flux than the 22.5% middle front (at 9% absolute momentum influx), is 45% less effective than the 22.5% middle front at that amount of absolute momentum influx. This suggests a possible correlation between streamwise momentum influx and stall-delaying potential.

In Fig. 44, the effect of the streamwise component of jet movement is brought out more explicitly. The abcissa in the figure is the component of momentum flux in the streamwise direction. The latter is based on the approximation that flow angle of the stator "free stream" flow decreases linearly from inlet to exit, with inlet and exit angles obtainable from Fig. 24. (The correspondence between mass injection rate and streamwise momentum influx is plotted in Fig. 45.)

The 22.5% skewed middle front performance curve has poor performance at zero injection, but then a rapid increase, and at 5% streamwise momentum influx it performs nearly as well as the 22.5% middle front. Based on Figs. 43 and 44, it appears that it is the streamwise component of the jet momentum flux which causes the favorable effect on stall suppression, although the reason underlying its success is still unresolved. One possible explanation is that the streamwise component of the jet helps delay stall by actually energizing the endwall boundary layer. Other mechanisms, however, can also be postulated, such as a restriction in root leakage flow, which thereby suppresses stall. The view held here is that, without further investigation, the correct mechanism of jet operation cannot be identified.

5.4.2 Endwall Flowfield

Up to now, only the effects of jet location and orientation on overall performance have been investigated. This section examines changes in the flowfield brought about by the injection at the front.

5.4.2.1 Accuracy of Simulation

Figures 46a,b,c through 52a,b,c (except 48 and 50) show projection of velocities on various geometrical planes for: a) the smooth wall, b) the treated hub used in [8] and [9], and c) the 22.5% front slots with injection. We first examine the relation between the hub treatment flow and the injection flow. Figures 46a,b,c are views of the radial plane at 2% span next to the hub surface. In each of (b) and (c), a jet is seen to emerge from the endwall at the front of the stator passage. (The dotted rectangle in (c) represents the location of injection.) The jets in (b) and (c) behave similarly in that they both impinge on the pressure side of the left blade (blade 1 in the figure).

Although the velocity of the hub treatment jet is somewhat higher, the trajectory of each jet after striking the blade is demonstrated in Figs. 47a,b,c, which show chordal planes 8% of pitch from the pressure surface. These show that, after striking the blade, the jet travels upwards and towards the stator exit on the blade surface.

Note the very close correspondence between (b) and (c) from Figs. 46b,c and 47b,c; it is observed that the velocity magnitude of the jet in (c) is roughly three-quarters of the one in (b). However, the trajectories of the jets in both cases are quite similar, despite this difference in jet velocity. In addition, as will be shown subsequently, pitch averaged velocities also show a close simulation. Hence, the simulated injection does resemble the jet in a conventional hub treatment, with the overall jet trajectory represented diagramatically in Fig. 48. (In Fig. 47a, there is of course no jet seen with the smooth hub.) A central feature of the flow in Fig. 47a is a reduction in chordal velocities near the trailing edge; this is a region of high blockage. This reduction in chordal velocity will be examined in the next section.

5.4.2.2 Comparison of Rear Passage Endwall Flow

Consider now the flow in the rear of the passage. With the smooth hub, the flow near the trailing edge has only a small streamwise component of velocity (see Fig. 46a). In contrast, the same region of flow in Fig. 46c has higher streamwise velocities. (Figure 46b represents a different situation as flow is removed from the endwall.) This implies that the blockage has decreased in (c).

The same conclusion can be inferred from Figs. 49a,b,c, which are chordal planes at 28% pitch from the pressure side, arranged in the same order as before. There are marked differences in the behaviour of the rear-passage,

endwall flow in all three cases. The blockage that corresponds to an area of small chordal velocities close to the hub is clearly visible near the trailing edge in (a). In contrast to this in Fig. 49c, no area with significant decrease in chordal velocities is seen. The flow at 2% span in the rear half of the passage is parallel to the hub surface. Furthermore, chordal velocities (which are very close to streamwise velocities) in that area are considerably higher than those in (a), and are comparable to those in the upper planes. In (b), again, the situation is very different from both (a) and (c), since with a complete hub treatment the blockage is removed due to the flow entering the slots at the passage rear.

5.4.2.3 Pitch-Averaged Streamwise Velocity Profile

We can also look at the flowfields in another manner, as in Fig. 50, which presents the evolution of the pitch-averaged streamwise velocity through the stator passage. The pitch-averaged streamwise velocity is normalized by the annulus-averaged streamwise velocity at that location. At inlet to the stator (0% axial chord), all three profiles, corresponding to the smooth hub, Johnson's hub treatment and 22.5% front slots with 2.8% injection, have roughly the same shape, with no significant reduction in velocities near the hub surface. Some traces of the jet in (c) are already visible at this axial location.

At 8% axial chord, the effect of the jets is seen with the hub treatment and with the injection. There is a region of increased velocity covering approximately the lowest 10% of the span. At locations from 8% to 55% axial chord, an upward movement of the point of highest velocity can be identified, due to the jets' trajectory. The strong similarity between the injected flow and the hub treatment flow is also clearly evident.

Up to 55% axial chord, the smooth wall profile shows no marked reduction in velocities close to the hub surface. After this axial location, however, considerable reduction in streamwise velocities near the wall takes place. The reduction of streamwise velocities also occurs with hub treatment and with the injection, although it is much less severe. At the 100% axial chord location, flow at 2% span in the case of the smooth hub leaves the passage with a streamwise velocity that is 40% of the mean flow, compared to 60% in the other two cases. This further confirms the existence of higher blockage in case (a) as described in Section 5.4.2.2.

5.4.2.4 Examination of Secondary Circulation in the Stator Passage

In Fig. 49c, one can see downward velocities in the upper radial planes near the trailing edge. This appears more clearly in Fig. 51c, which shows an axial plane at 78% axial chord from the leading edge. Around the rectangular contour, the circulation is equal to 0.45 $\overline{C}_x b_{ax}$, where b_{ax} is the stator axial chord. The flowfield associated with this circulation is such that, at 6% span, flow near the suction side of the blade passage possesses downward (towards the hub) velocities, and upward velocities near the pressure side. The amount of flow transported downward through the radial plane at 6% span is 1.4% of the mass flow rate of the main flow, equivalent to 1.2% normalized momentum flux. In contrast to the flow at 6% span, at 2% span the flow is parallel to the hub.

The circulation also occurs with conventional hub treatment, as seen in Fig. 51b. Around a similar contour, the circulation is equal to 0.49 $\overline{C}_x b_{ax}$. That this rear passage circulation is due to the jet can be proved by noting that the circulation around the same contour in the case of the smooth hub has a value of -0.10 $\overline{C}_x b_{ax}$. This has the opposite sense to the circulation

obtained with the treated slots. The positive circulation found with the treated slots thus originates from the jet (and not from other sources, such as secondary flow developed from upstream vorticity).

It is natural to ask if the mixing due to this circulation might energize the flow near the hub and thus help delay the stall. Recall that the normalized momentum flux of the main flow transported towards the hub surface is 1.2%. At 2.8% mass injection rate at the front, the normalized streamwise momentum influx at the location of blowing corresponds to 5.1%, from Fig. 45. This implies that momentum addition to the low total pressure flow due to increased mixing with the main flow is clearly not dominant, although its role may not be altogether negligible.

5.4.2.5 Further Comments on Endwall Flow Region

Figures 52a,b,c conclude the description of endwall flow; Fig. 52c is a chordal plane at 67% pitch in which both the jet and the downward flow appear. One also notices the healthy endwall flow at 2% span. (a) and (b) are included for comparison. Again, injection at the front and removal at the rear of the stator passage are clearly seen in (b).

The results that have been presented show that (perhaps only as one might expect) there is a link between the streamwise momentum flux into the endwall region and the increase in stall performance. One of the mechanisms by which the casing treatment works, therefore, might be simply by addition of streamwise momentum through high velocity flow injection. The data taken, however, does not prove this conclusively. In particular, it does not rule out the alternative mechanism mentioned in [10] - the suppression of tip leakage (which is known to have a very strong effect on stall point) by the jet. If the total pressure losses associated with the leakage flow are

decreased, the endwall region could be affected in a similar fashion by the direct momentum injection.

Finally, it should be noted that the endwall boundary layer has a non-collateral three-dimensional profile, with the flow at hub not aligned with the free stream flow. It thus would not be expected that two-dimensional boundary layer models are applicable or that conventional techniques of two-dimensional boundary layer control involving blowing and suction can provide a satisfactory framework within which results of the present experiment can be explained.

6.0 SUMMARY AND FUTURE WORK

6.1 Summary

An experimental investigation has been carried out to examine the effects on stall margin of flow injection into and removal from the endwall of an axial compressor blade row. The goal was to identify the mechanism by which wall treatment suppresses stall in turbomachines.

Results showed that, even though both injection at the front and removal at the rear of the blade passage increased the stall margin, neither was as effective as the complete treatment. This implies that both the removal of high blockage flow from the rear of the slot and the high velocity injection at the front are important causes of stall margin improvement in casing or hub treatment.

In regard to removal, the extent of stall enhancement did not depend heavily on the location of suction; in fact localized suction at the rear and front of the stator passage were equally effective. With the exception of improvement presumably due to the pressure field generated slot flow which occurred at low suction rates (only for the 45% slots), the performance increased monotonically with the amount of removal. The overall trend suggests that endwall suction delayed stall either by directly removing low momentum flow, as in the case of rear-passage suction, or by delaying the formation of such a flow, as in the case of front-passage suction.

With endwall injection, both the amount of momentum injected and the location of the injection strongly affected the stall margin improvement. Injection through a location from 27.5% to 50% of the passage worked as well as the full treatment. Injection through a location from 5% to 27.5%, which corresponds most closely to the simulation of the jet in the full treatment, was less effective. Injection in the rear of the passage delayed stall by

only a small amount. Although the experiments were carried out for one blade row only, the stagger angle, inlet velocity triangles, and overall performance are representative of rotor tip behavior for geometries of current interest. This, coupled with the apparent insensitivity of stall inception in multistage compressors to the precise details of the blading [15], implies that the results should have quite considerable generality, certainly (if not more than) for the basic trends.

The streamwise momentum component was found to be crucial to the success of endwall injection; the amount of stall suppression increased with the streamwise momentum influx. Detailed flowfield measurements revealed the presence of streamwise vorticity at the rear of the passage, when the jet was simulated at the front. The vorticity was oriented in such a way that the endwall flow appeared to be energized by mixing with the main flow.

Based on these findings, it is hypothesized that three aspects of the jet could contribute to stall enhancement. In the order in which the author rates their importance, these are: 1) direct streamwise momentum addition to the endwall boundary layer, 2) a decrease in the tip (or root) leakage flow, and 3) (a distant third) mixing of the latter with main flow due to the rear-passage vorticity. Number two (2) was not directly investigated in the experiment; it is a conjecture based on accumulated data. Since the three mechanisms were interrelated in that they came from the same source, namely, the jet itself, it is necessary to decouple them before one can uncover the story behind the success of injection. This leads to future work.

6.2 Future Work

Investigation on casing or hub treatment has so far been essentially all experimental, and the author knows of relatively little effort that has been put in to simulate the flow numerically. One suggestion for future work is to

investigate the possibilities by numerically simulating the tip leakage, main flow, and slot efflux or influx using a three-dimensional viscous solver. The aim here is geared towards understanding the non-collateral structure of the endwall boundary layer and also its interaction with tip leakage flow. The trajectory of a "leakage element" can be tracked computationally, hence the involvement of leakage flow can be studied. A further step is to simulate flow injection (and maybe removal) by altering the boundary conditions. Again, by keeping track of the "leakage element", one should be able to tell if the jet does alter tip leakage flow. Such an attempt, if successful, will generate the complete endwall flowfield with and without the jet. Results thus obtained will be most illuminating in the understanding of casing treatment operation and even the origin of endwall stall.

Experiments using the same setup can also be used to further examine the streamwise momentum factor of the jet by varying the angle of the slots. A device such as a tracer-gas unit can be simultaneously employed to trace out root leakage flow for the purpose of seeing its involvment in stall onset, and also its interaction with the jet. One way to do this is to release the gas close to the root of the pressure surface in the adjacent blade passage, and measure its concentration in the main measuring passage. The amount of leakage flow can then be known via the measured concentration of the gas.

The strength of such an experiment would be that it directly examines the role of leakage flow, which has long been known to have a detrimental effect on the stall margin. The goal of the investigation would be to unveil the path of the leakage flow, and to see if the jet cuts down the amount of leakage, thereby delaying stall.

REFERENCES

1. Smith, G.D.J., "Casing Treatment in Axial Compressors," Ph.D. Thesis, Engineering Department, University of Cambridge, April 1980.

2. Fujita, H. and Takata, H., "A Study on Configurations of Casing Treatment for Axial Flow Compressors," Bulletin of the JSME, Vol. 27, No. 230, August 1984, pp. 1675-1681.

3. Prince, D.C., Jr., Wisler, D.C., and Hilvers, D.E., "Study of Casing Treatment Stall Margin Improvement Phenomena," NASA CR-134552, March 1974.

4. Greitzer, E.M., Nikkanen, J.P., Haddad, D.E., Mazzawy, R.S., and Joslyn, H.D., "A Fundamental Criterion for the Application of Rotor Casing Treatment," ASME J. Fluids Eng., Vol. 101, June 1979, pp. 237-243.

5. Smith, G.D.J. and Cumpsty, N.A., "Flow Phenomena in Compressor Casing Treatment," ASME J. Gas Turbines and Power, Vol. 107, April 1985, pp. 532-541.

6. Cheng, P., Prell, M.E., Greitzer, E.M., and Tan, C.S., "Effects of Compressor Hub Treatment on Stator Stall Margin and Performance," J. Aircraft, Vol. 21, No. 7, July 1984, pp. 469-475.

7. Takata, H. and Tsukuda, Y., "Stall Margin Improvement by Casing Treatment - Its Mechanism and Effectiveness," ASME J. Eng. Power, Vol. 99, January 1977, pp. 121-133.

8. Cheng, P., "Effects of Compressor Hub Treatment on Stator Stall and Pressure Rise," MIT GTL Report No. 167, September 1982.

9. Johnson, M.C., "The Effects of Hub Treatment on Compressor Endwall Flowfields," M.S. Thesis, Department of Aeronautics and Astronautics, MIT, January 1985.

10. Johnson, M.C. and Greitzer, E.M., "Effects of Slotted Hub and Casing Treatments on Compressor Endwall Flowfields," ASME Paper 86-GT-247.

11. Prell, M.E., "An Experimental Investigation of Stator Hub Treatment in an Axial Flow Compressor," MIT GTL Report No. 161, July 1981.

12. Owen, E. and Pankhurst, R.C., The Measurement of Airflow, 5th edition, Ch. 7, Pergamon Press, 1977.

13. Koch, C.C., "Experimental Evaluation of Outer Case Blowing or Bleeding of Single Stage Axial Flow Compressor," Part VI - Final Report, NASA CR-54592, January 30, 1970.

14. Covert, E., Private Communications, October 1986.

15. Koch, C.C., "Stalling Pressure Rise Capability of Axial Flow Compressor Stages," ASME J. Eng. Power, Vol. 103, October 1981, pp. 645-656.

16. Fink, D.A., unpublished MIT GTL Report, 1987.

17. Wagner, J.H. and Okishi, T.H., "Analysis of Multistage, Axial Flow Turbomachine Wake Production, Transport, and Interaction," Department of Mechanical Engineering, Iowa State University, ISU- ERI-AMES-78173, December 1977.

18. Schmidt, D.P. and Okishi, T.H., "Multistage Axial Flow Turbomachine Wake Production, Transport and Interaction," AFOSR-TR-77-0720, November 1976.

19. Hunter, I.H. and Cumpsty, N.A., "Casing Wall Boundary-Layer Development Through an Isolated Compressor Rotor," ASME J. Eng. Power, Vol. 104, October 1982, pp. 805-817.

TABLE 1
FLOWPATH GEOMETRY

	Rotor	Stator
Hub diameter (mm)	444	444
Casing diameter (mm)	597	597
Number of blades	44	45
Chord (mm)	38	38
Solidity at midspan	1.0	1.0
Aspect ratio	1.9	1.9
Camber (deg)	30	30
O.D. stagger angle (deg)	65	40
Midspan stagger angle (deg)	60	42.5
I.D. stagger angle (deg)	55	45
Blade clearance (mm)	0.8	1.5

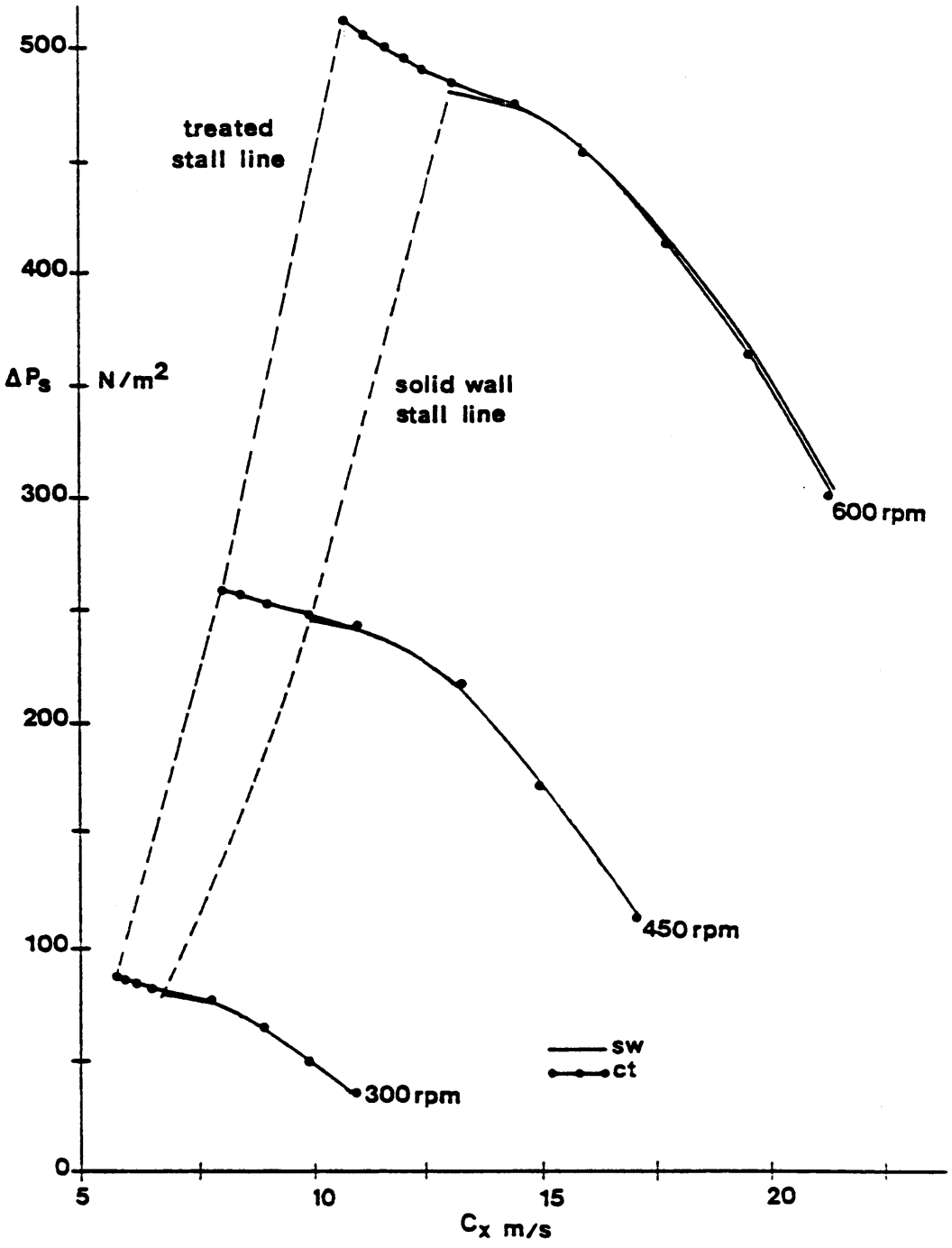

Fig. 1: Stall lines for smooth wall and treated wall, from [1]

TYPES OF COMPRESSOR STALL

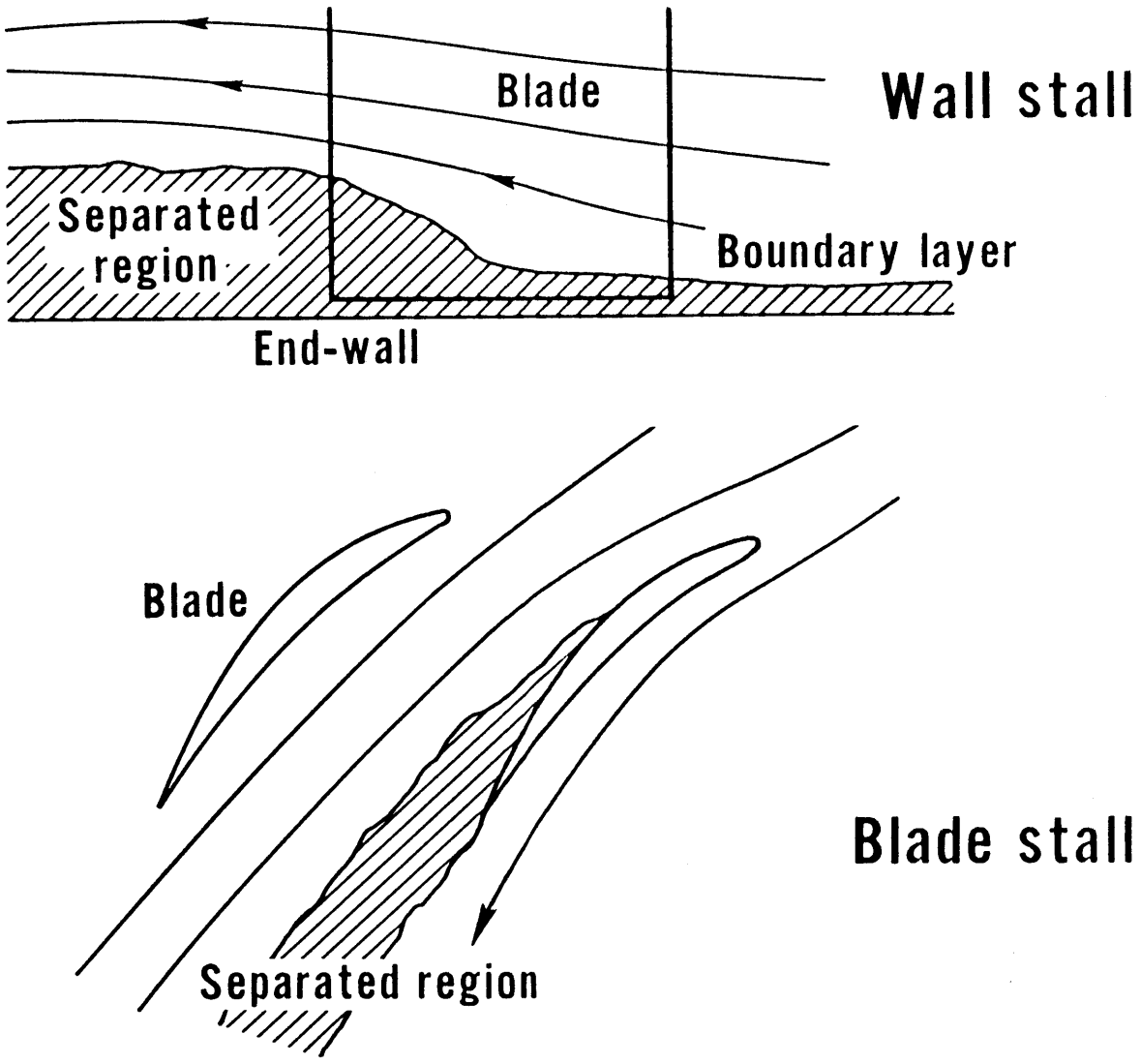

Fig. 2: Blade stall and wall stall

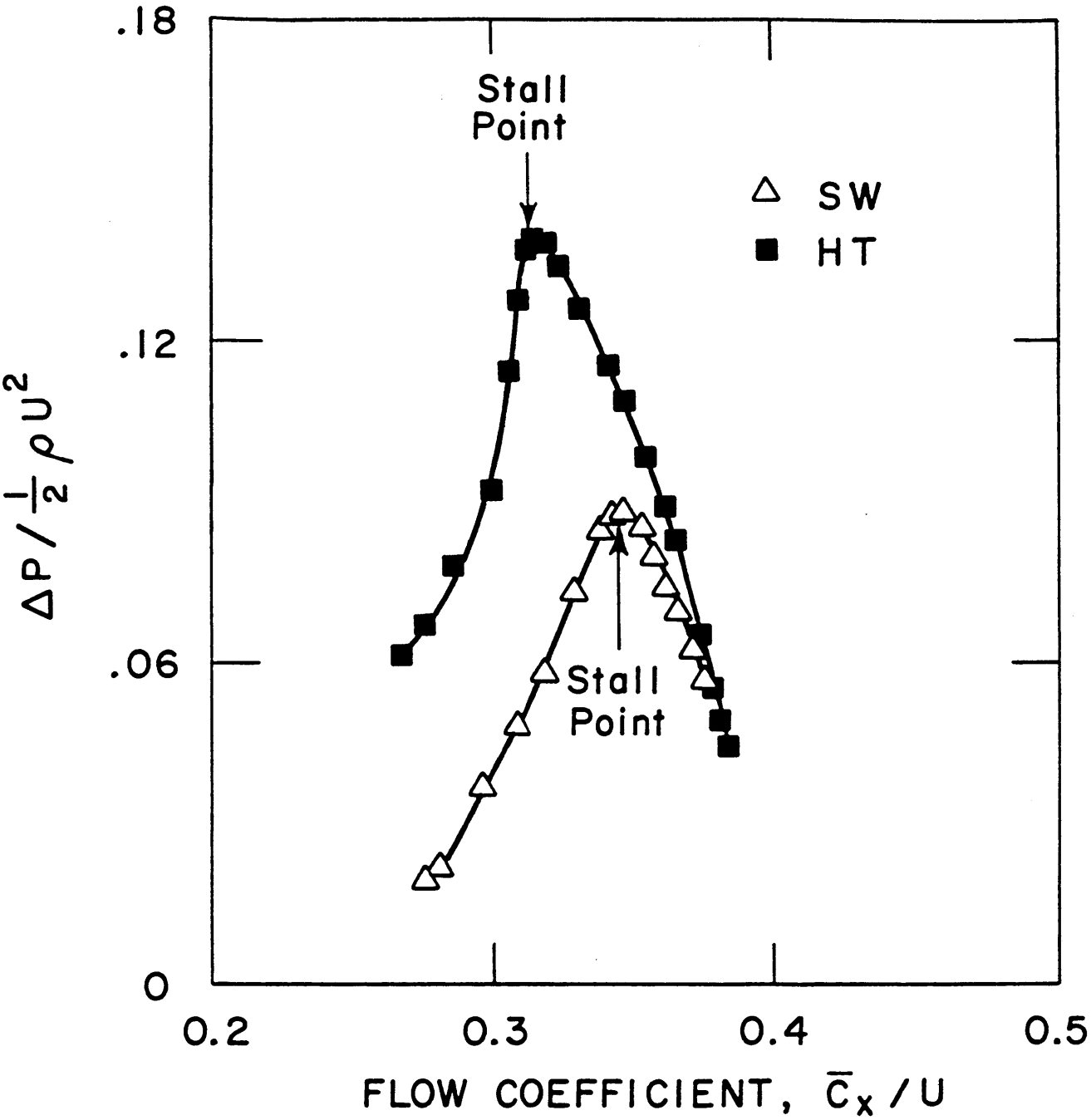

Fig. 3: Stator static pressure rise characteristics for smooth wall (SM) and hub treatment (HT), from [8]

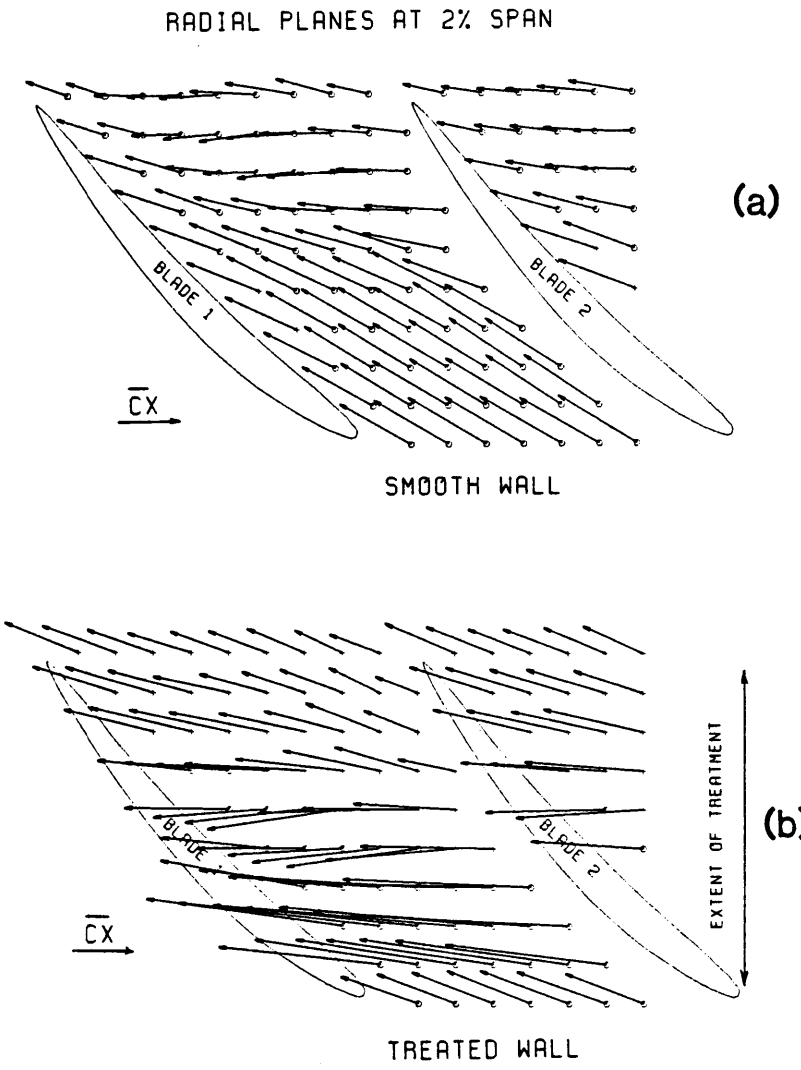

Fig. 4: Velocity field at 2% span from hub

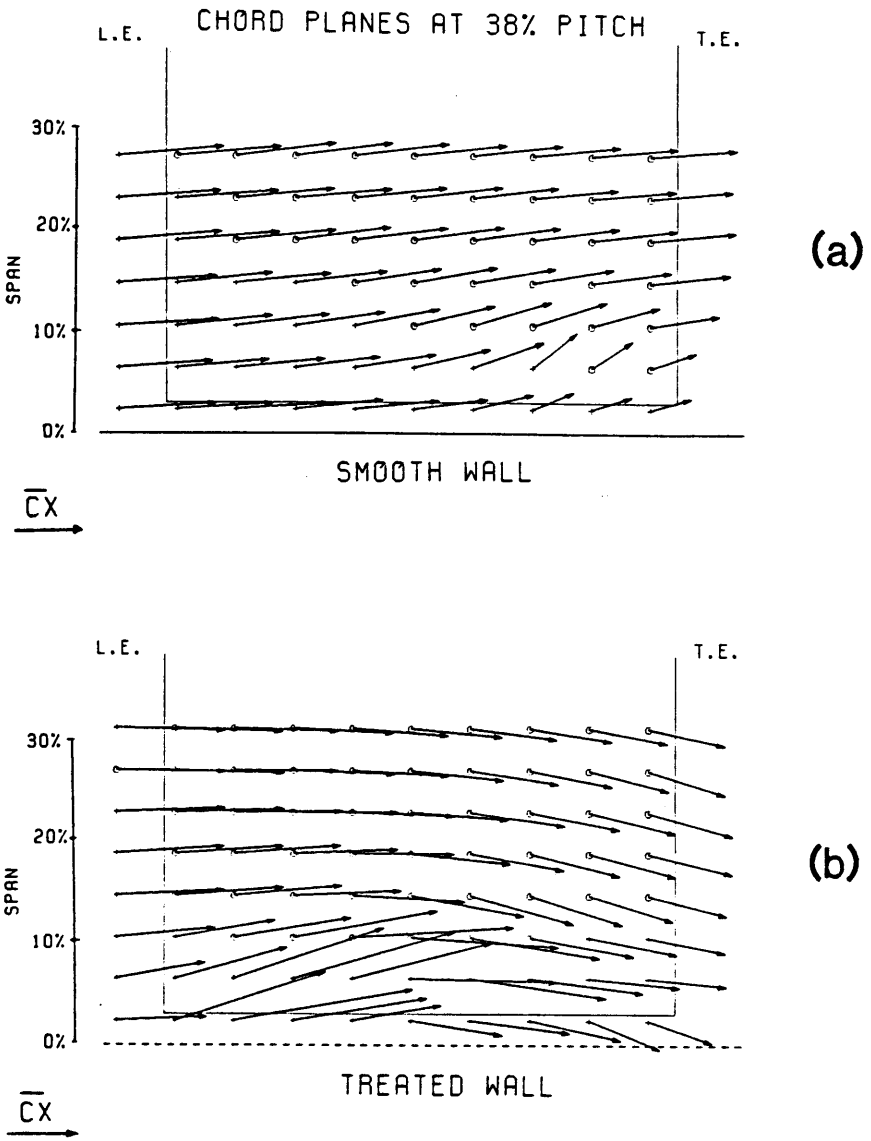

Fig. 5: Velocity field at 38% pitch from blade 1, from [9]

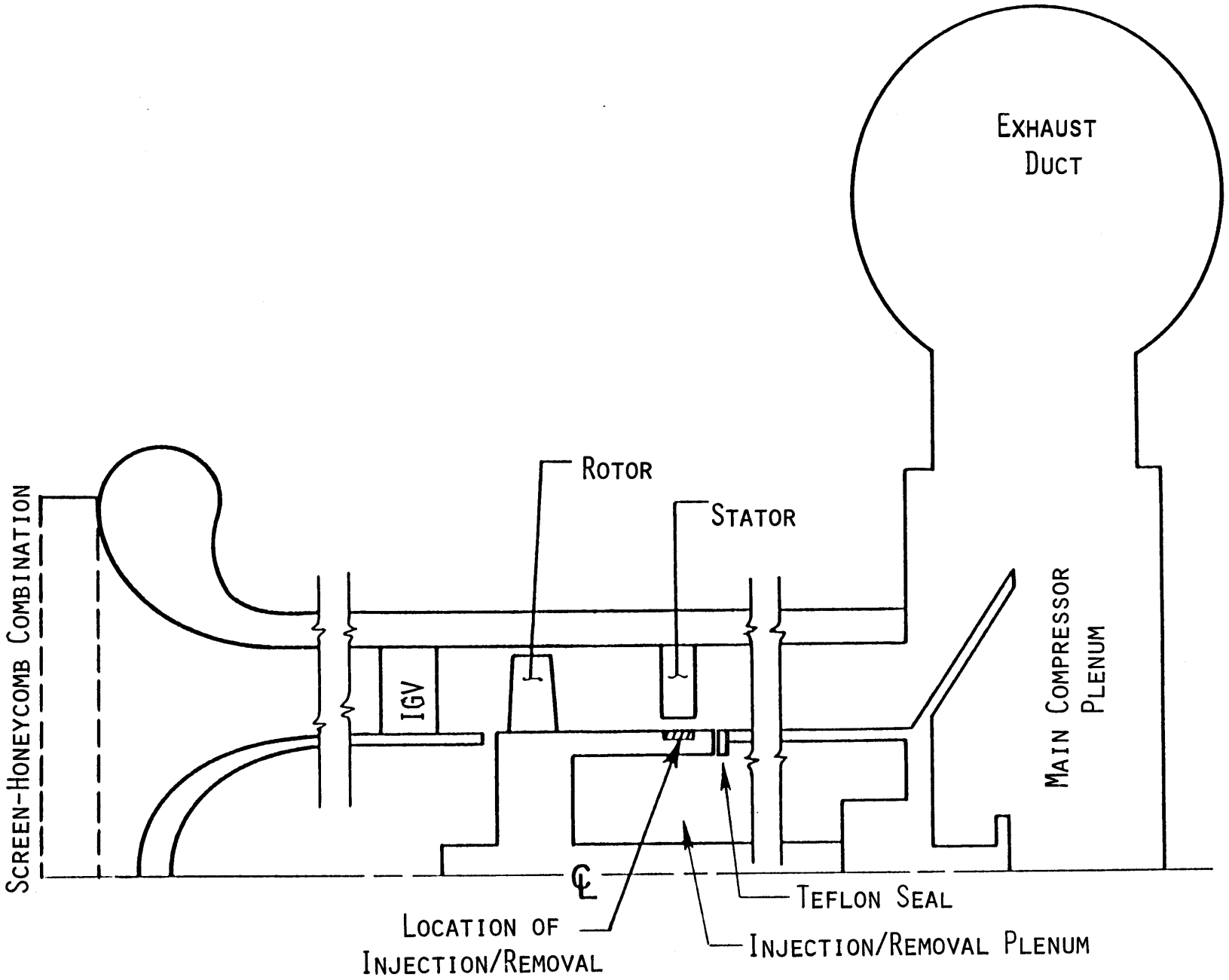

Fig. 6: Schematic drawing of compressor

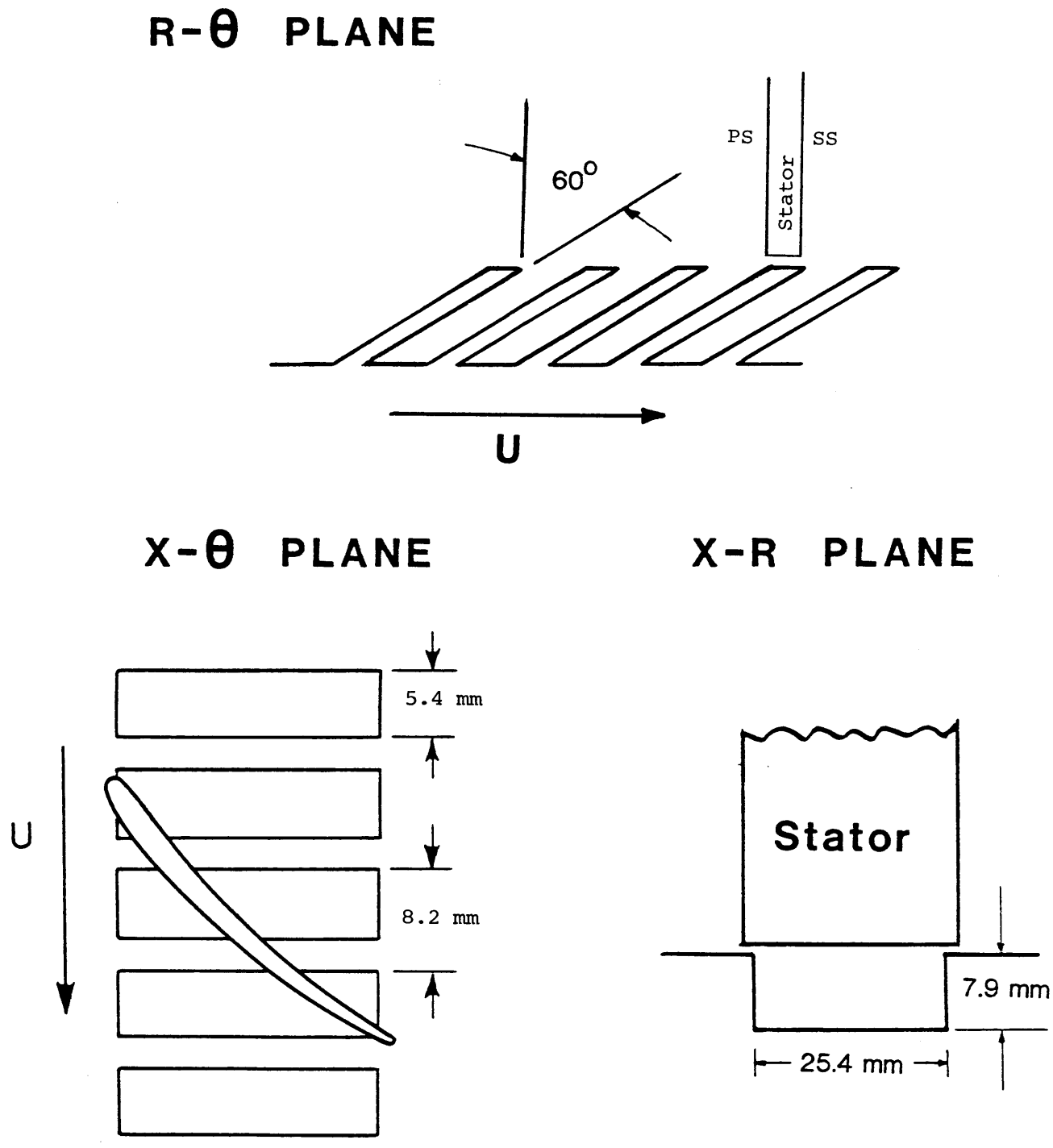

Fig. 7: Geometry of Johnson's hub treatment slots

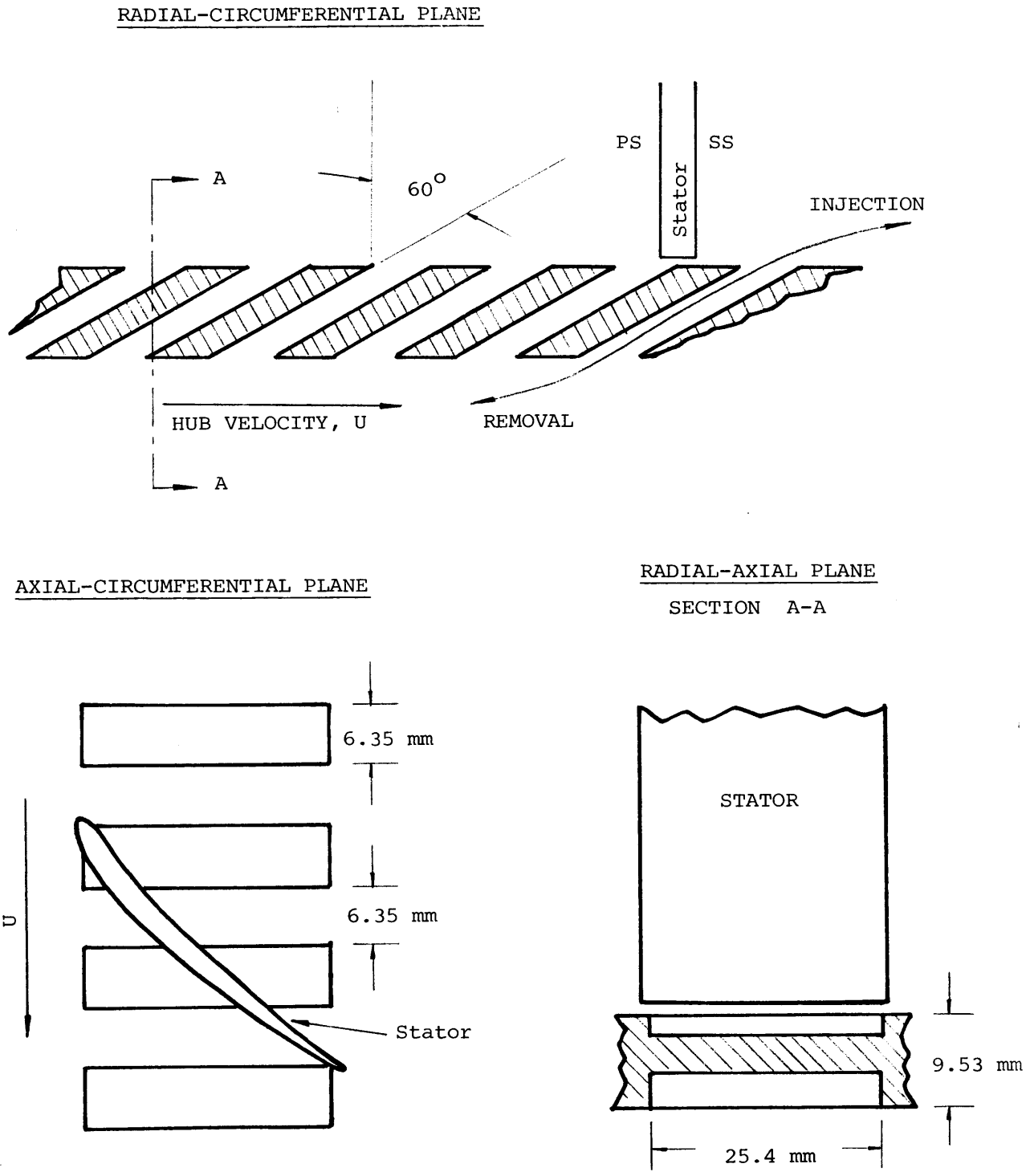

Fig. 8: Geometry of the full 90% slots

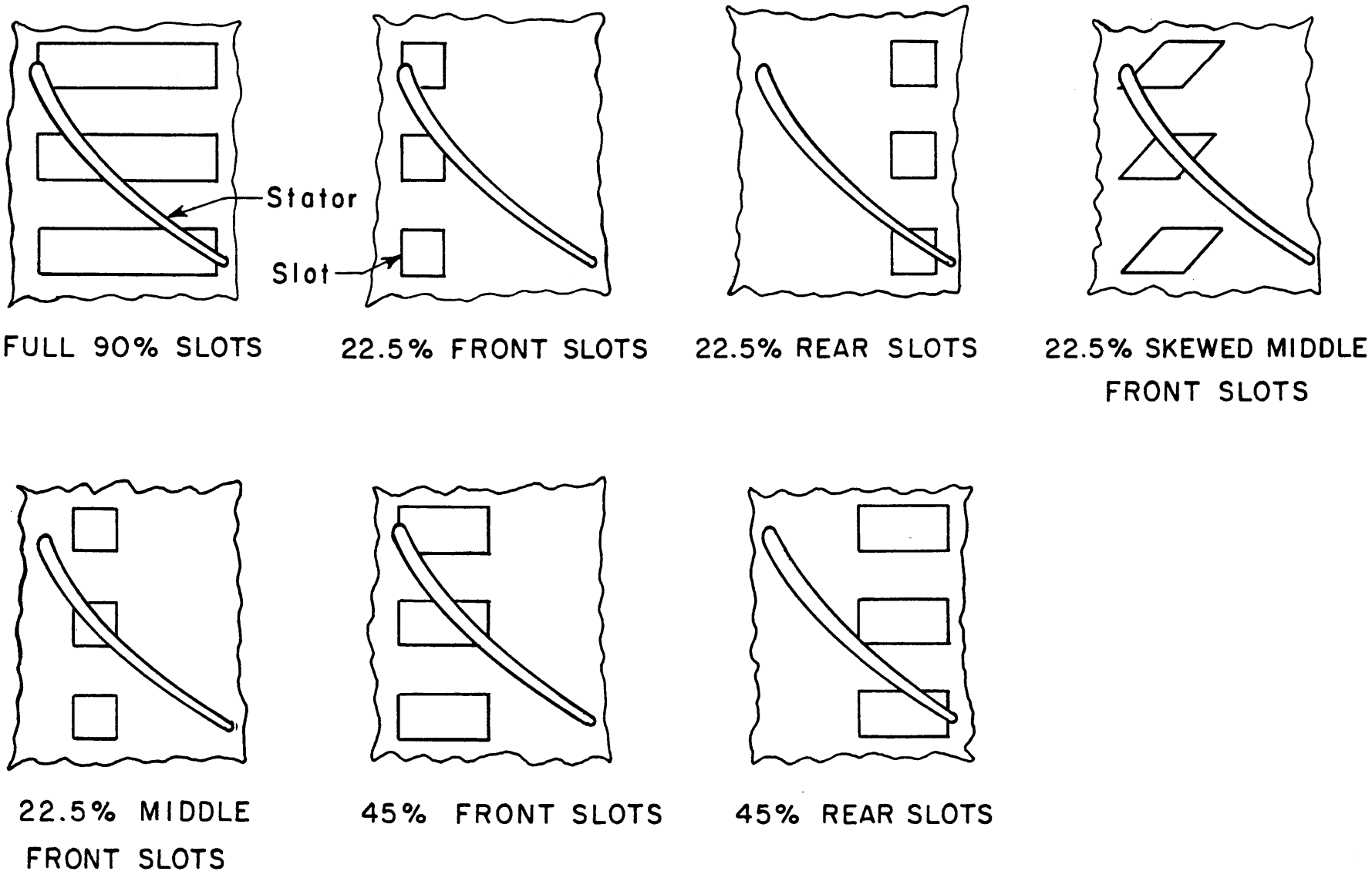

Fig. 9: Locations of slots

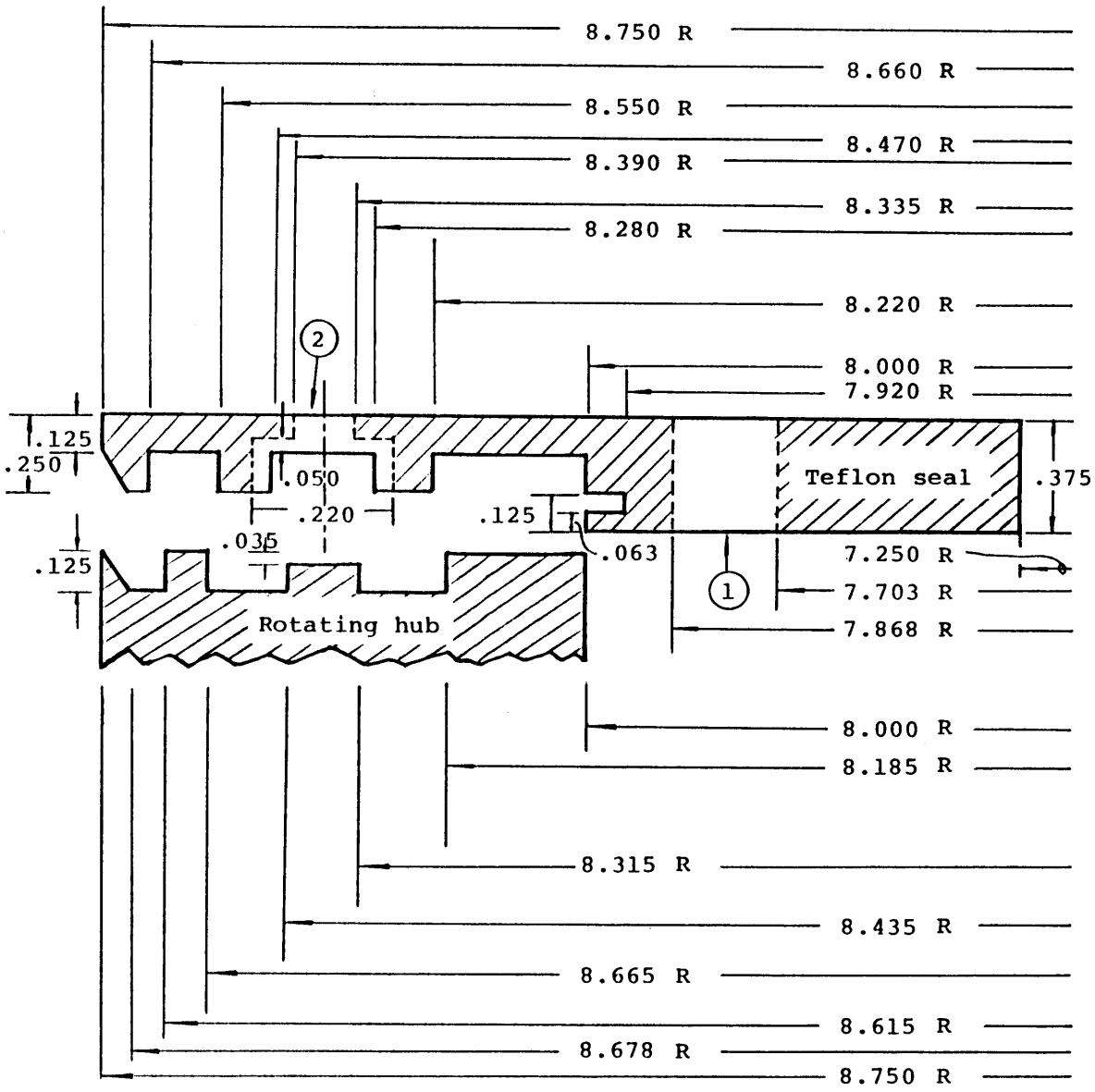

1 Eighteen Clearance Holes, equally spaced
2 Eighteen Countersunk Holes, each is located midway between two adjacent Clearance Holes

ALL DIMENSIONS ARE IN INCHES

Fig. 10: Geometry of seal

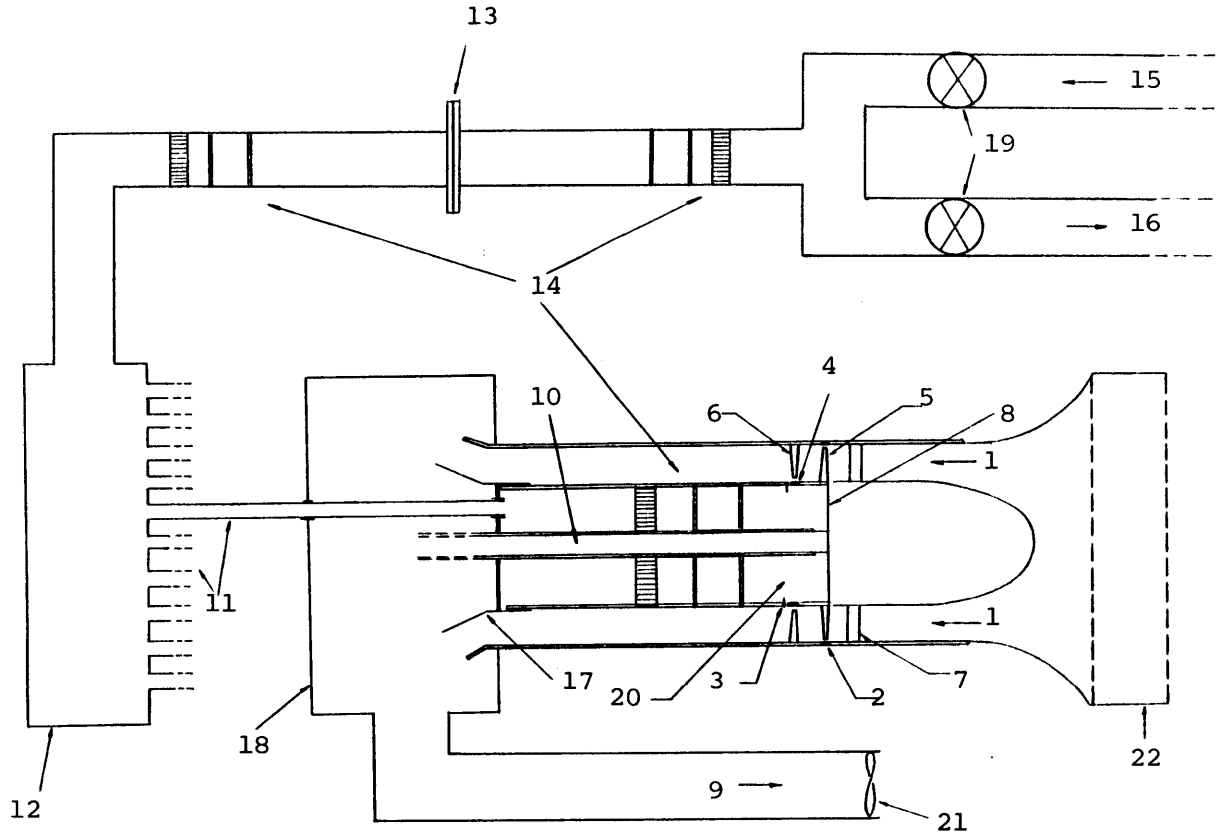

1 Compressor Inlet
2 Casing Treatment
3 Teflon Seal
4 Location of Injection/Removal
5 Rotor
6 Stator
7 Inlet Guide vanes
8 Rotating Hub
9 Exhaust Duct
10 Shaft
11 Ten hoses
12 Manifold
13 Orifice
14 Flow Straighteners and Smootheners
15 From air Supply Compressor
16 To Steam Ejector
17 Discharge Valve
18 Main Compressor Plenum
19 Butterfly Valves
20 Injection/Removal Plenum
21 Downstream Fan
22 Screen-Honeycomb Combination

Fig. 11: Schematic drawing of flow injection and removal system

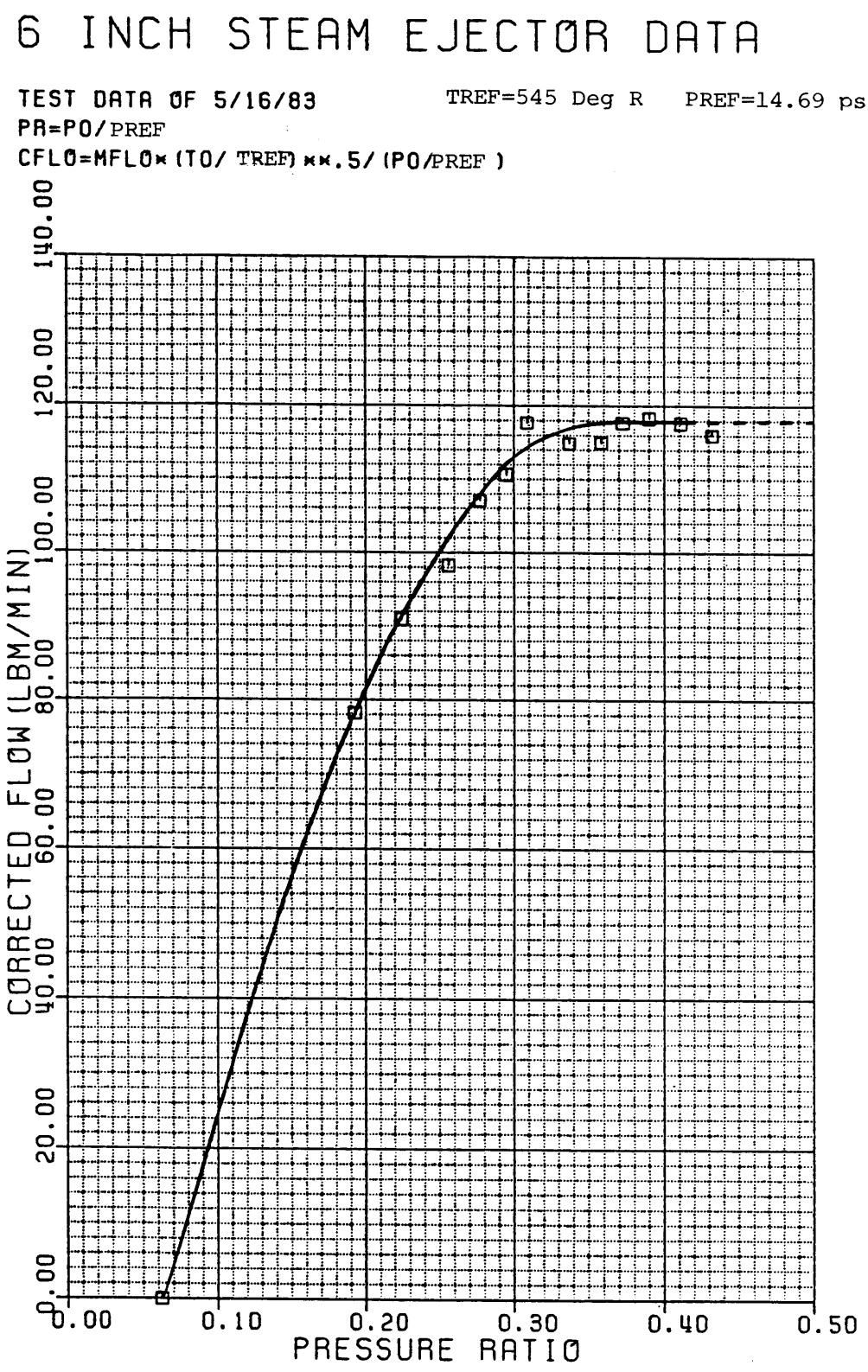

Fig. 12: GTL steam ejector pressure-mass flow characteristics (from [16])

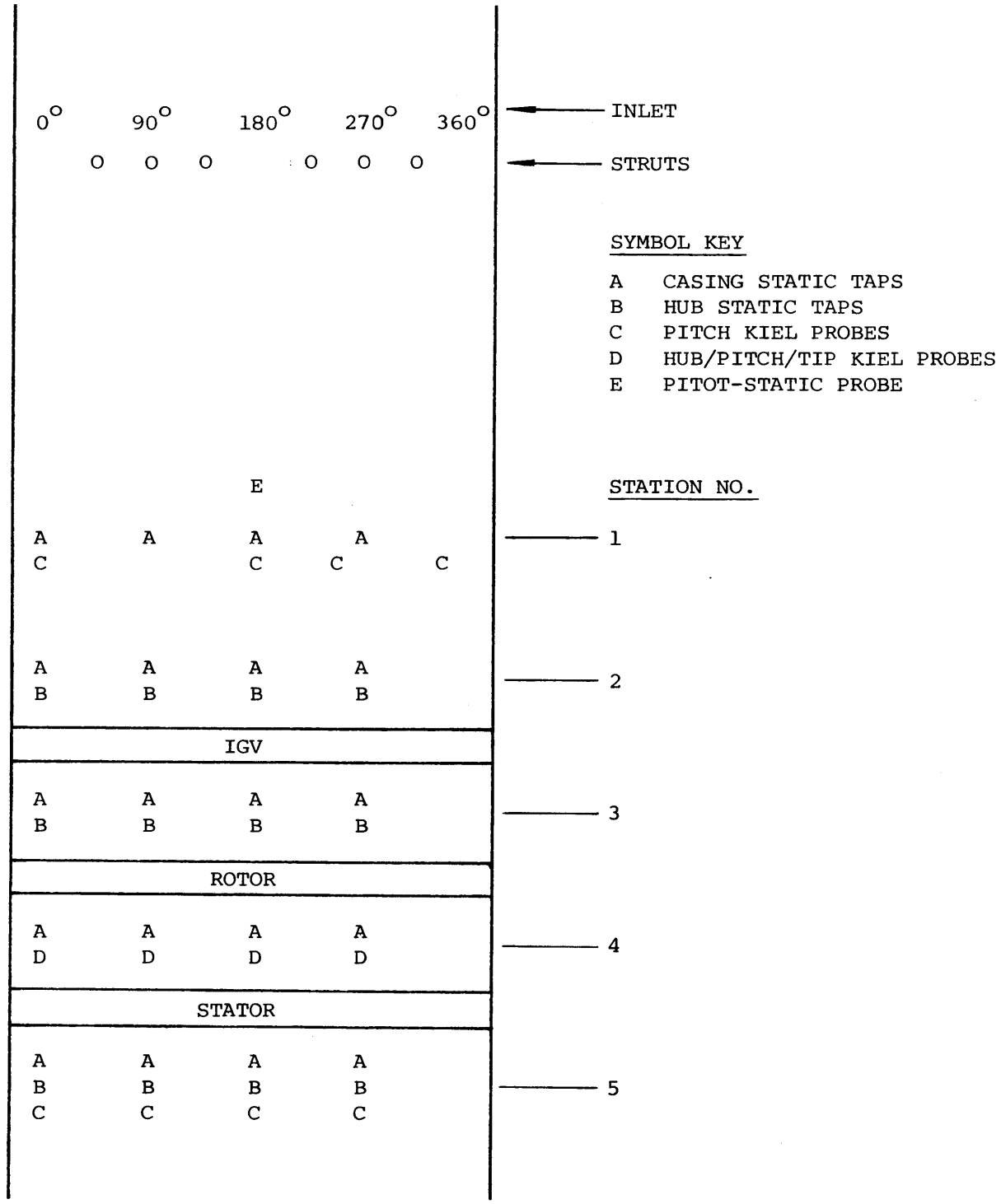

Fig. 13: Locations of pressure taps on compressor

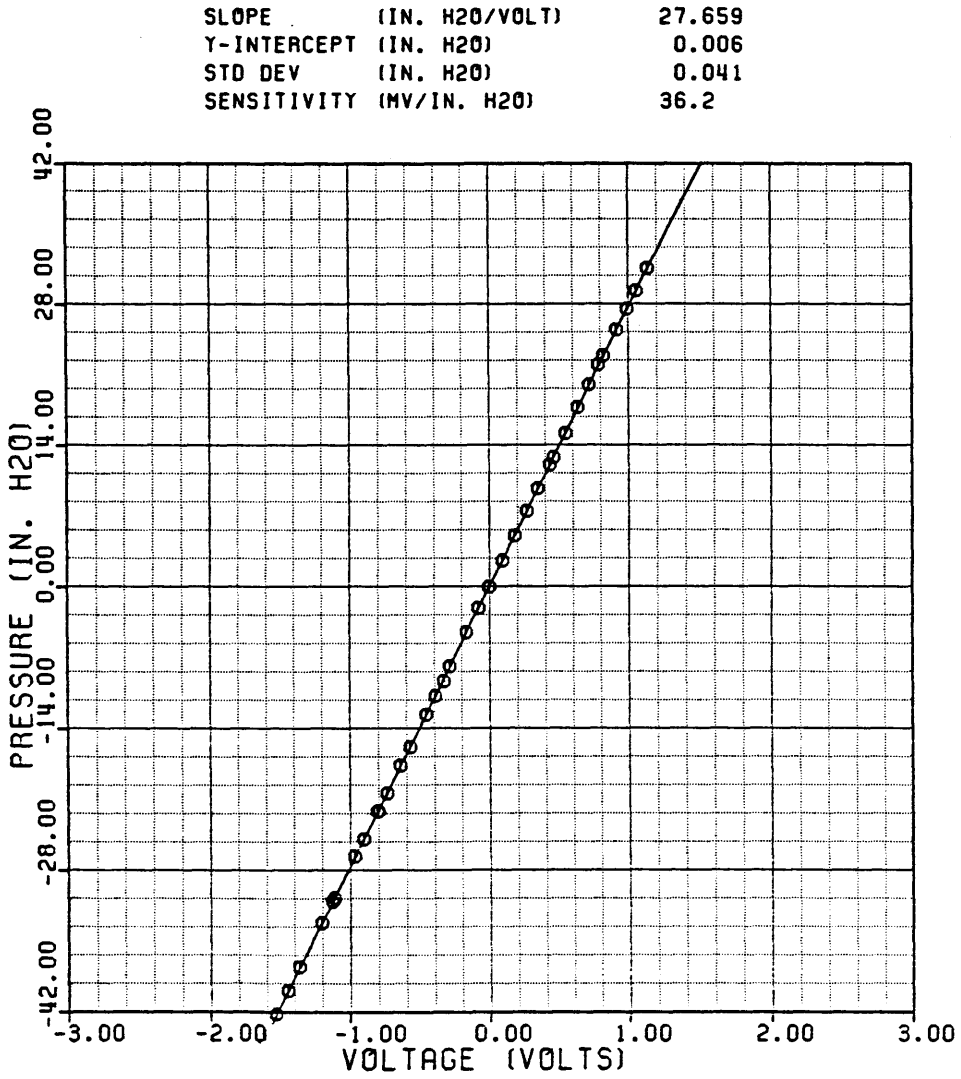

Fig. 14: Scanivalve transducer calibration

GRID LOCATIONS

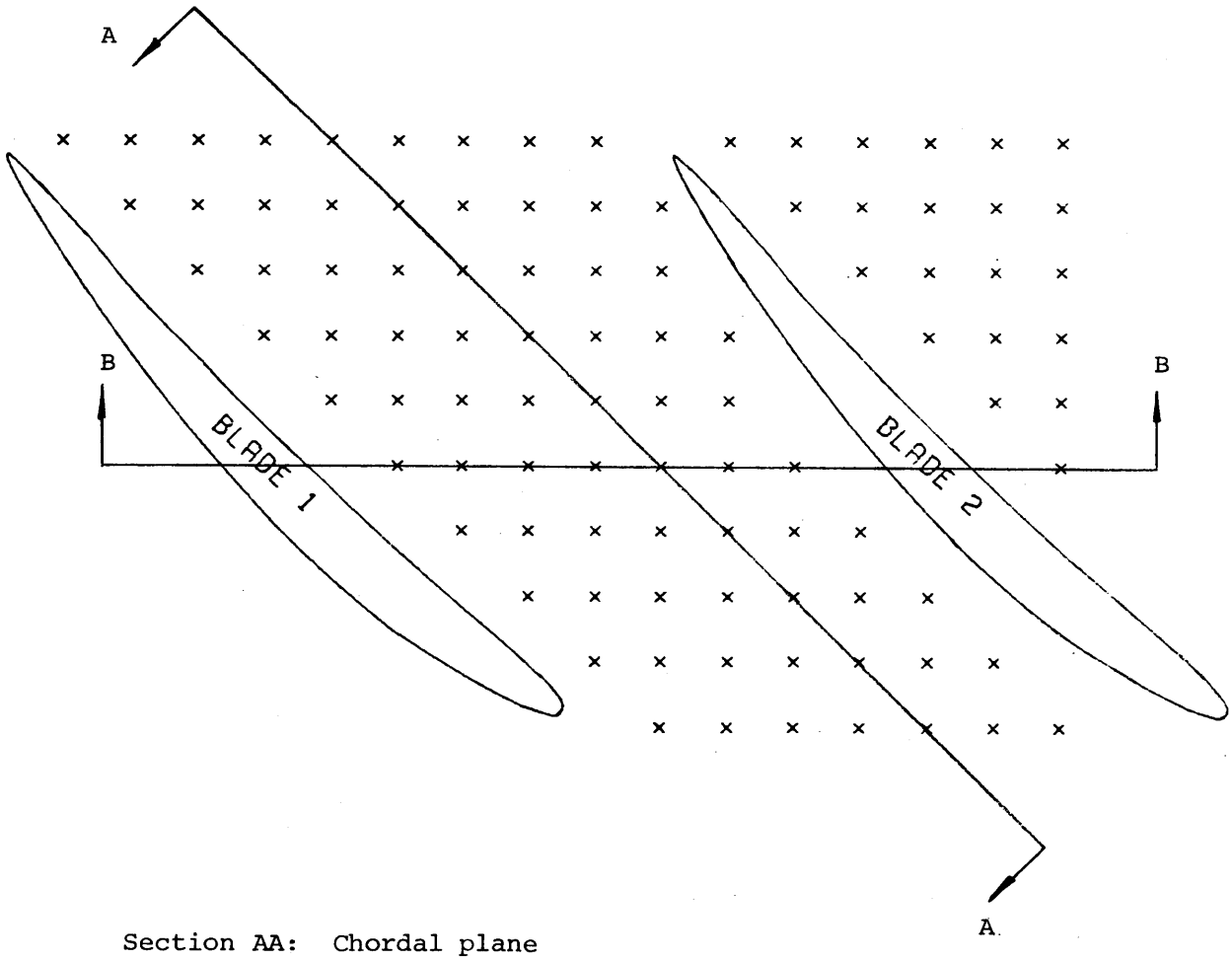

Section AA: Chordal plane

Section BB: Axial plane

Fig. 15: Radial plane, also showing sections of chordal and axial planes

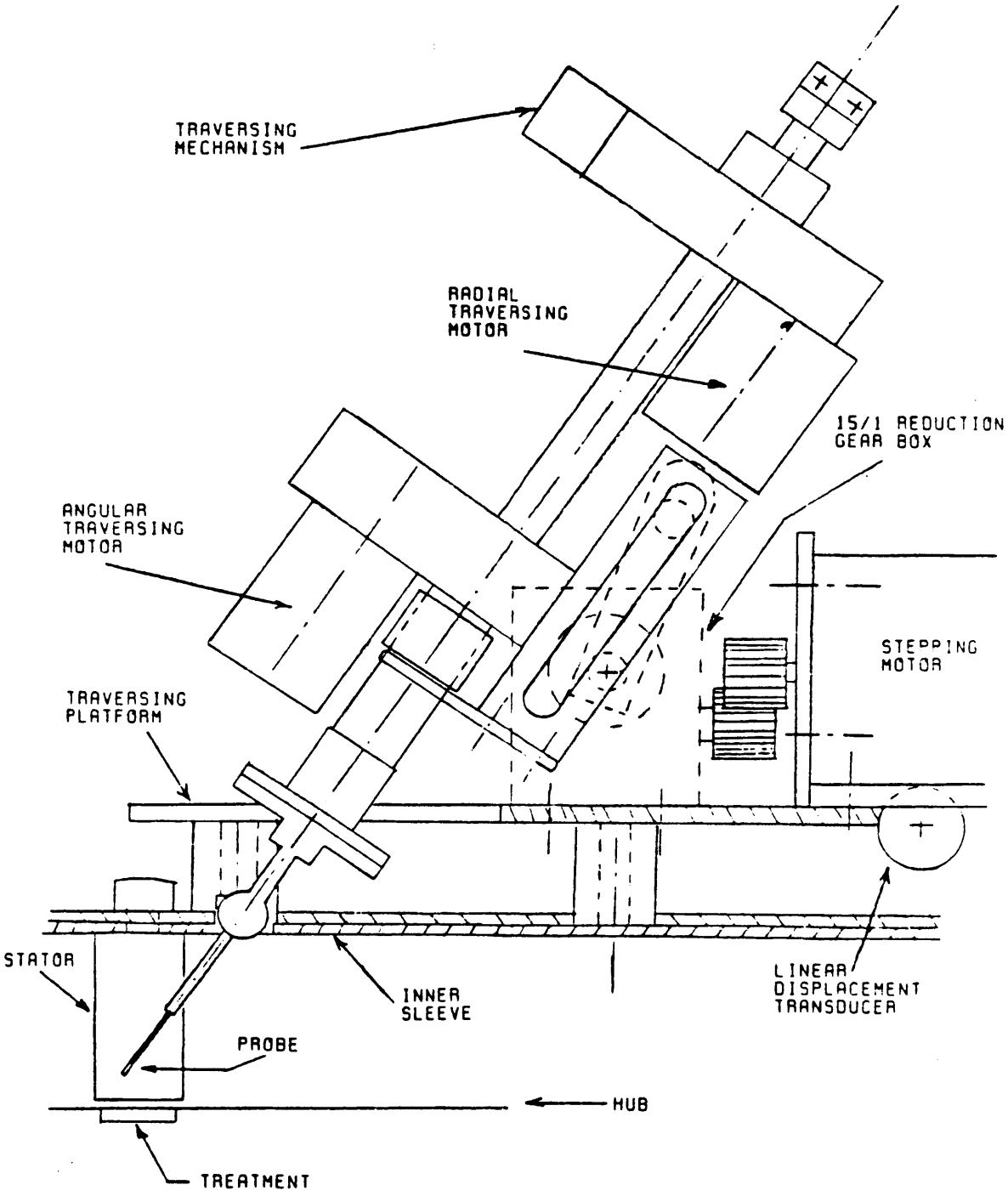

Fig. 16: Side view of positioning system

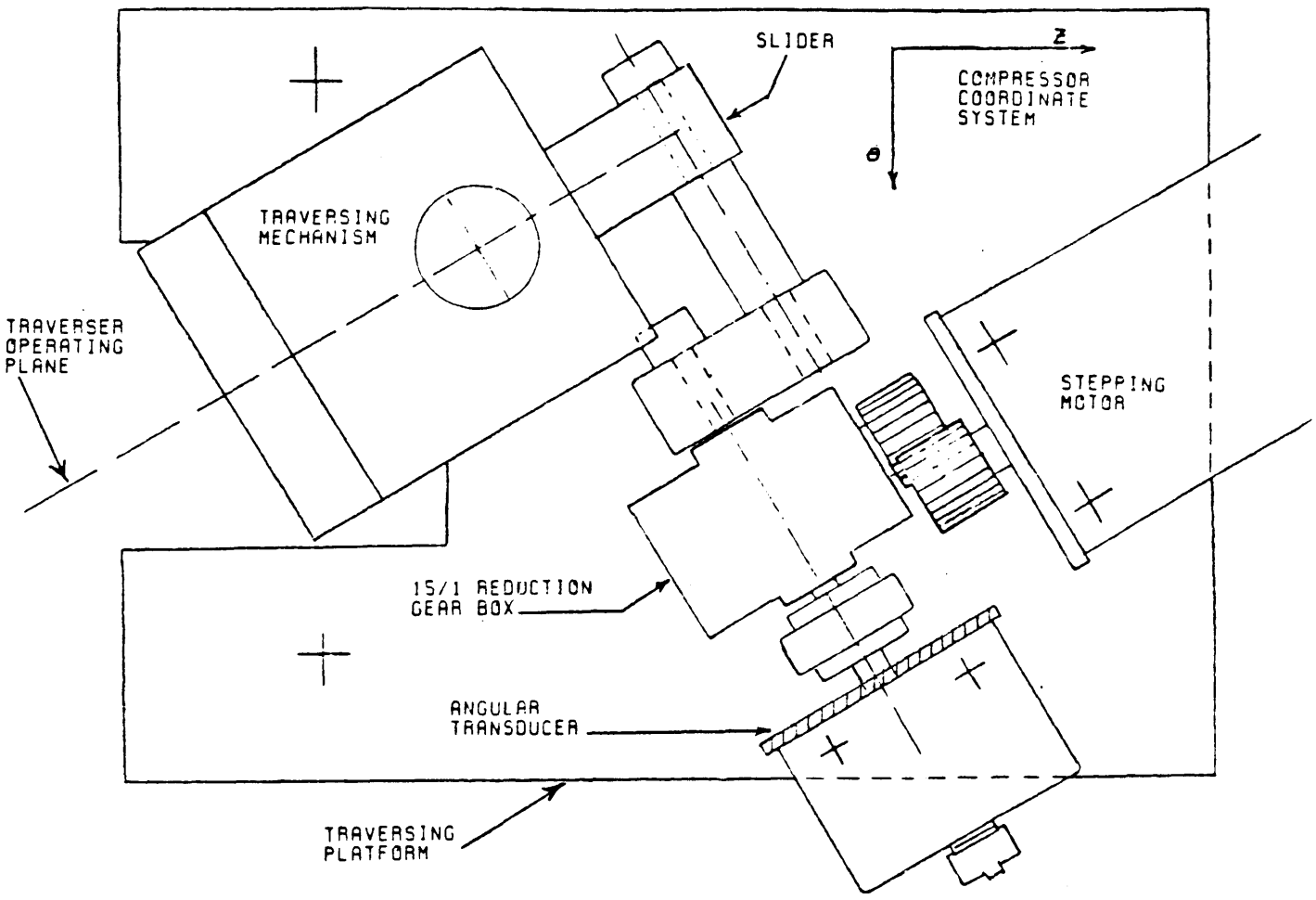

Fig. 17: Top view of positioning system

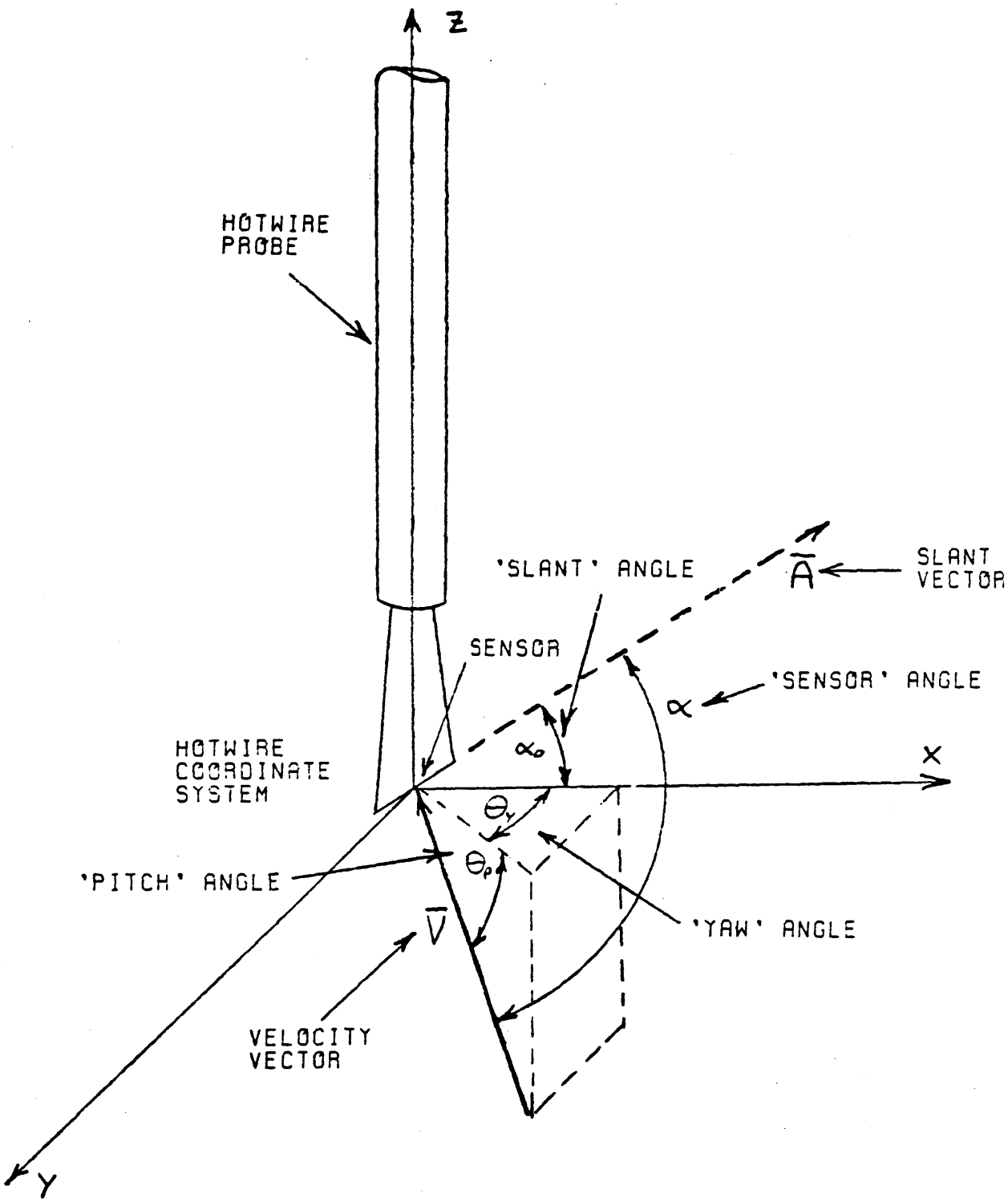

Fig. 18: Probe geometry

VELOCITY PROFILE FOR SUCTION

VELOCITY AT CENTRE (m/s)	19.22
REYNOLDS NUMBER	190311
MASS FLOW RATE (Kg/s)	0.153
DISCHARGE COEFFICIENT	0.641

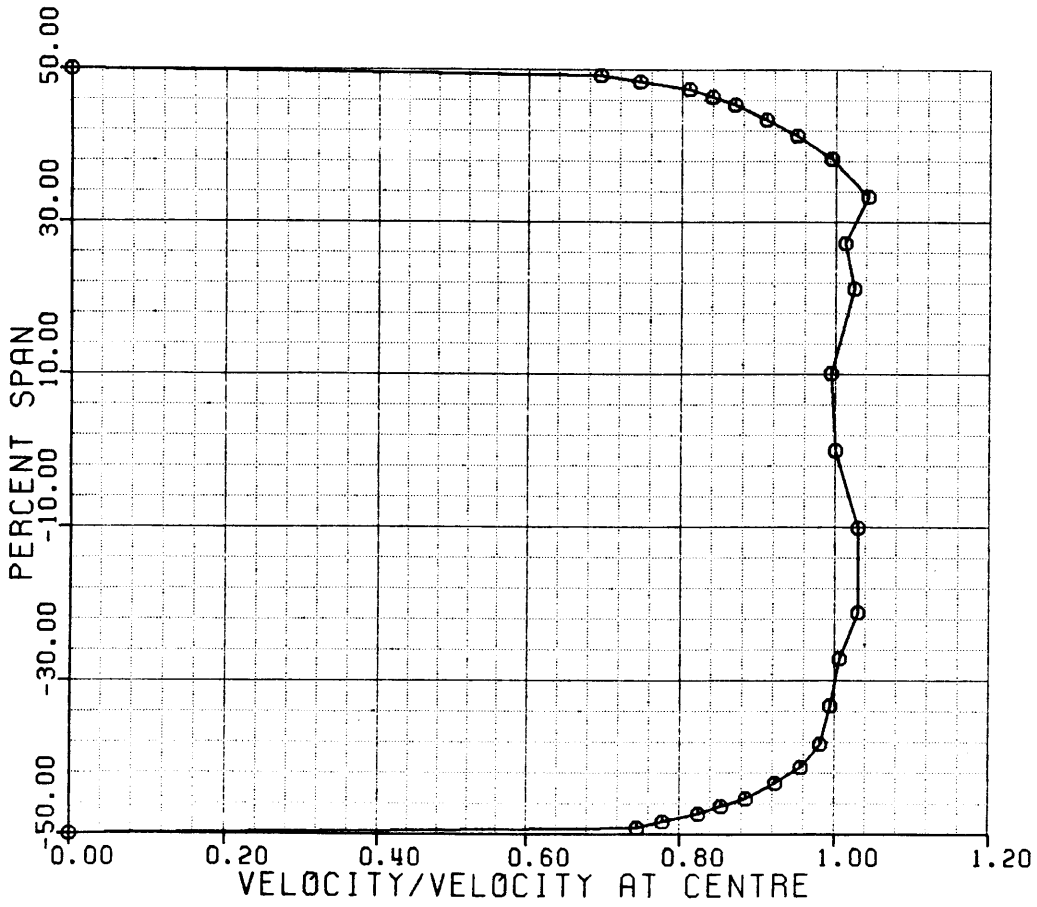

Fig. 19: Typical velocity profile of flow entering orifice

ORIFICE CALIBRATION FOR SUCTION

(Dis coeff= 1.000-0.2491*Re**.0299)

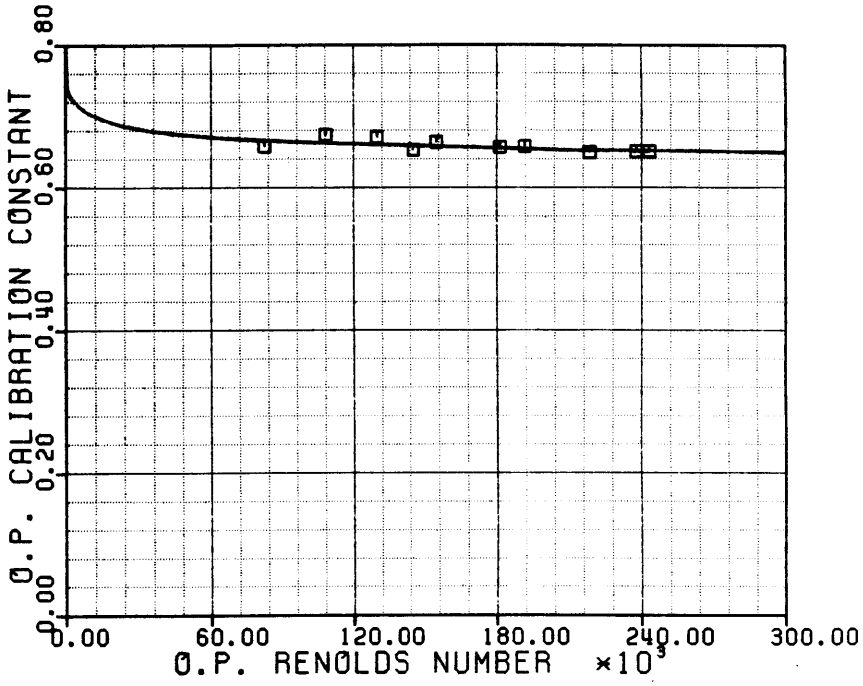

Fig. 20

ORIFICE CALIBRATION FOR BLOWING

(Dis coeff= 1.000-.1996*Re**.0447)

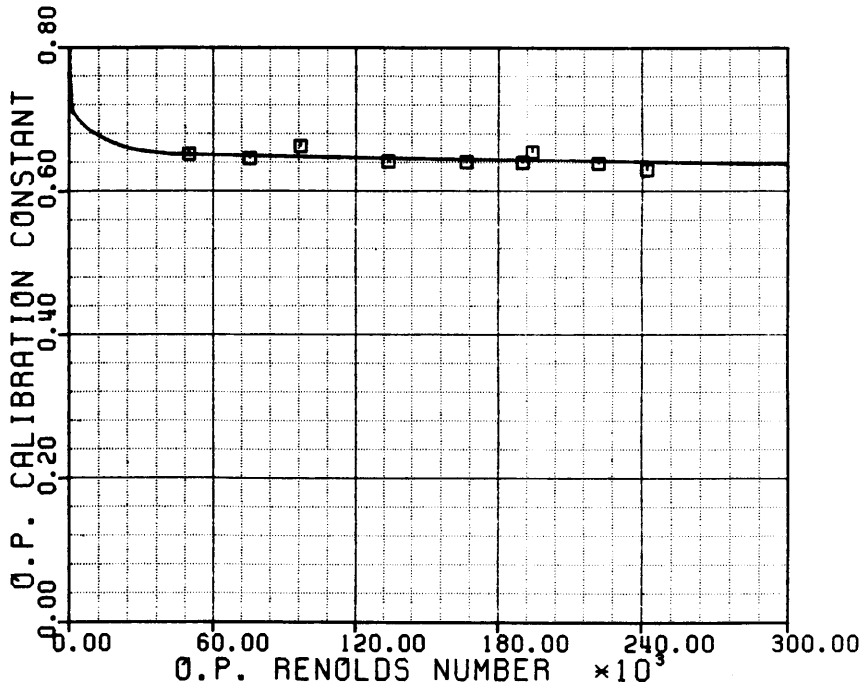

Fig. 21

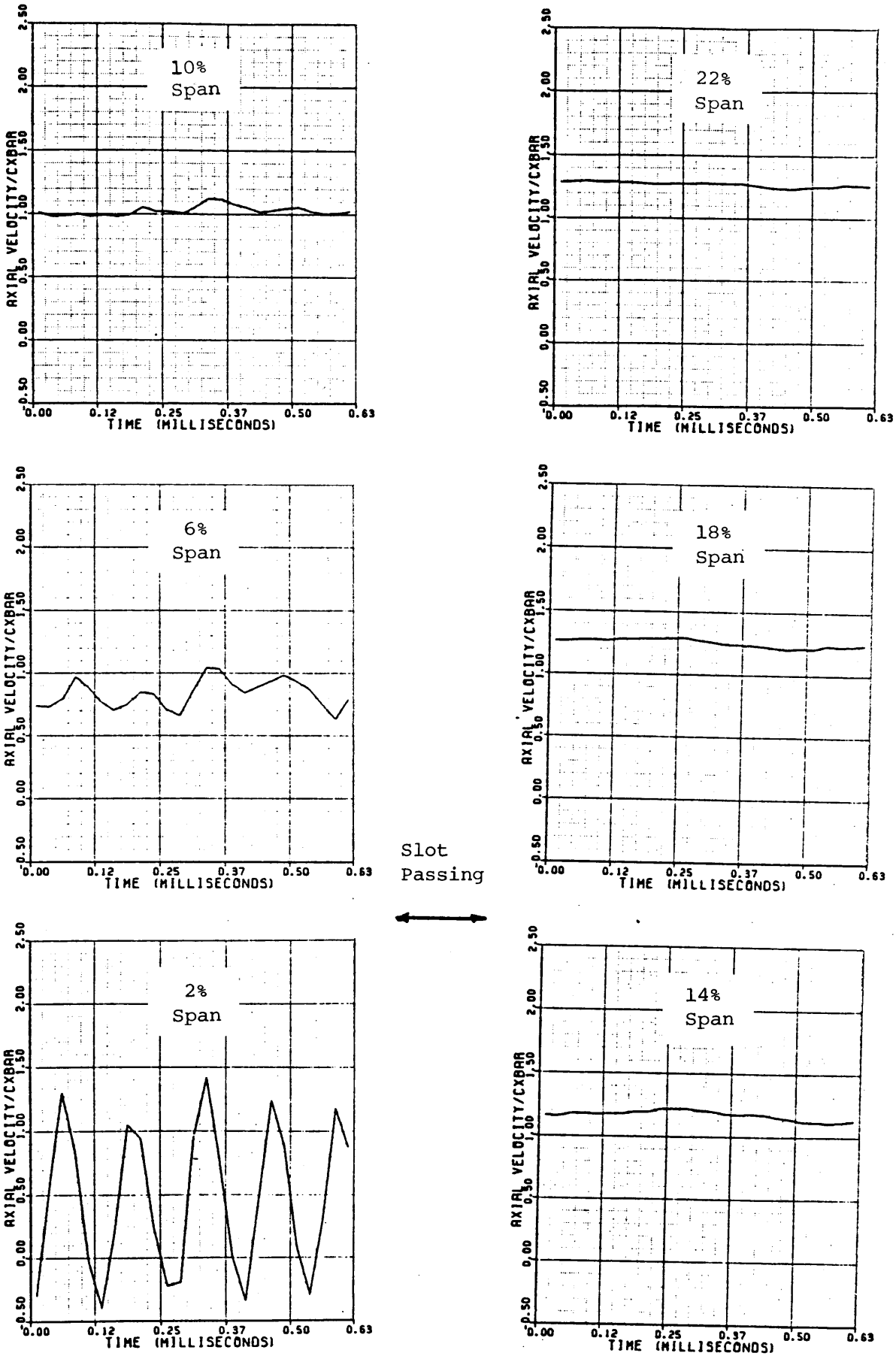

Fig. 22: Decay of axial unsteadiness near leading edge, from [9]

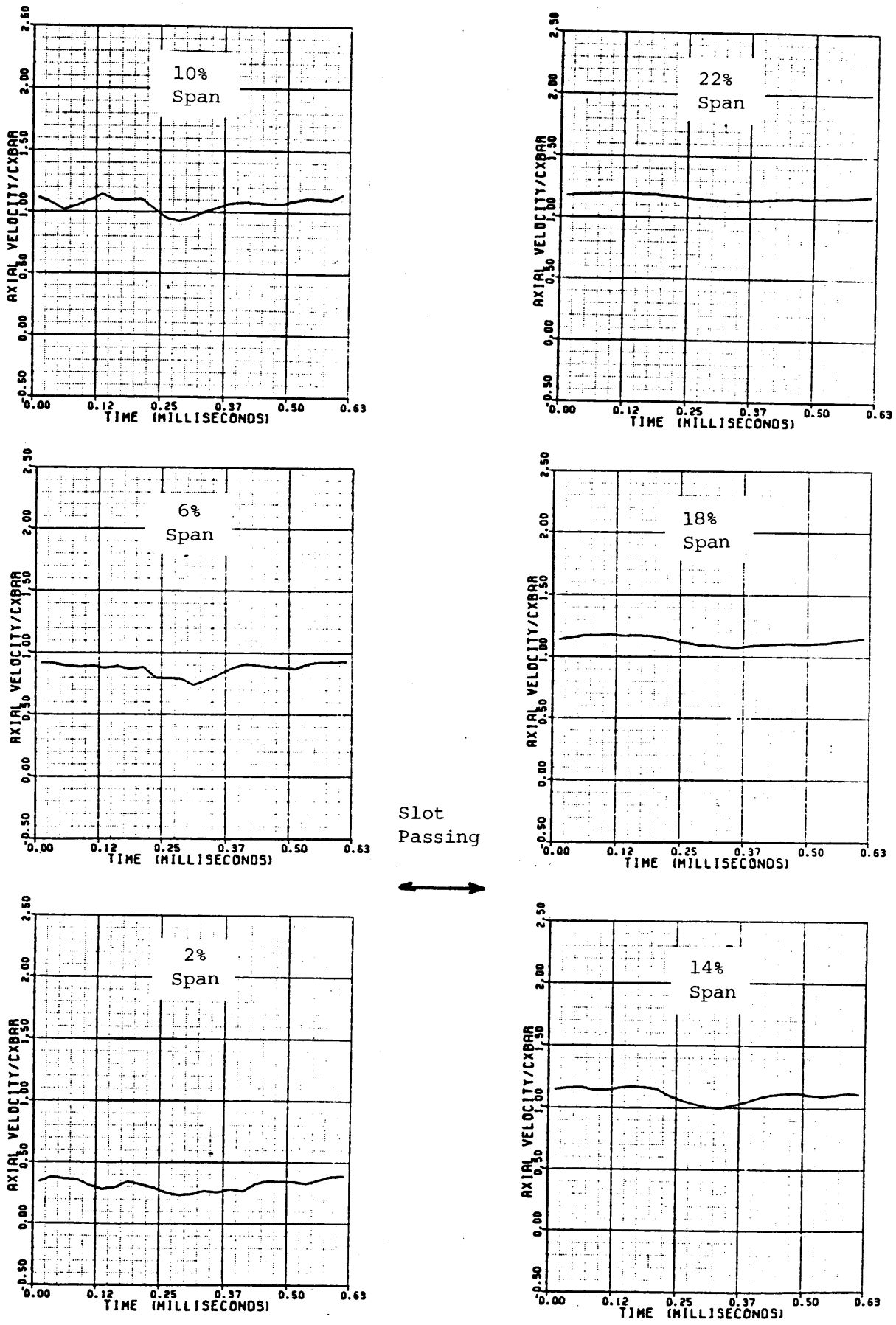

Fig. 23: Decay of axial unsteadiness near trailing edge, from [9]

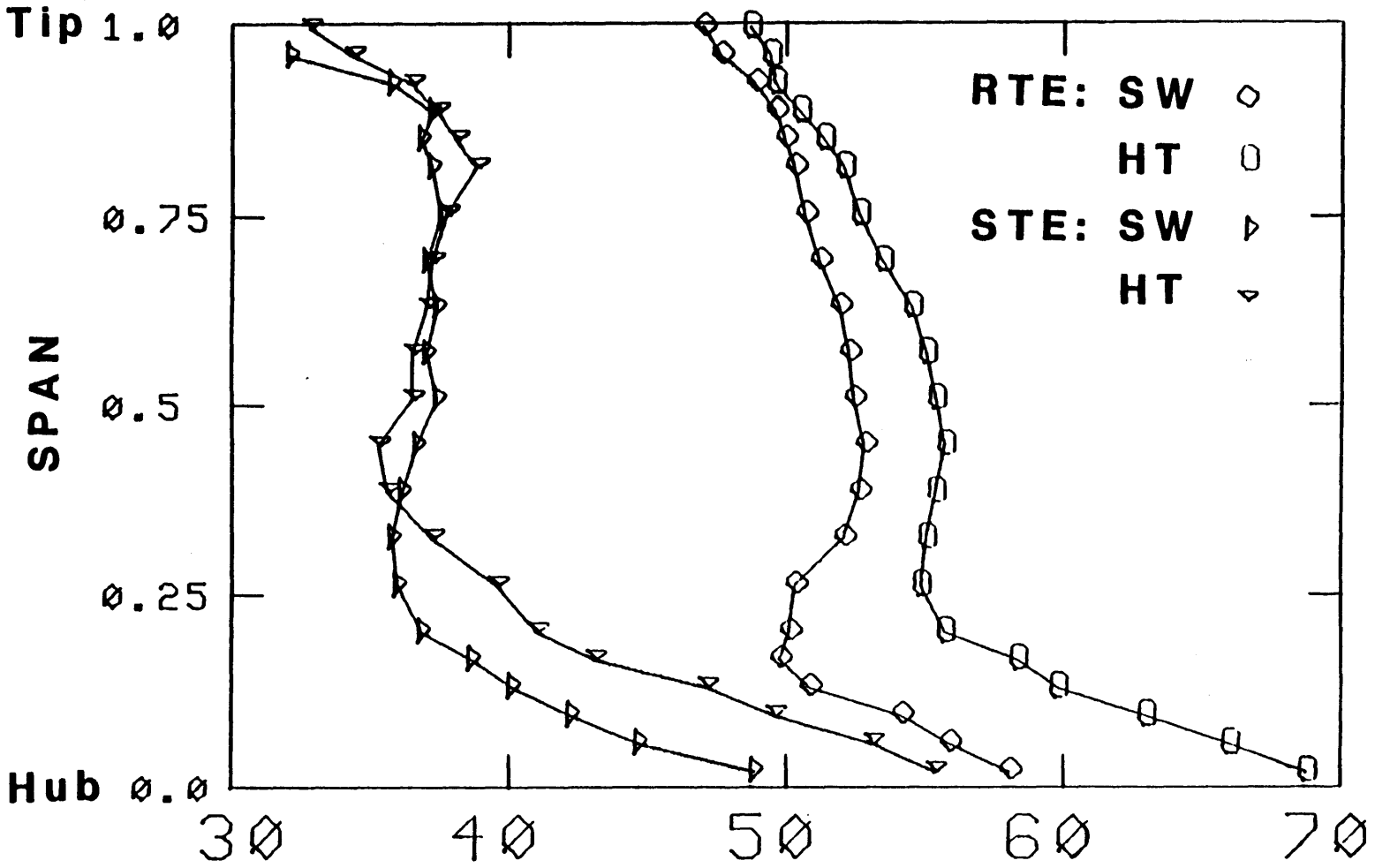

Fig. 24: Absolute stator inlet and exit angles:
SW (smooth wall) data taken at $\overline{C}_x/U = 0.345$
HT (hub treatment) data taken at $\overline{C}_x/U = 0.305$

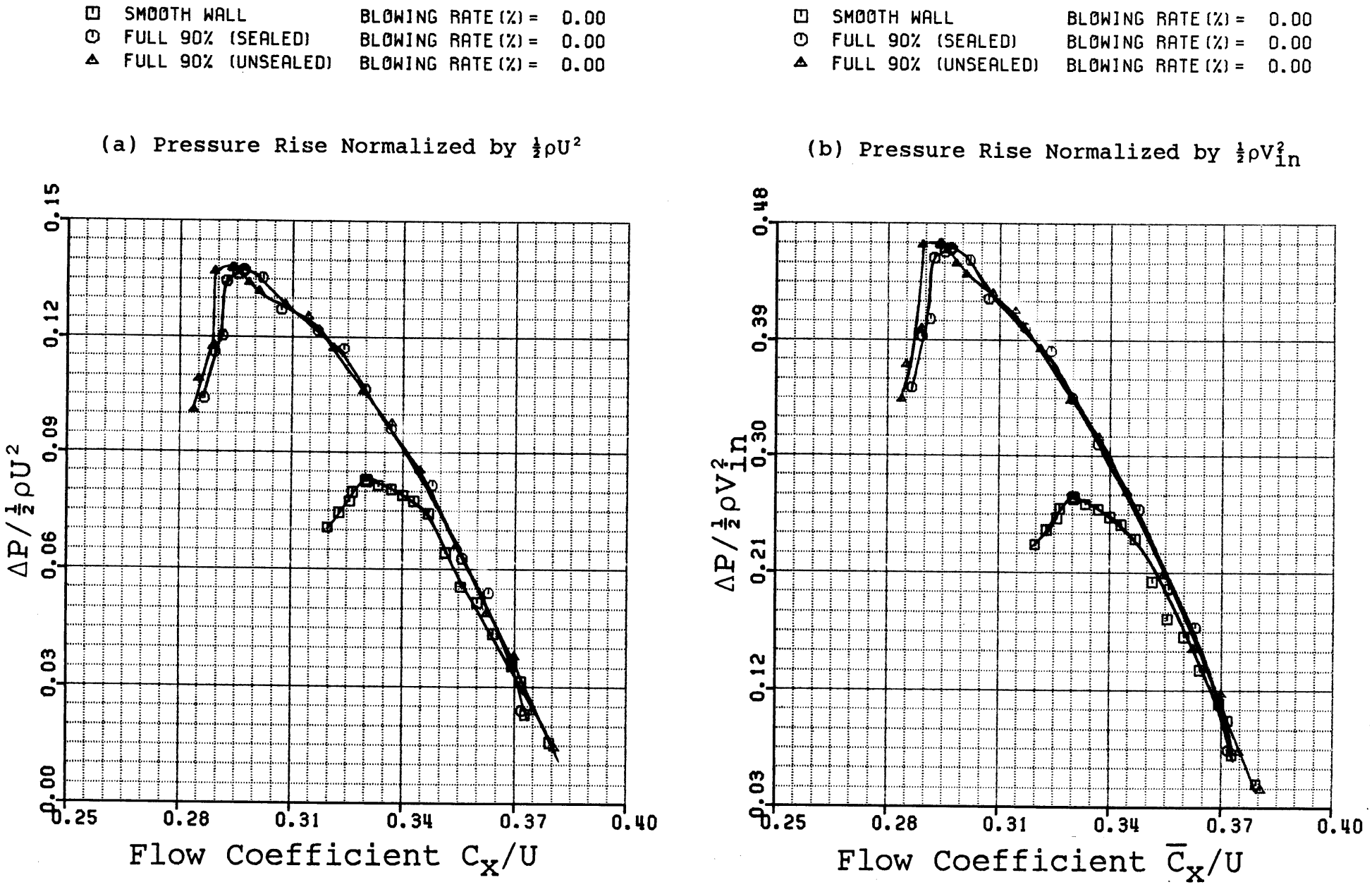

Fig. 25: Baseline stator static pressure rise: smooth wall and full 90% slots

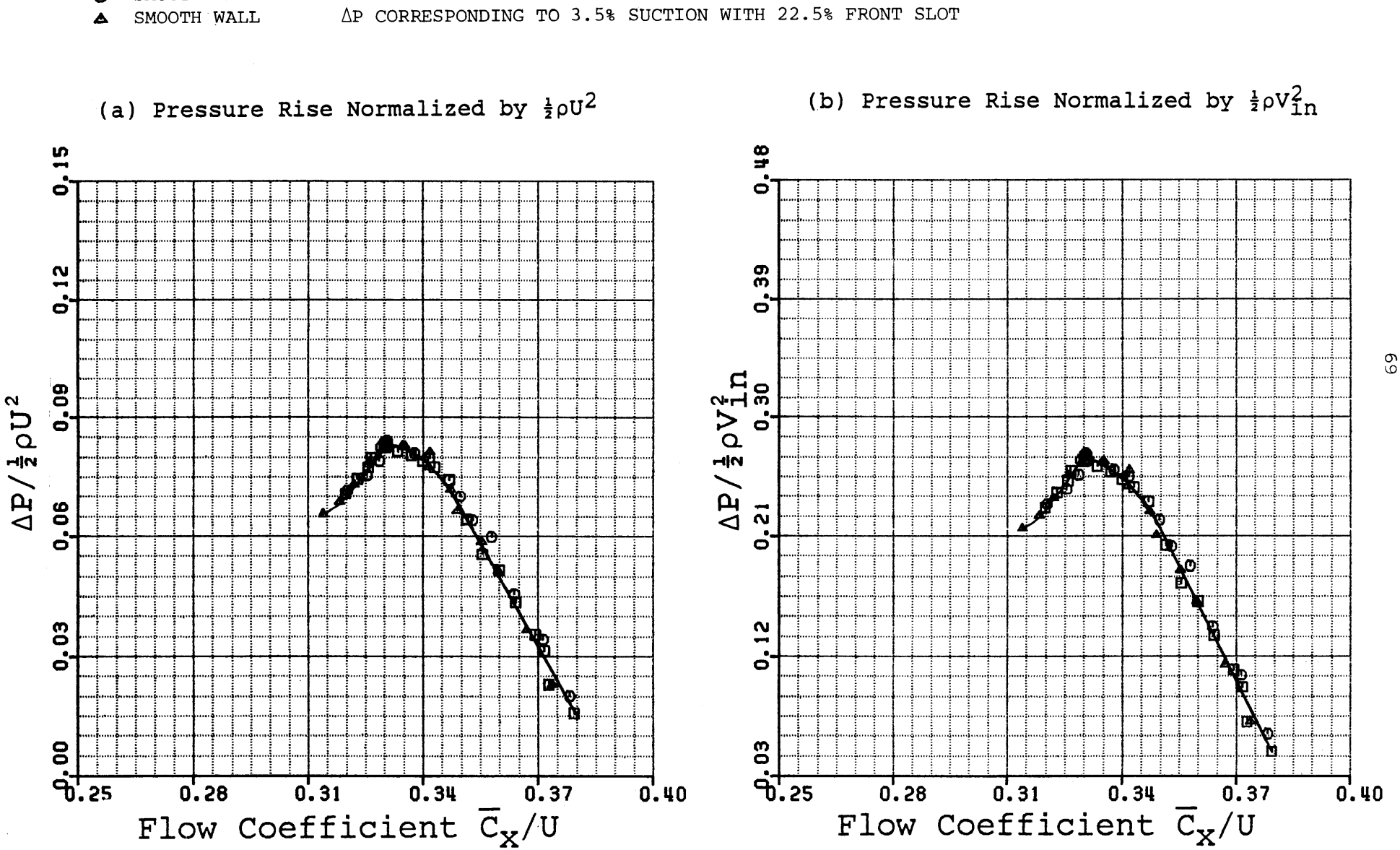

Fig. 26: Smooth wall speedlines: with positive plenum pressure, negative plenum pressure, and without application of pressure

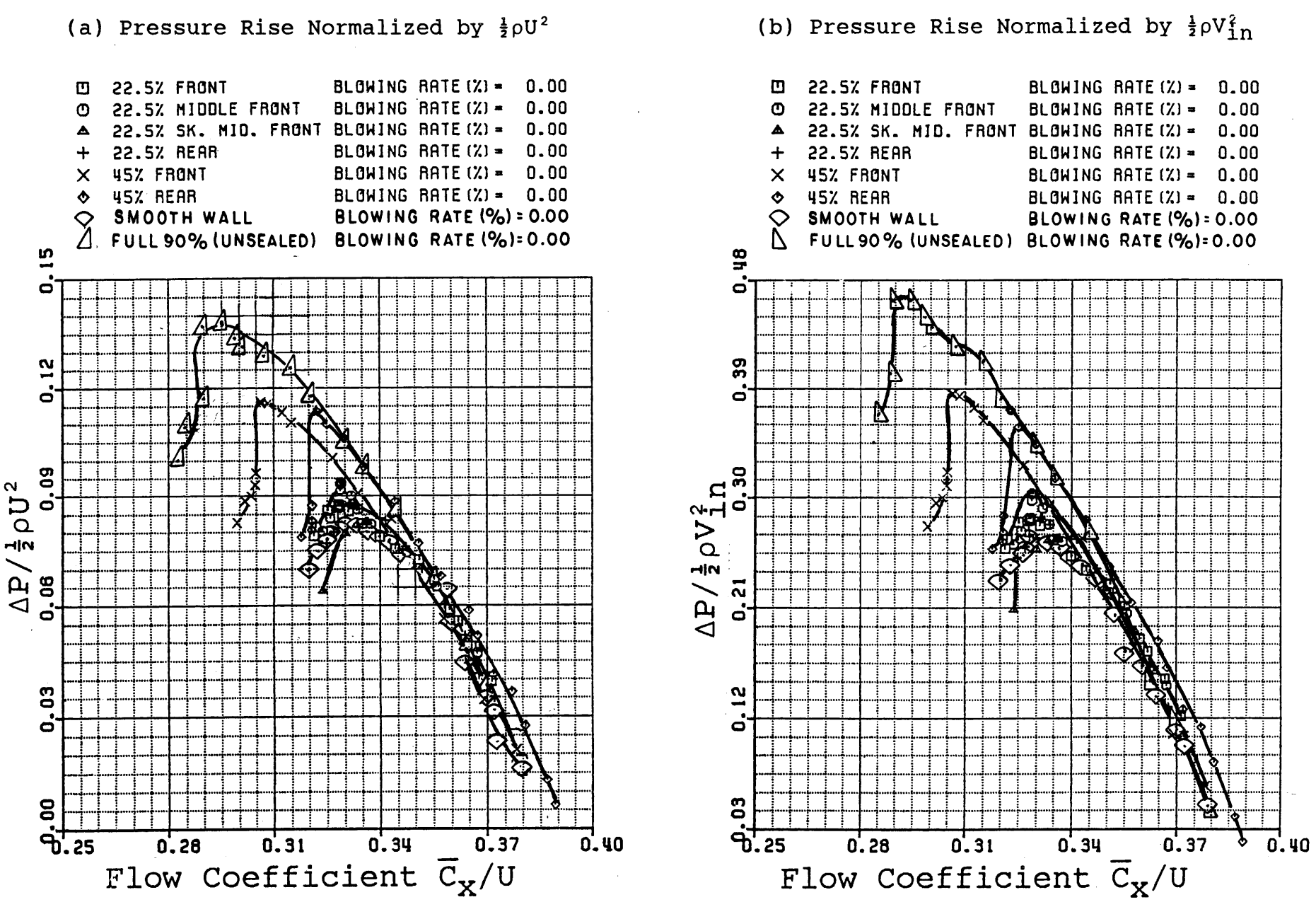

Fig. 27: Stator static pressure rise with no injection or removal

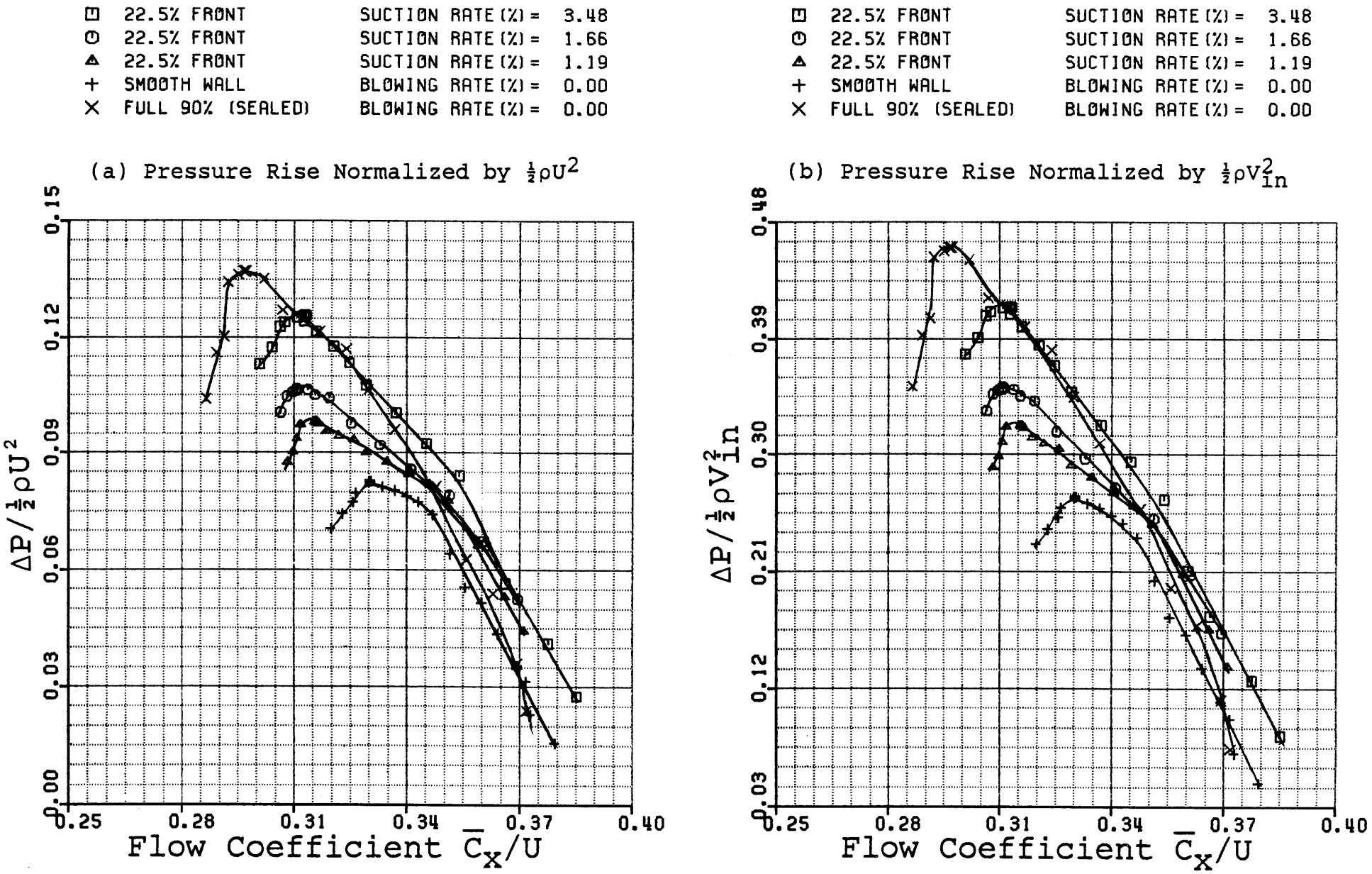

Fig. 28: Stator static pressure rise with removal: 22.5% front slots

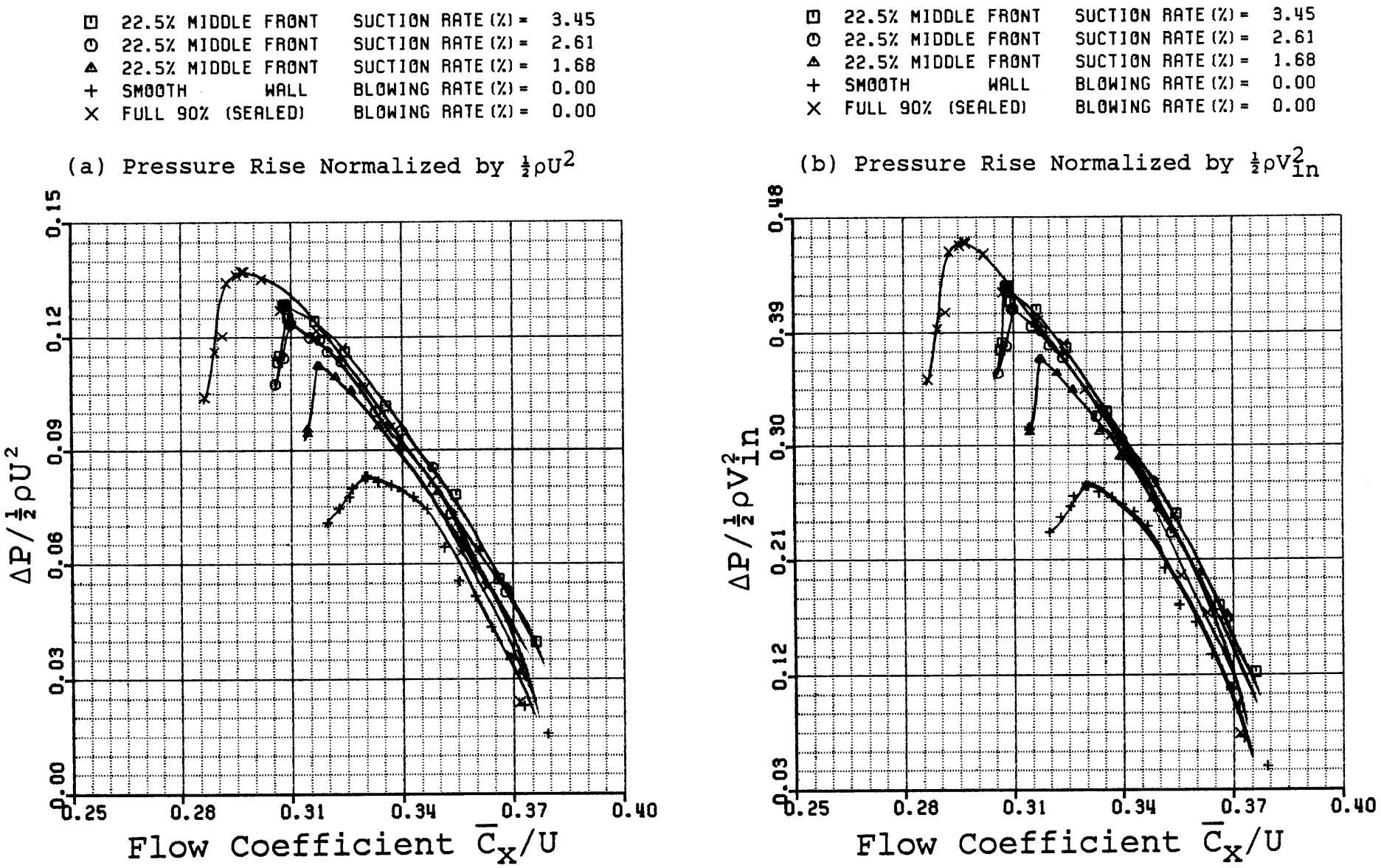

Fig. 29: Stator static pressure rise with removal: 22.5% middle front slots

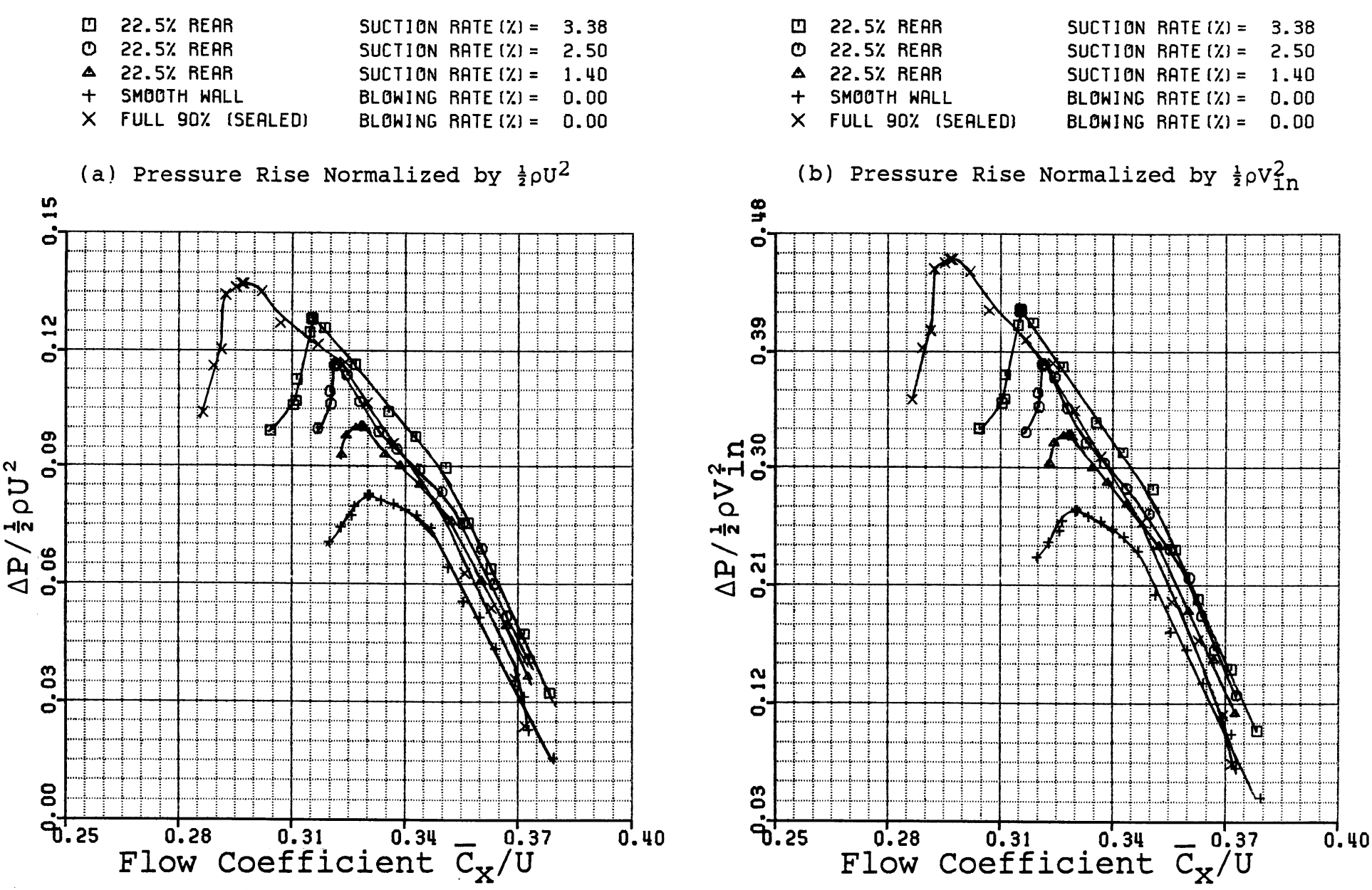

Fig. 30: Stator static pressure rise with removal: 22.5% rear slots

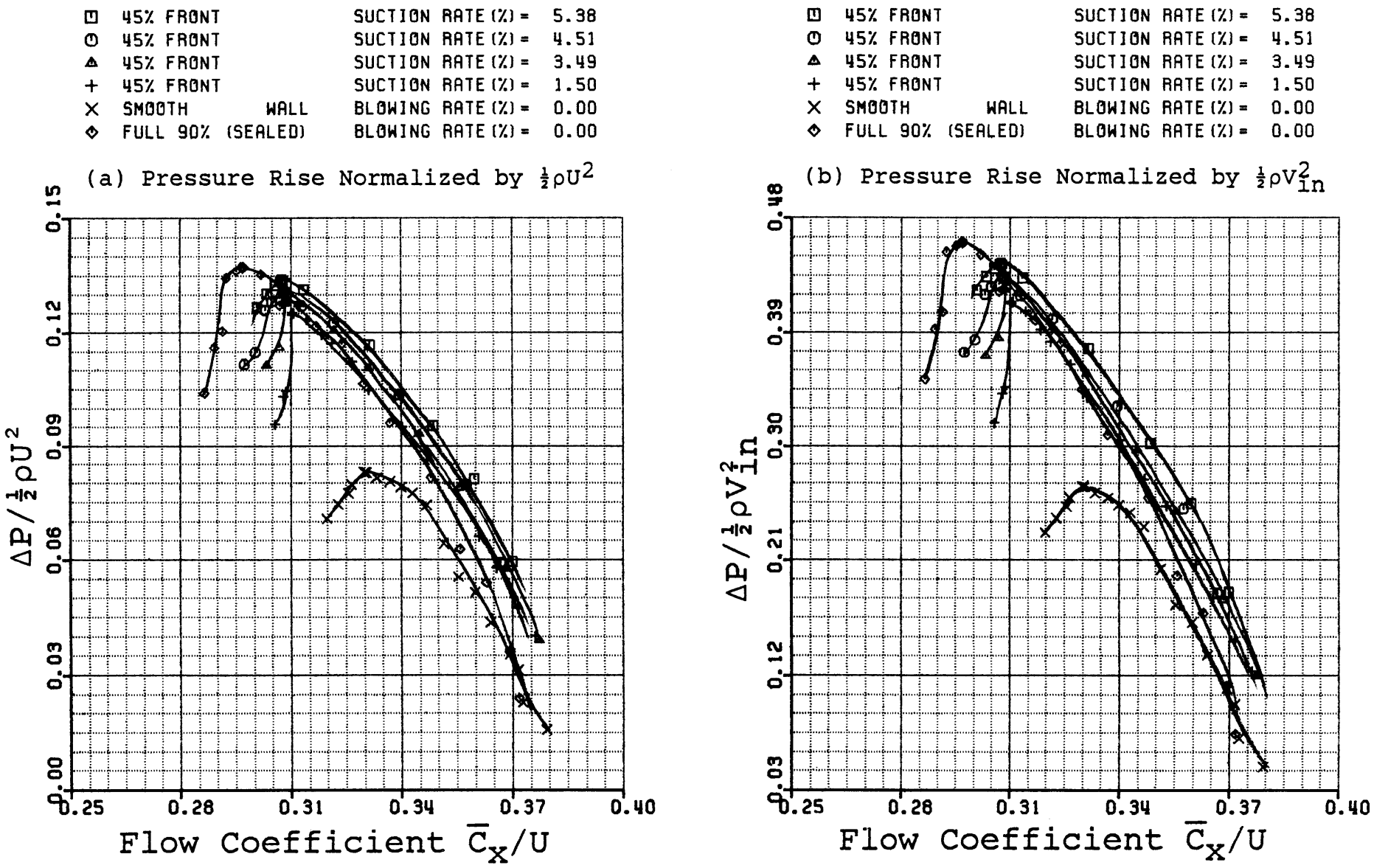

Fig. 31: Stator static pressure rise with removal; 45% front slots

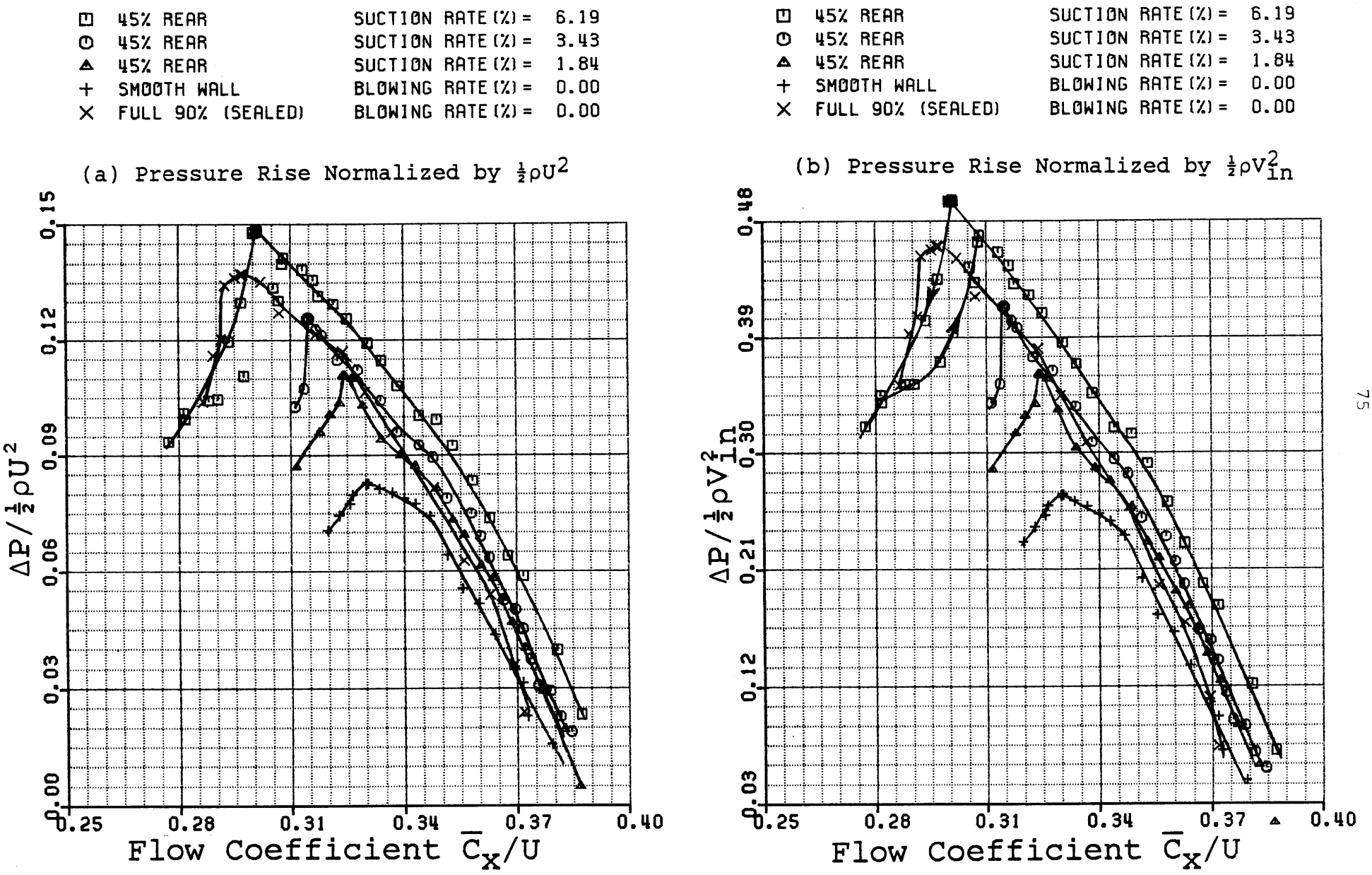

Fig. 32: Stator static pressure rise with removal: 45% rear slots

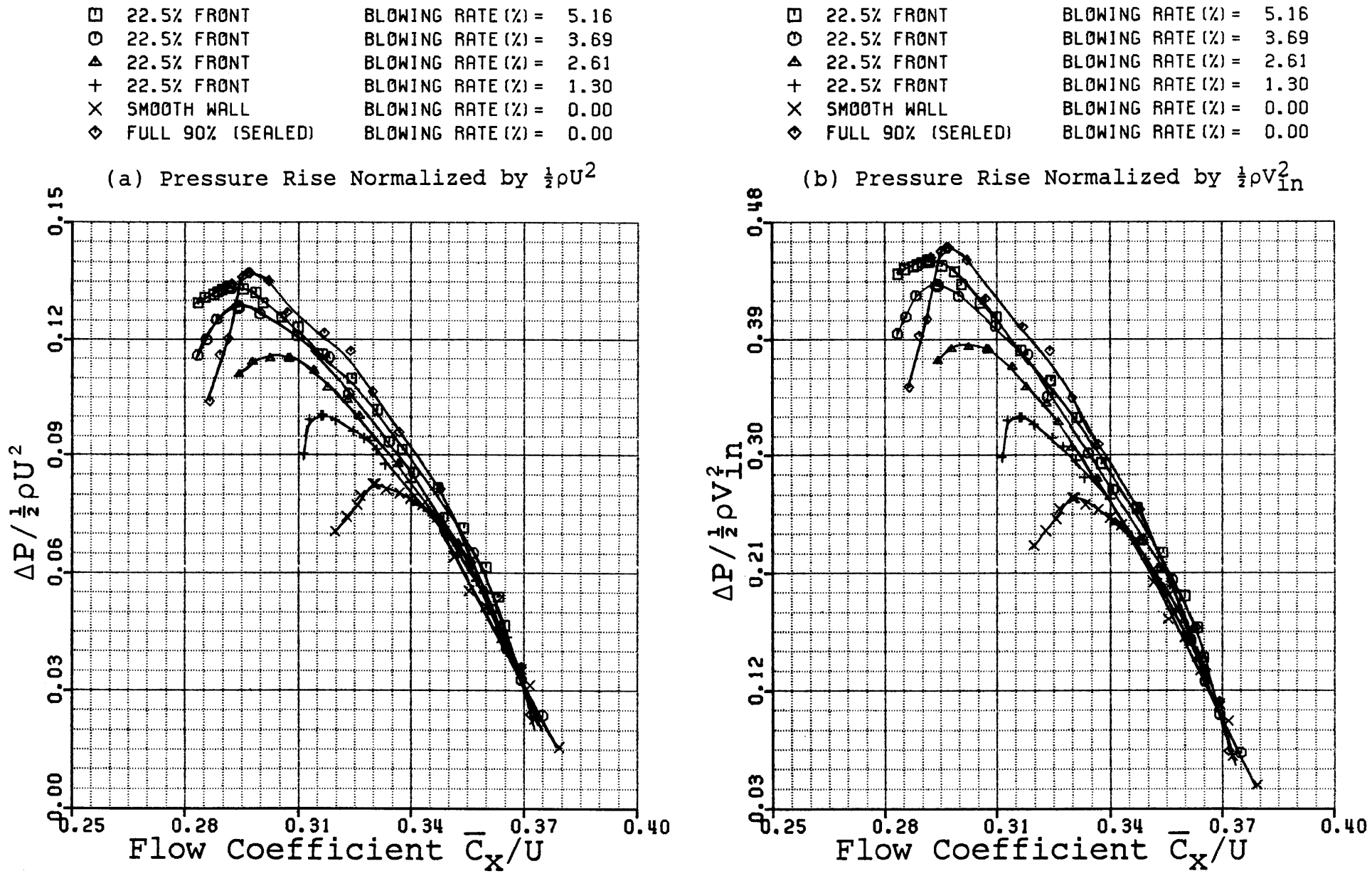

Fig. 33: Stator static pressure rise with injection: 22.5% front slots

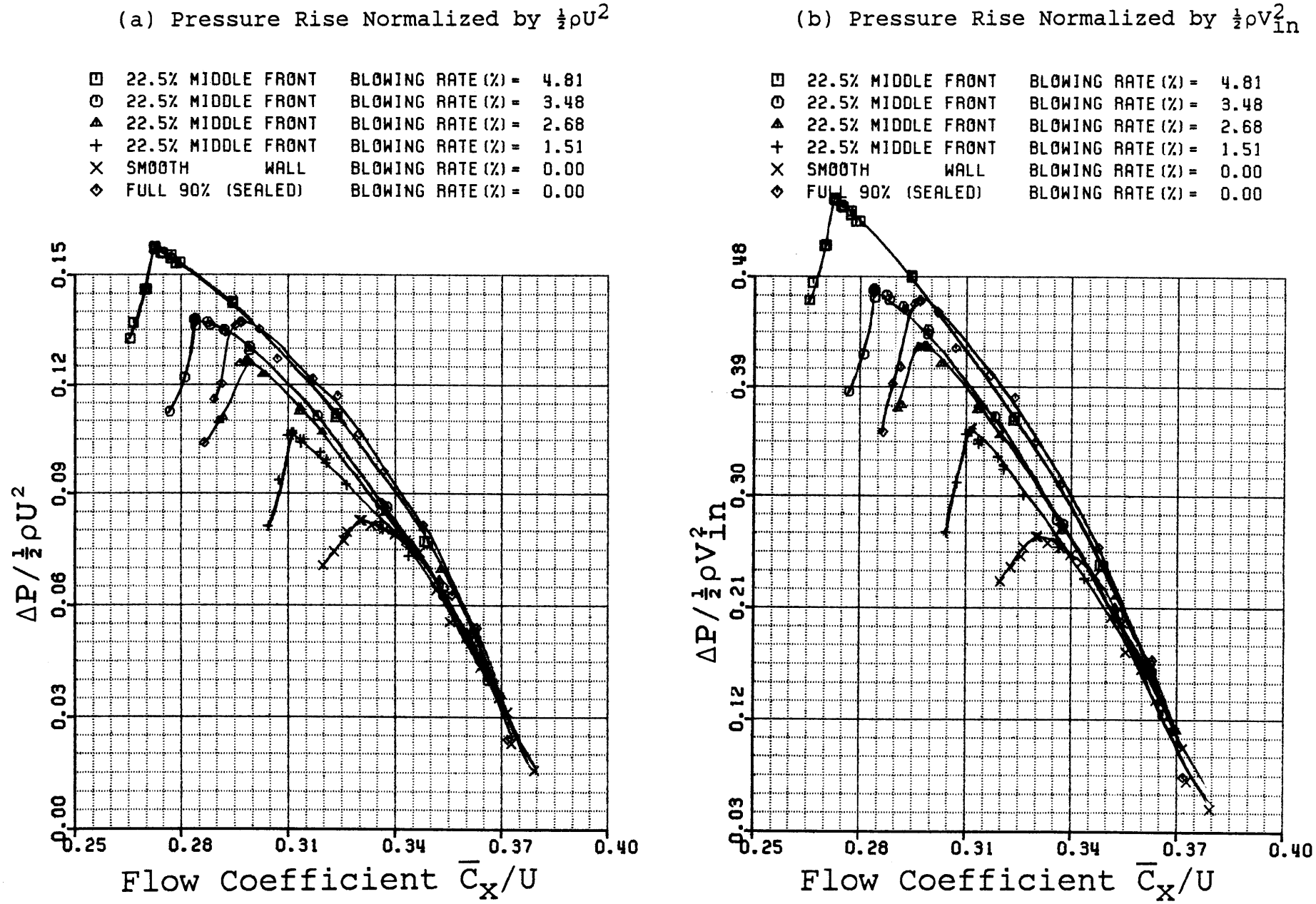

Fig. 34: Stator static pressure rise with injection: 22.5% middle front slots

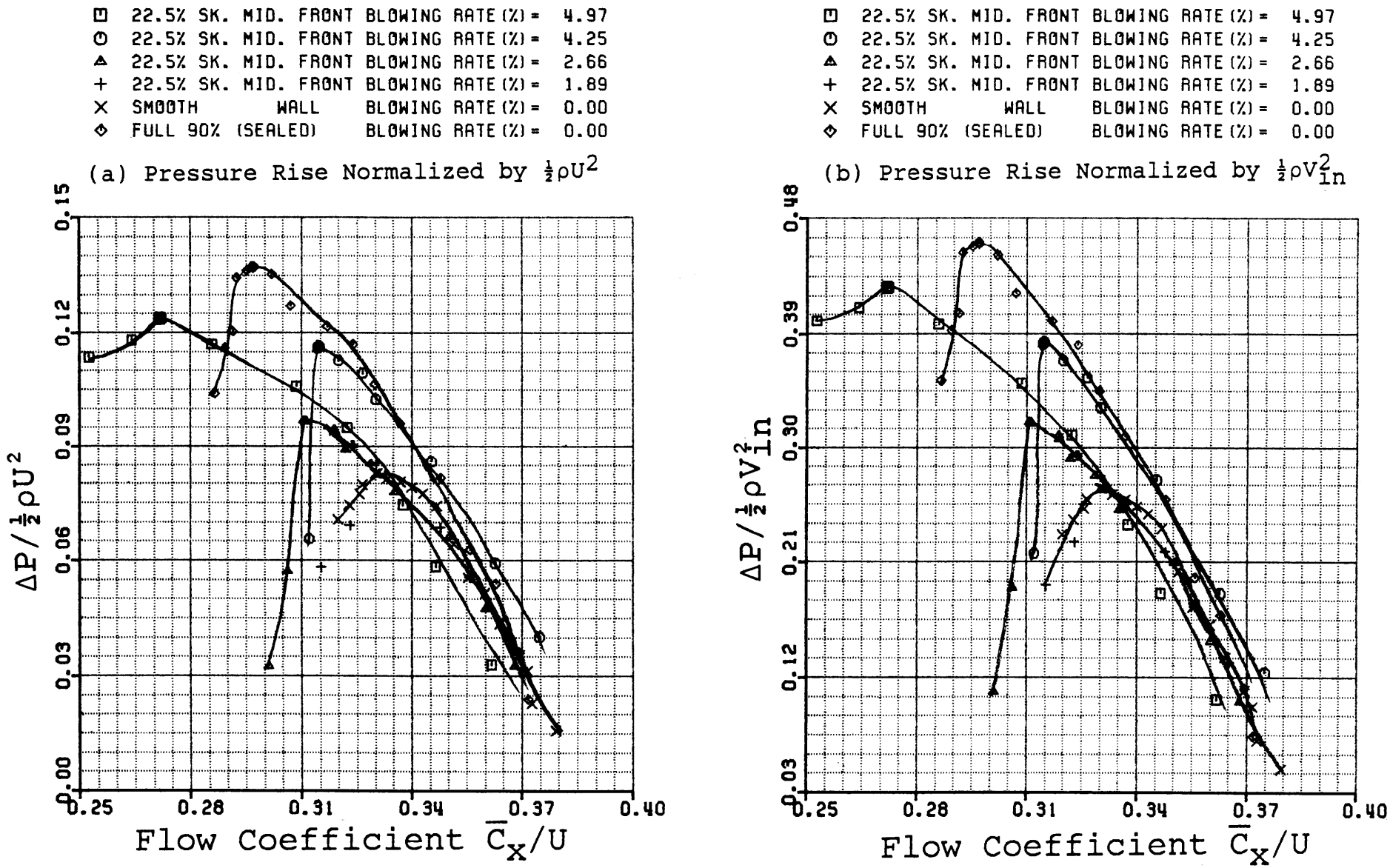

Fig. 35: Stator static pressure rise with injection: 22.5% skewed middle front slots

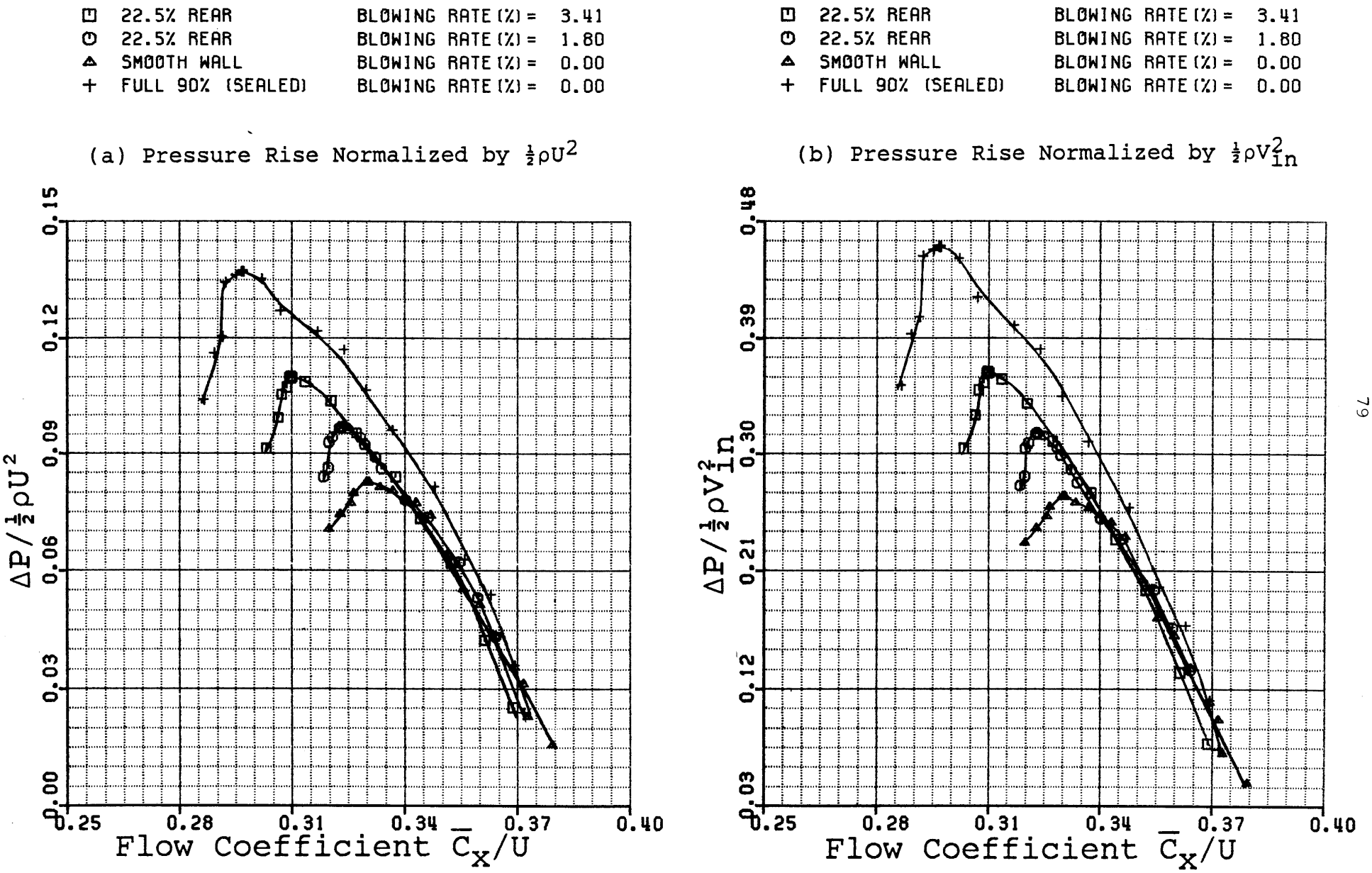

Fig. 36: Stator static pressure rise with injection: 22.5% rear slots

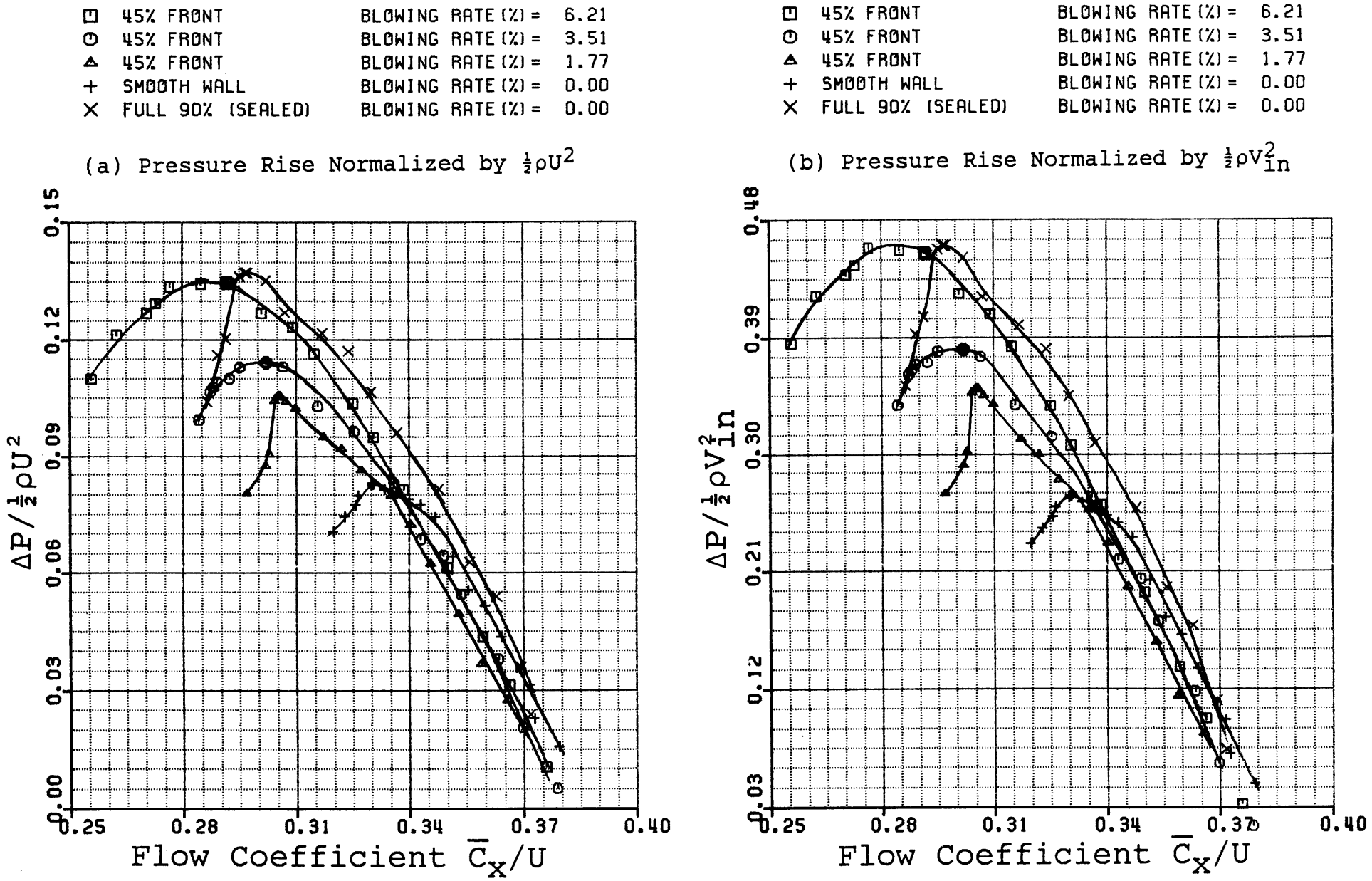

Fig. 37: Stator static pressure rise with injection: 45% front slots

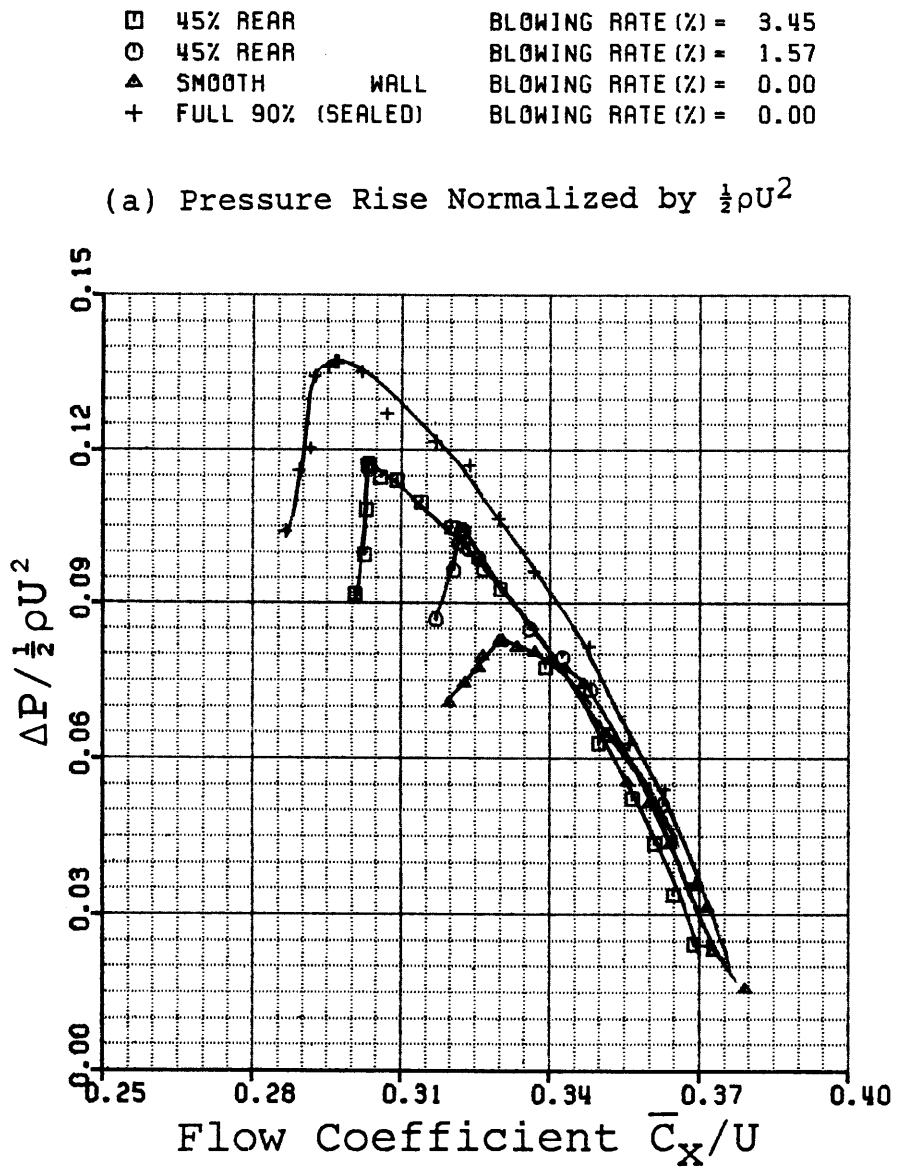

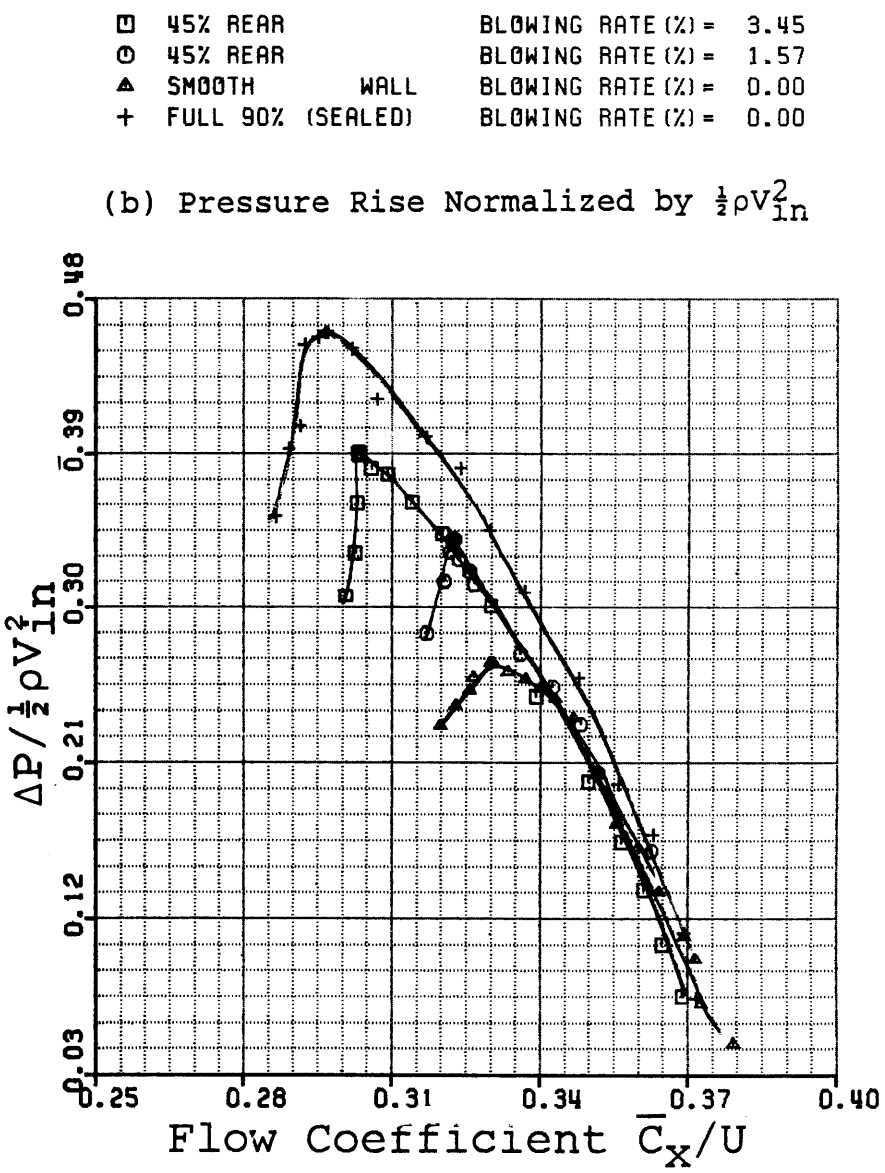

Fig. 38: Stator static pressure rise with injection: 45% rear slots

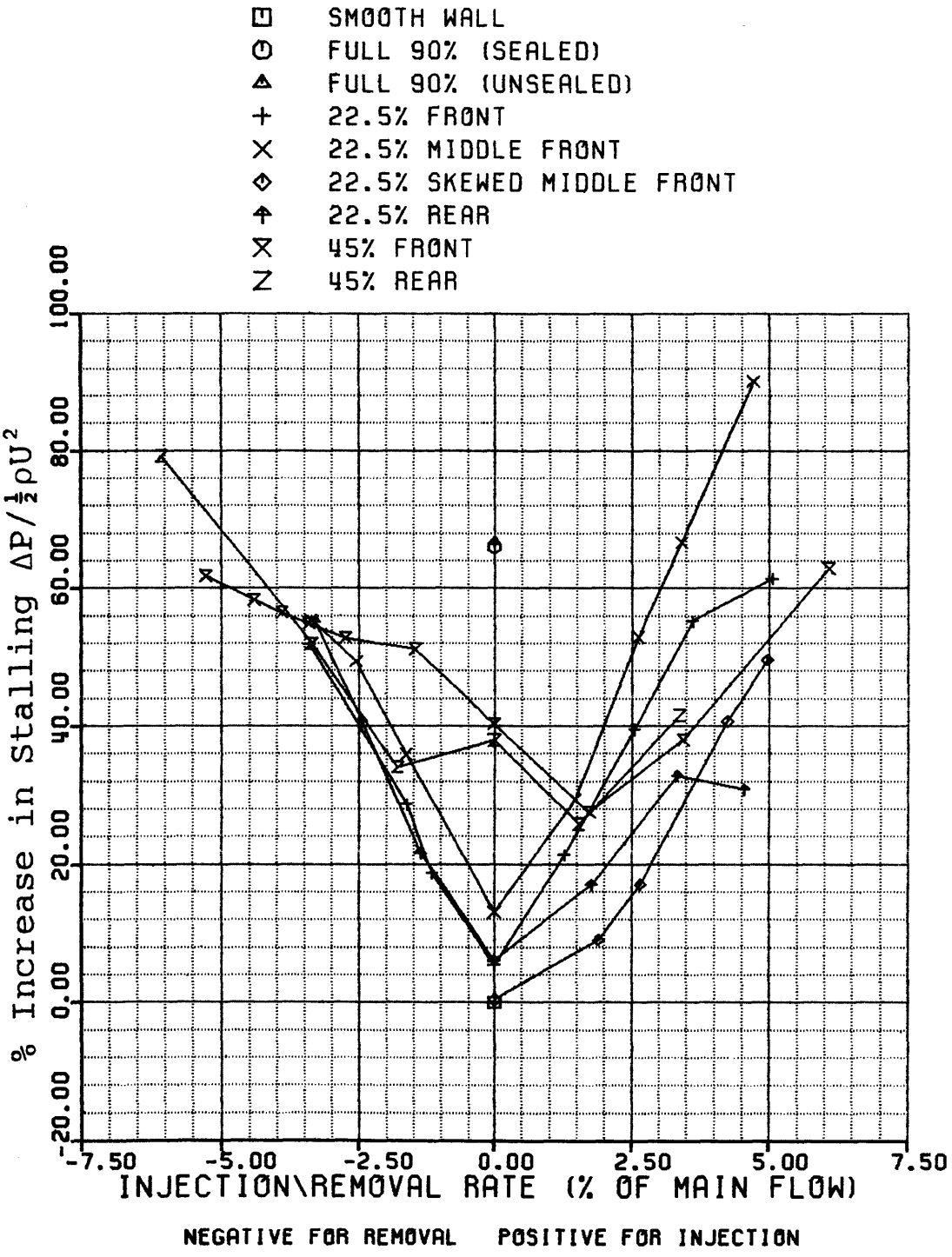

Fig. 39a: Percentage increase in performance of various slots over smooth wall

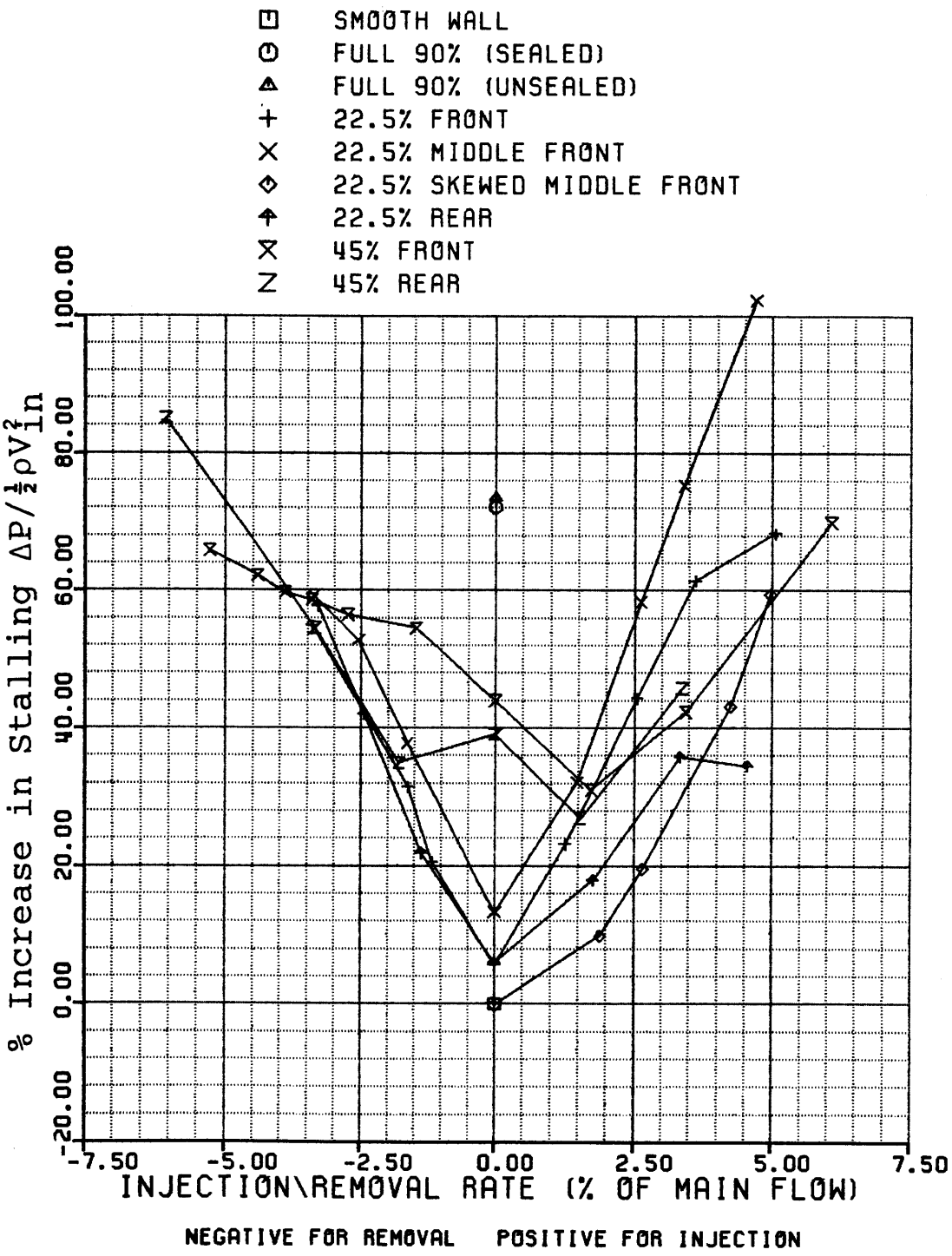

Fig. 39b: Percentage increase in performance of various slots over smooth wall

VELOCITY VECTORS

HUB TYPE	22.5% FRONT
SCALE (FT/S/IN)	150
TIME NO.	AVERAGE
BLOWING RATE (%)	2.82

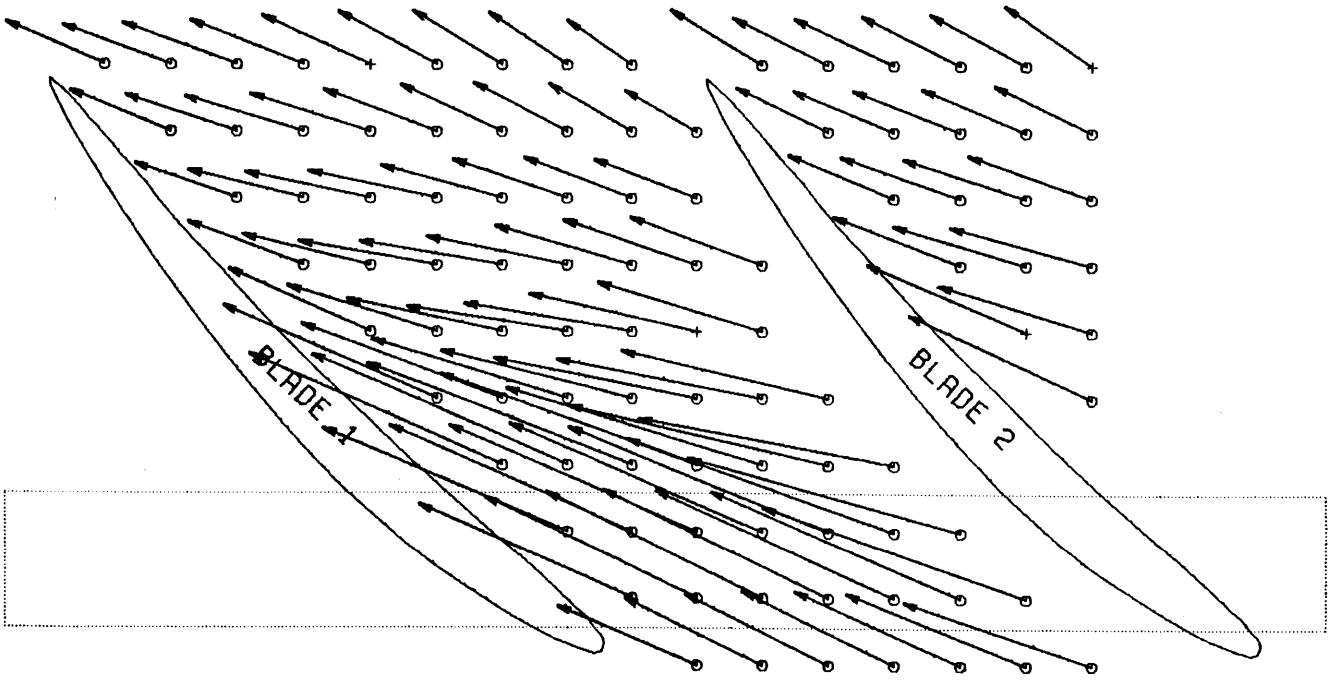

Fig. 40: Radial plane no. 1 at 2% span

VELOCITY VECTORS

HUB TYPE	22.5% FRONT
SCALE (FT/S/IN)	150
TIME NO.	AVERAGE
BLOWING RATE (%)	2.82

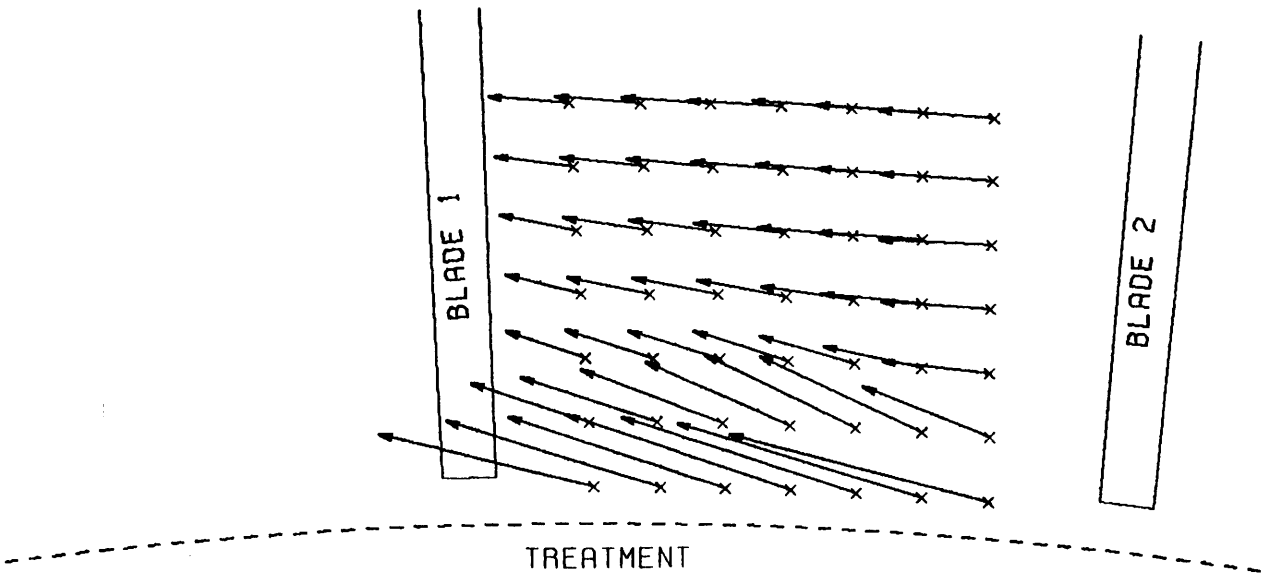

Fig. 41: Z plane no. 9 at 8% axial chord

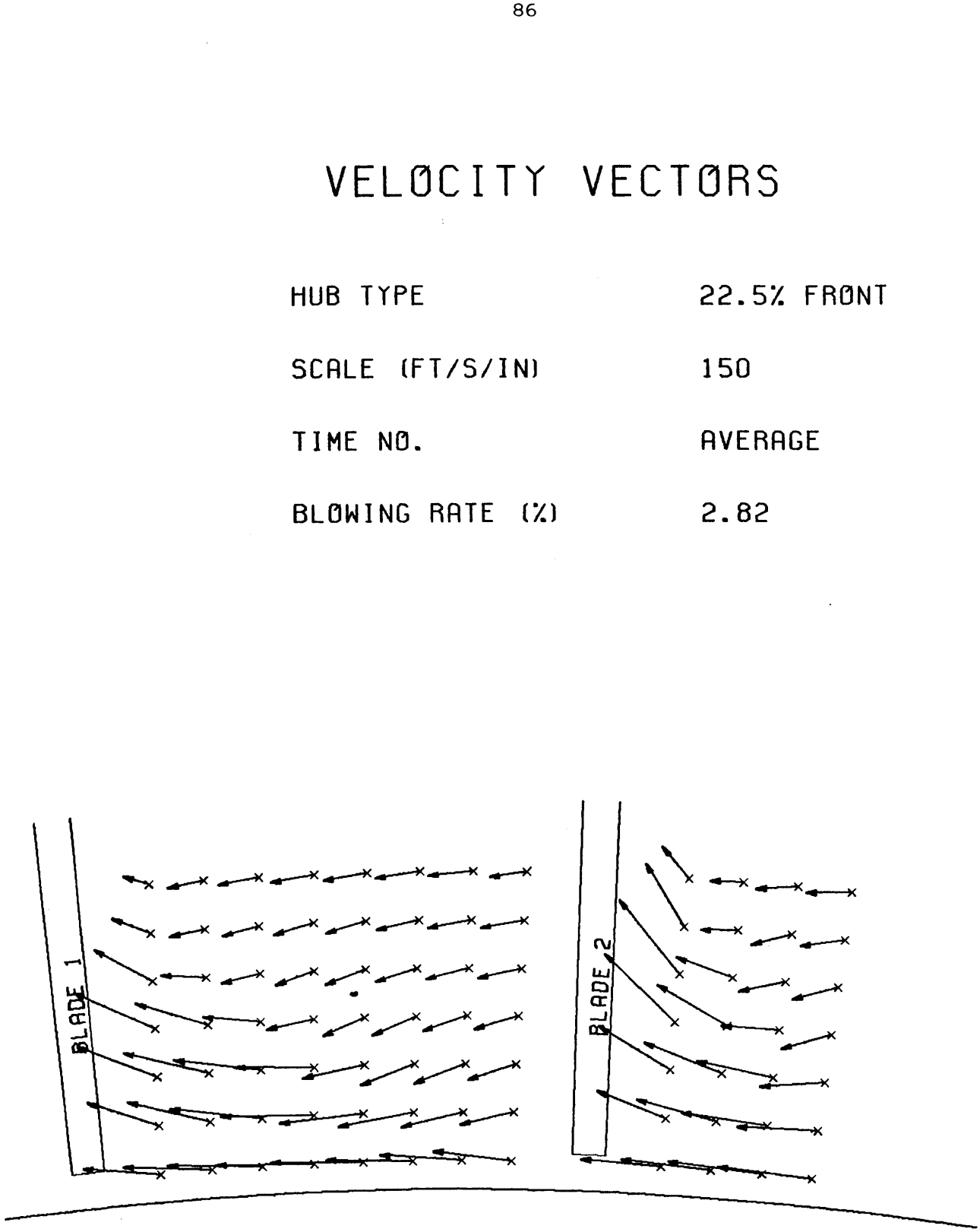

Fig. 42: Z plane no. 3 at 78% axial chord

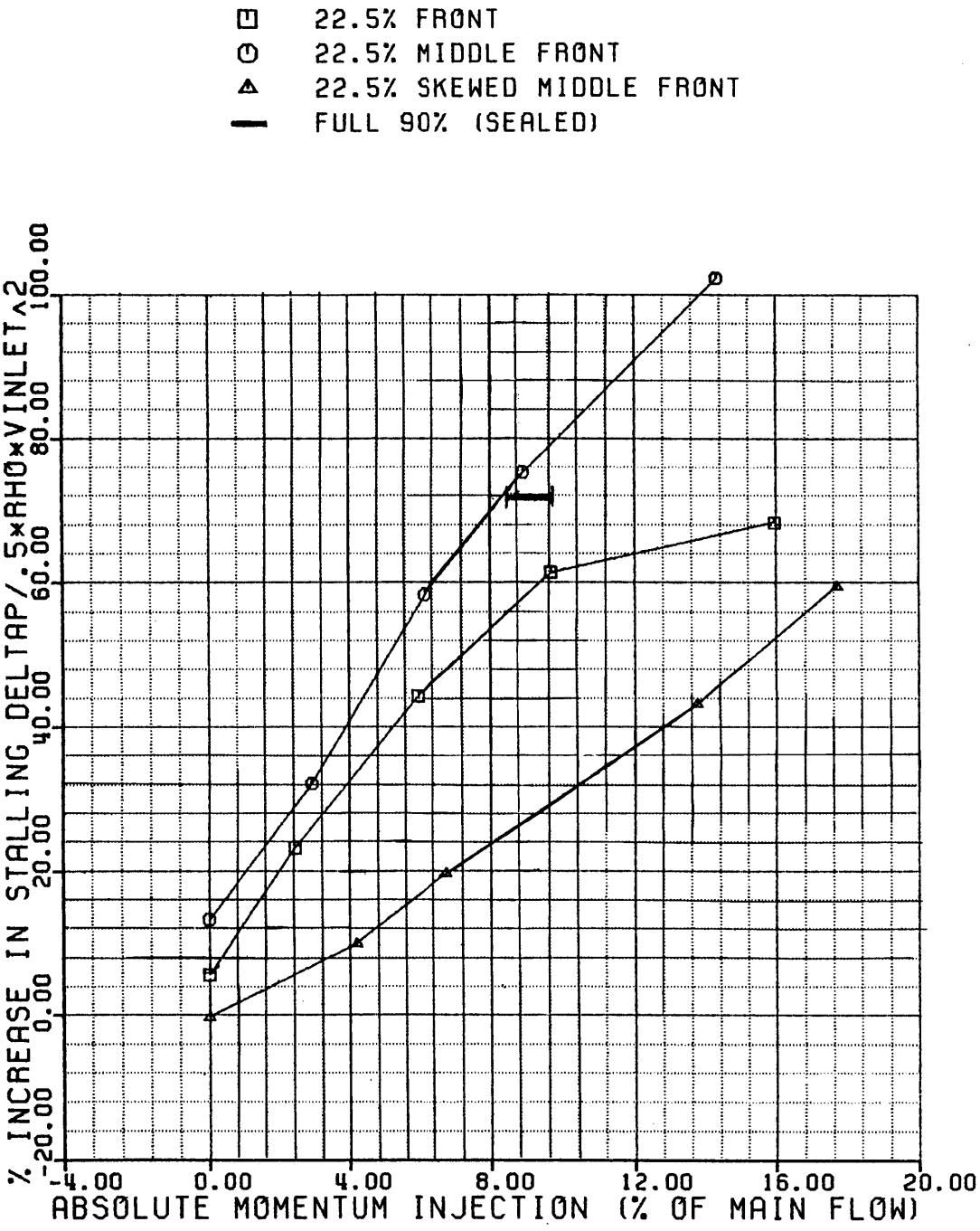

Fig. 43: Variation of performance with absolute momentum influx for the 22.5% slots

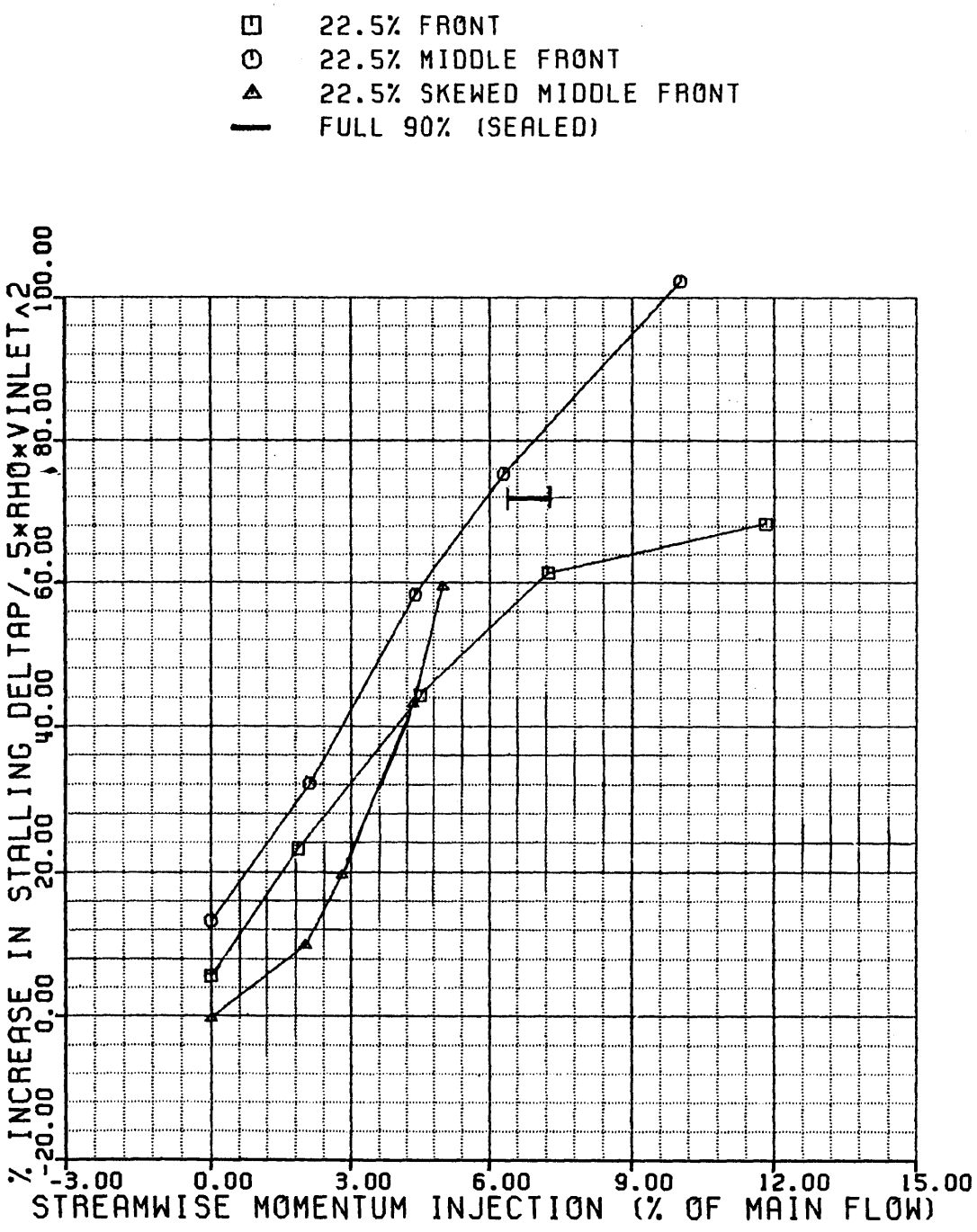

Fig. 44: Variation of performance with streamwise momentum influx for the 22.5% slots

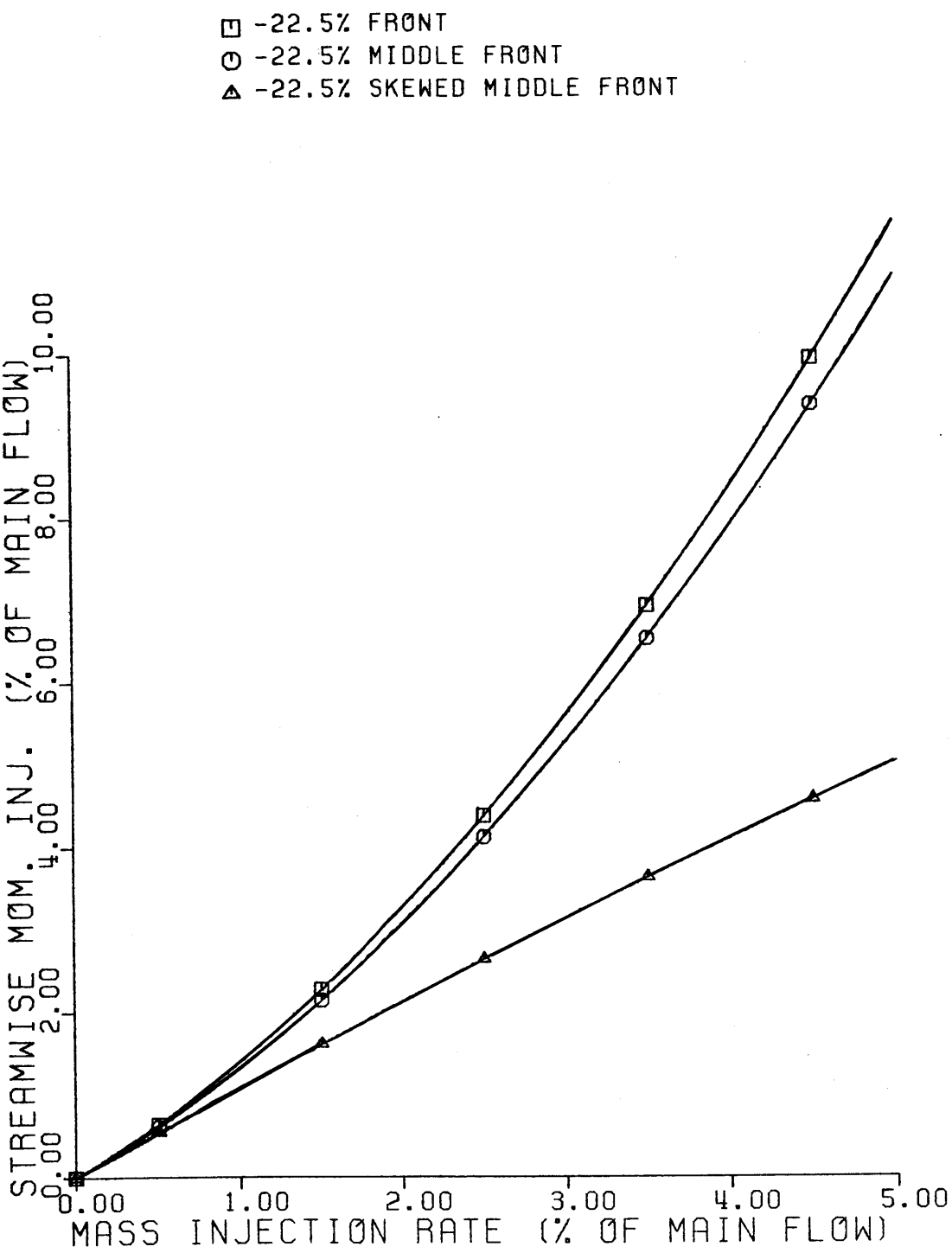

Fig. 45: Variation of streamwise momentum influx with mass injection rate for the 22.5% slots

Radial plane at 2% span

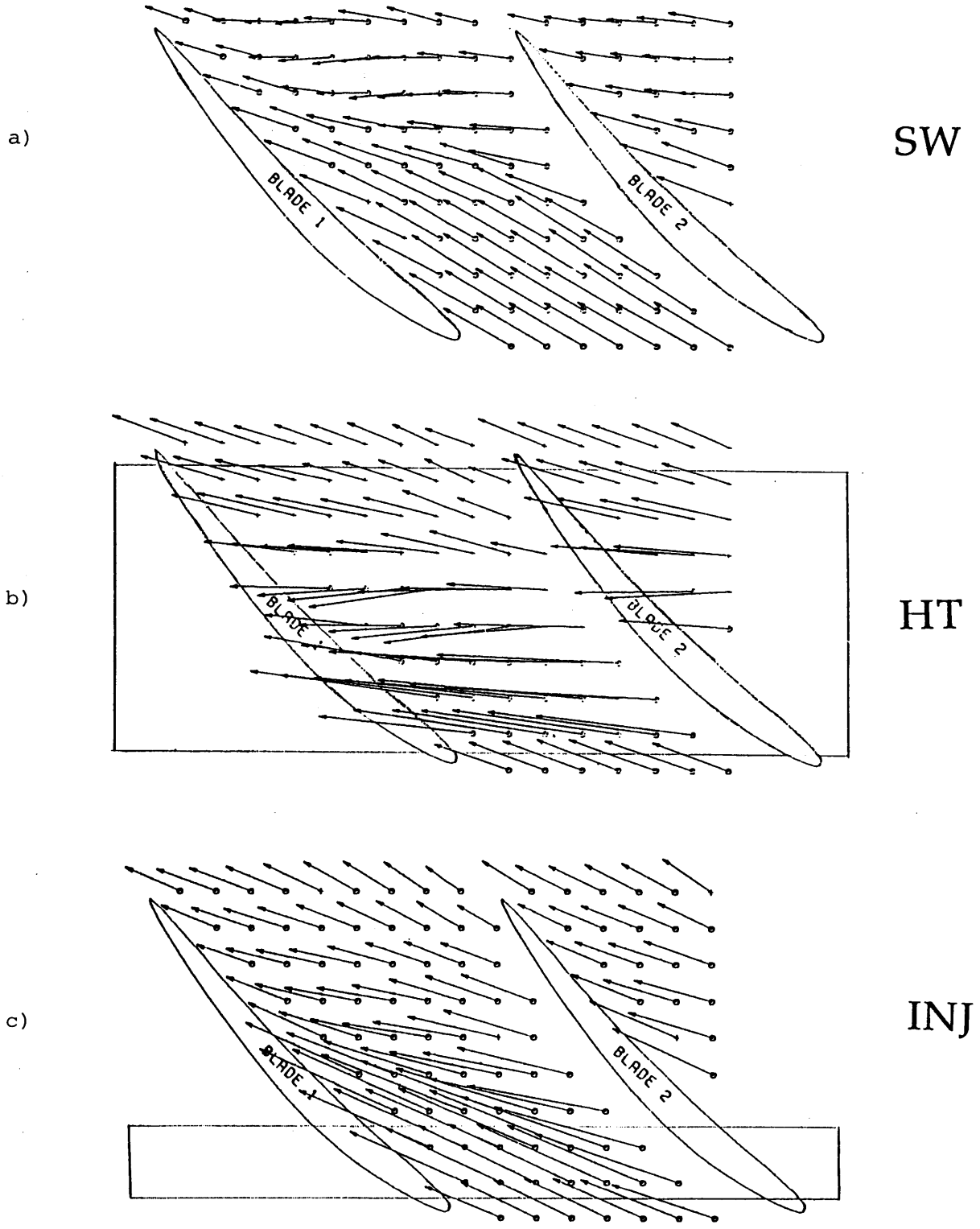

Fig. 46: Radial plane no. 1 at 2% span

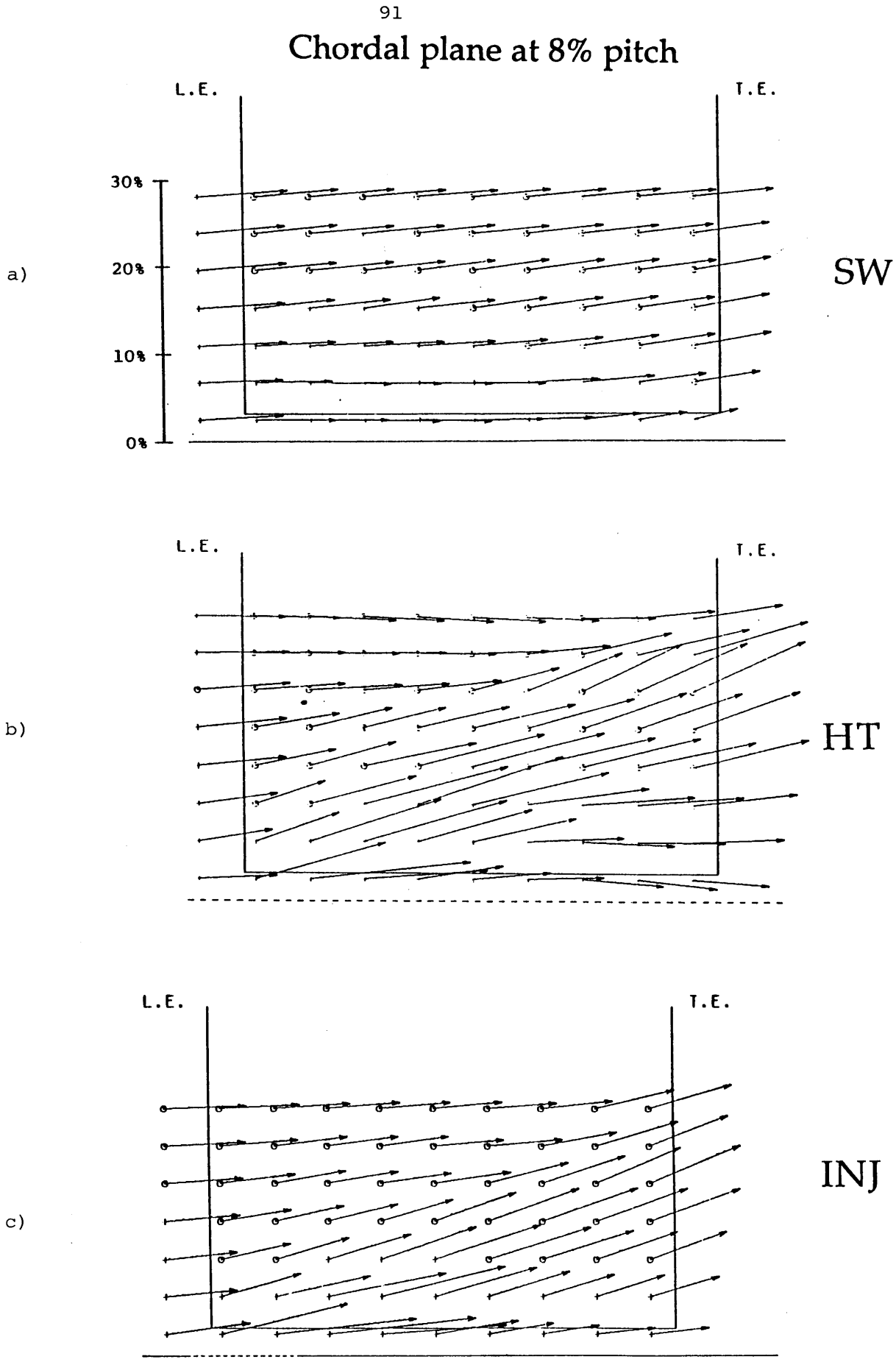

Fig. 47: Chordal plane no. 1 at 8% pitch

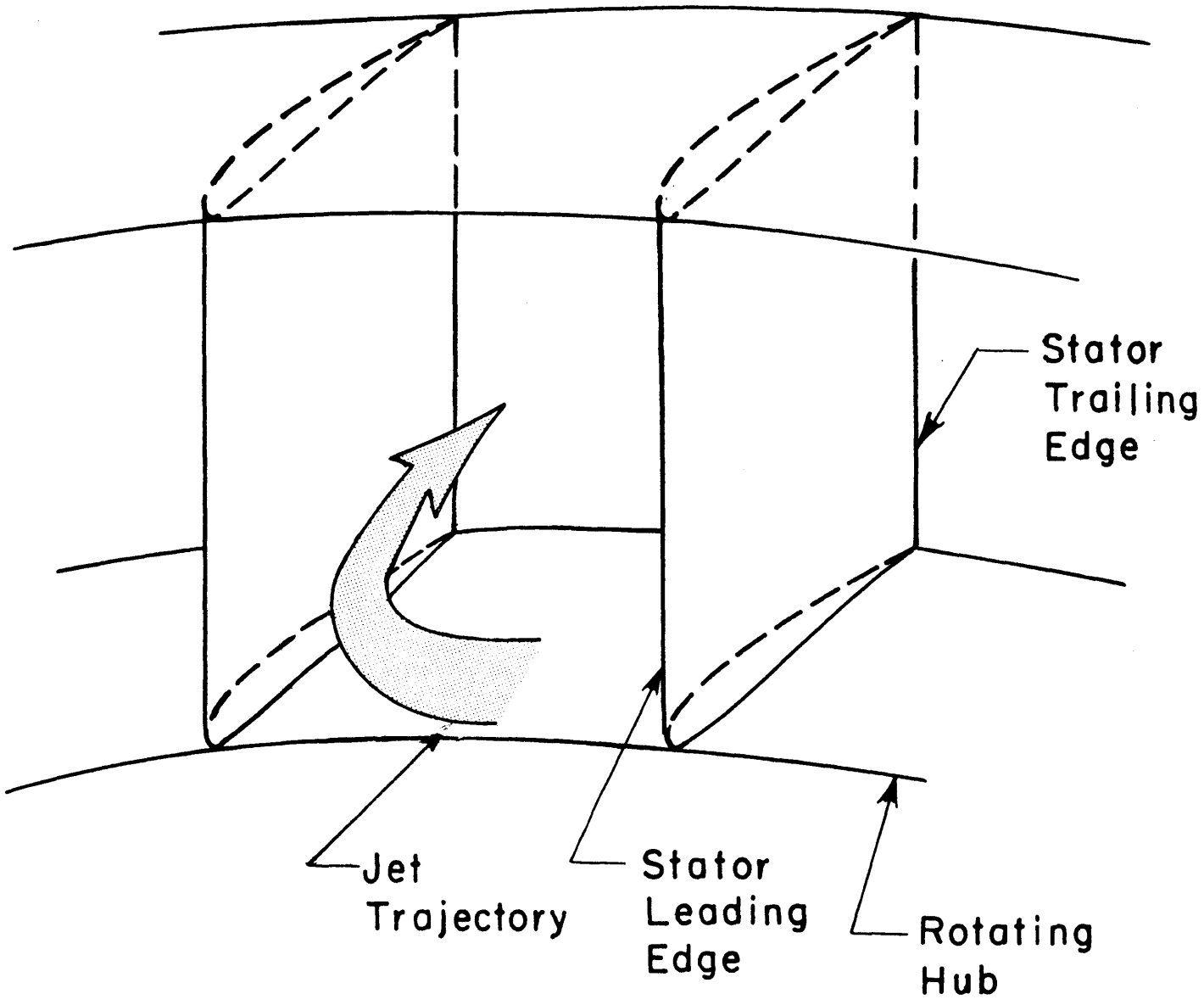

Fig. 48: Sketch of jet trajectory with hub treatment or with injection through 22.5% front slots

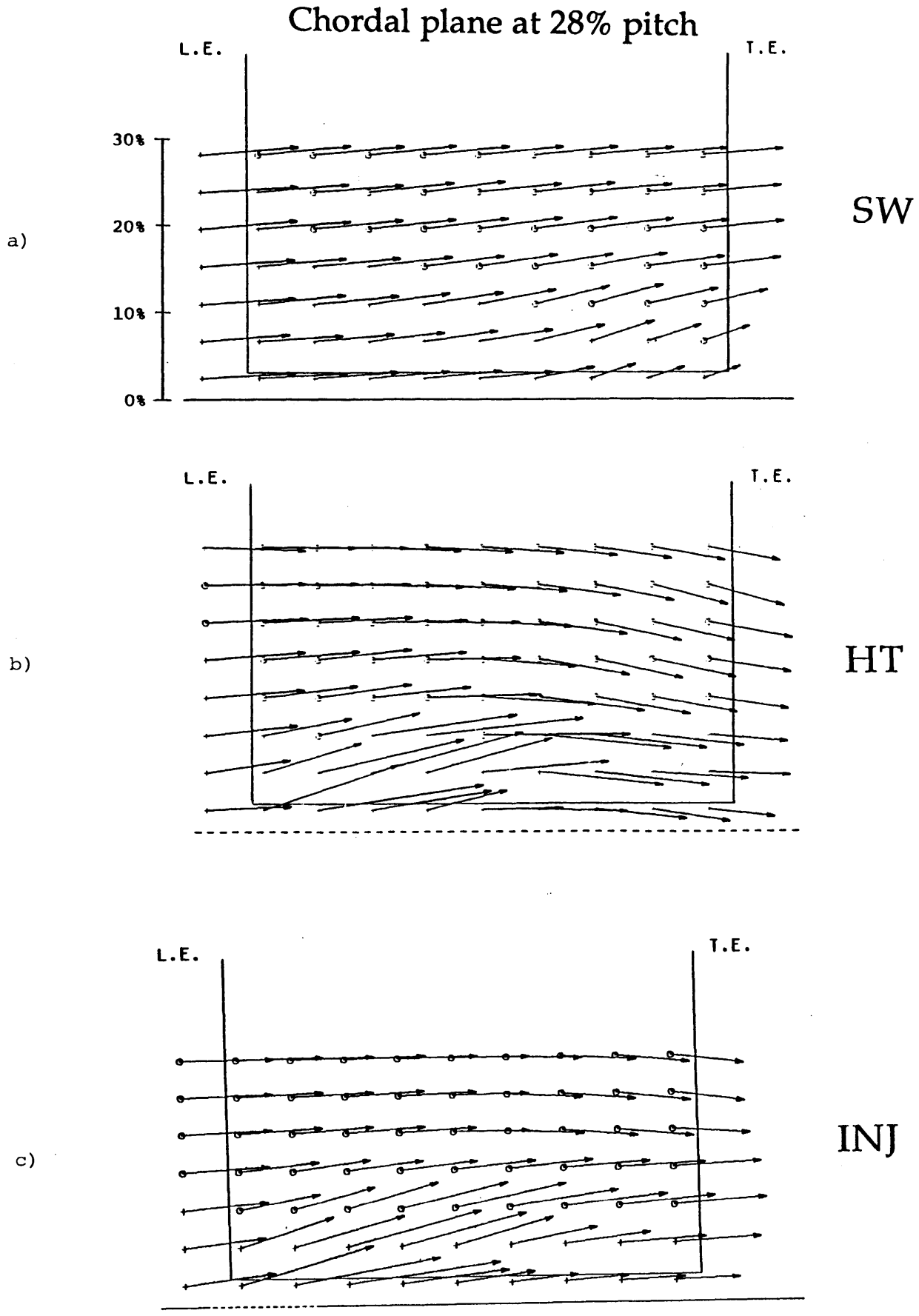

Fig. 49: Chordal plane no. 3 at 28% pitch

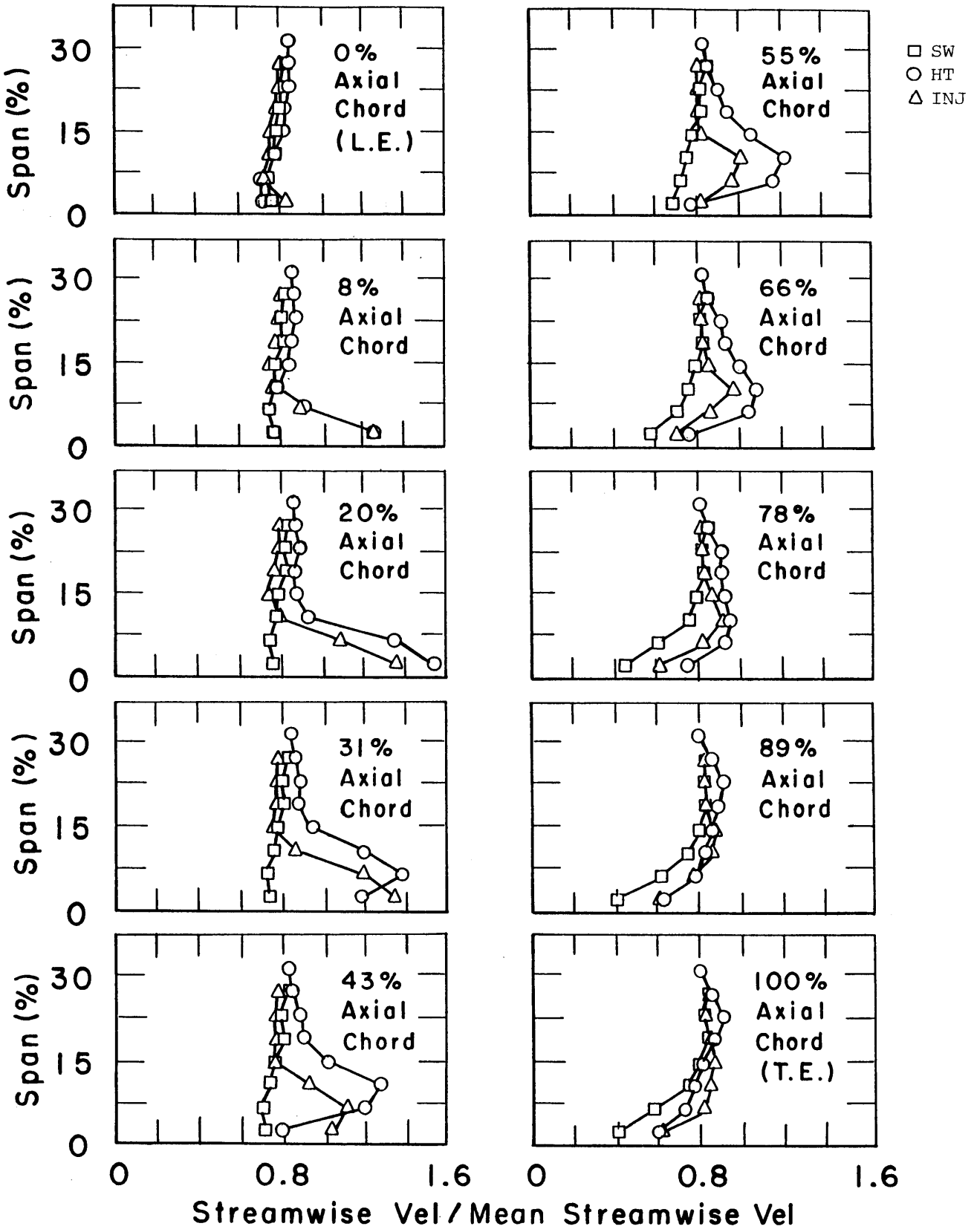

Fig. 50: Development of pitch-averaged streamwise velocity profile

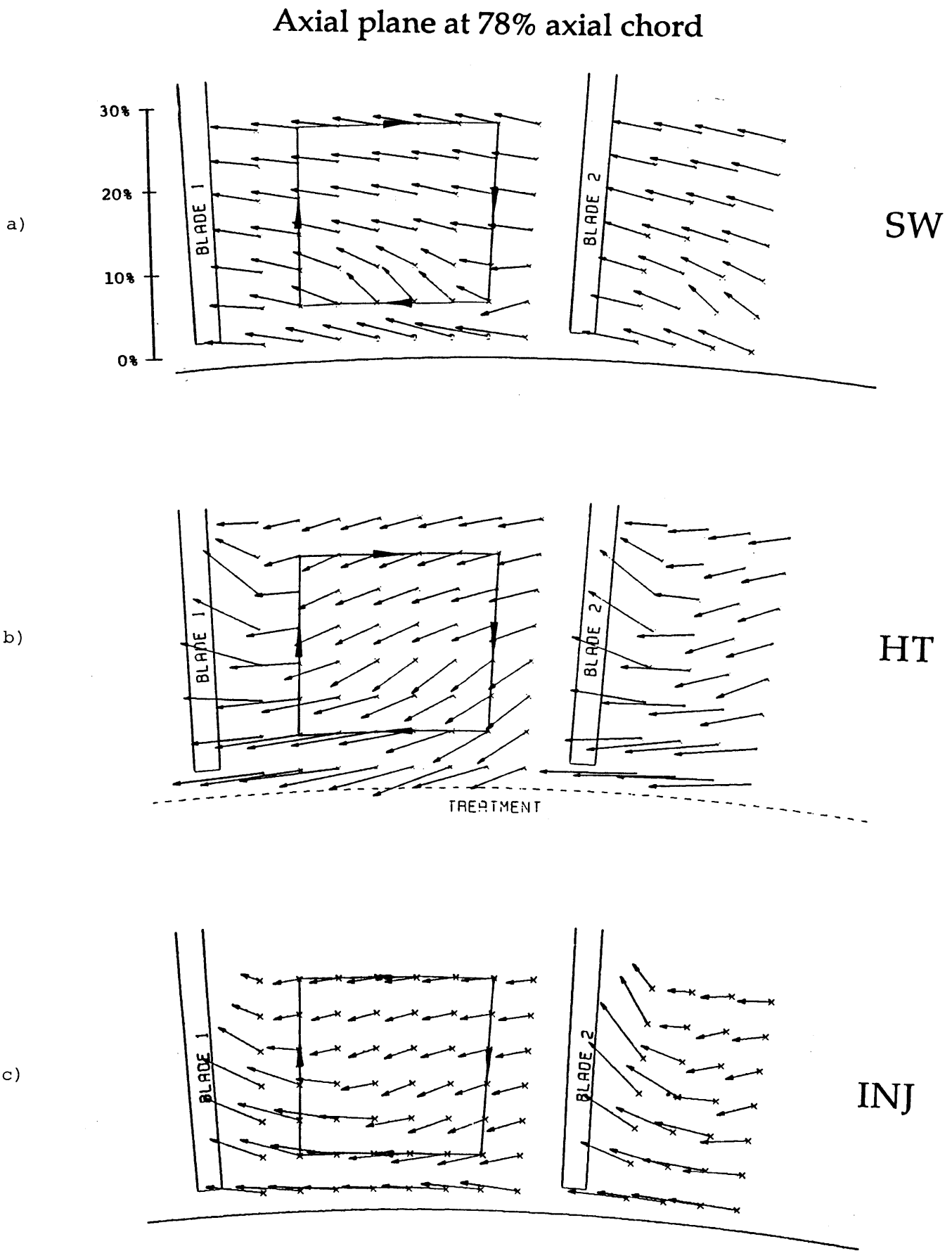

Fig. 51: Axial plane no. 3 at 78% axial chord

Chordal plane at 68% pitch

a)

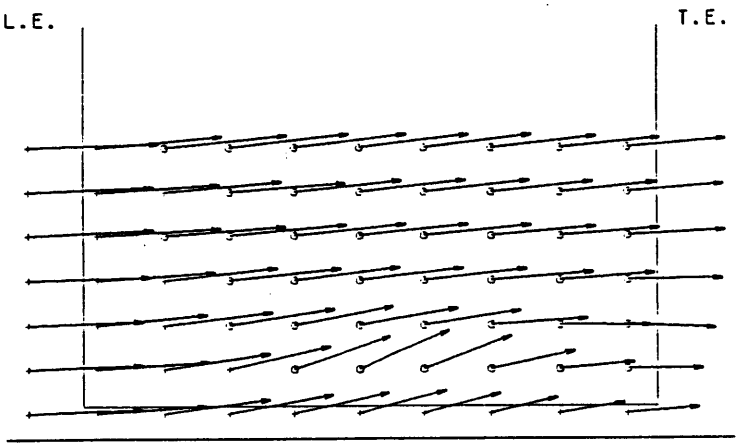

SW

b)

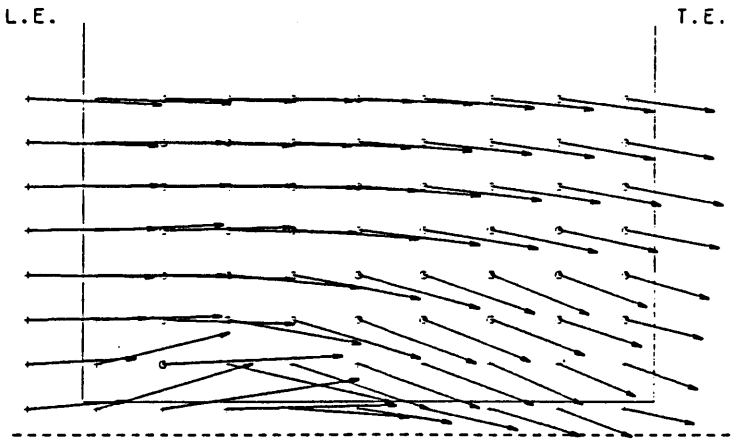

HT

c)

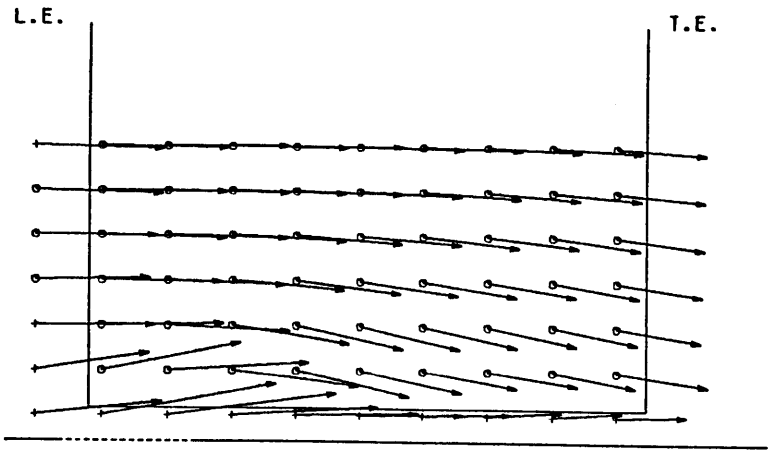

INJ

Fig. 52: Chordal plane no. 7 at 68% pitch

APPENDIX A
PRESSURE RISE DUE TO DIFFUSION EFFECTS OF SUCTION

Nomenclature

A	Area per stator passage perpendicular to compressor axis
C_x/U	Flow coefficient as defined in Chapters 1.0 - 6.0
DP	Difference between inlet and exit pressures
G	Angle between velocity and compressor axis
$\dot{m}$	Mass flow rate into a stator passage
P	Pressure
s	Endwall suction rate per stator passage as a fraction of $\dot{m}$
V	Velocity
ρ	Density

Subscripts

1	Stator inlet
2	Stator exit without suction
2'	Stator exit with suction

This part of the appendix contains a simple analysis to estimate the pressure rise due to diffusion effects of suction. The results are compared with the observed speedline shifts for the part of the characteristic away from stall.

Figure A.1 is a plan view of the stator passage. For the situation with no suction, the Bernoulli and continuity equations are

$$\frac{P_1}{\rho} + \frac{1}{2} V_1^2 = \frac{P_2}{\rho} + \frac{1}{2} V_2^2 \qquad (A.1)$$

$$\dot{m} = \rho A V_1 \cos G_1 = \rho A V_2 \cos G_2 \qquad (A.2)$$

In this, the compressor is operating away from stall and blockage is small so we neglect the differences in deviation and blockage between the smooth and untreated situation.

With suction,

$$\frac{P_1}{\rho} + \frac{1}{2} V_1^2 = \frac{P_{2'}}{\rho} + \frac{1}{2} V_{2'}^2 \qquad (A.3)$$

$$\dot{m} = \rho A V_1 \cos G_1 = \rho A V_{2'} \cos G_{2'} + \dot{sm} \tag{A.4}$$

Equations (A.2) and (A.4) give

$$\frac{V_{2'} \cos G_{2'}}{V_2 \cos G_2} = 1-s \tag{A.5}$$

Data from [8] shows that the exit flow angle changes very little so we assume $G_2 = G_{2'}$.

Now

$$DP_a \equiv P_2 - P_1 = \frac{1}{2} \rho \left(V_1^2 - V_2^2 \right) \quad , \text{ from (A.1)}$$

and

$$DP_b \equiv P_{2'} - P_1 = \frac{1}{2} \rho \left(V_1^2 - V_{2'}^2 \right) \quad , \text{ from (A.3)}$$

$DP_b - DP_a$ is the difference in pressure rise due to diffusion effects alone, at the same inlet conditions.

$$DP_b - DP_a = \frac{1}{2} \rho \left(V_2^2 - V_{2'}^2 \right)$$

$$= \frac{1}{2} \rho V_2^2 \left(1 - (1-s)^2 \right) \quad , \text{ from (A.5)}$$

So

$$\frac{DP_b - DP_a}{\frac{1}{2} \rho U^2} = \frac{V_2^2}{U^2} \left(1 - (1-s)^2 \right)$$

Also

$$V_2 = \frac{\bar{C}_x}{\cos G_2}$$

Hence

$$\frac{DP_b - DP_a}{\frac{1}{2}\rho U^2} = \left(\frac{\bar{C}_x}{U}\right)^2 \frac{\left(1 - (1-s)^2\right)}{\cos^2 G_2}$$

and

$$\frac{DP_b - DP_a}{\frac{1}{2}\rho V_1^2} = \frac{\cos^2 G_1}{\cos^2 G_2}\left(1 - (1-s)^2\right)$$

G_1 ($\bar{\beta}_{in}$ described in Section 4.1) varies with $\bar{C}_x/U$.

Table A.1 contains estimated and measured $(DP_b-DP_a)/0.5\rho U^2$ and $(DP_b-DP_a)/0.5\rho V_1^2$ for some typical $\bar{C}_x/U$ and s values. It can be seen that the agreement is quite reasonable.

The above analysis can be slightly modified to give the difference in pressure rise between any two cases with suction. Adding subscripts a and b to s for these two cases, results so obtained yield

$$\frac{DP_b - DP_a}{\frac{1}{2}\rho U^2} = \left(\frac{\bar{C}_x}{U}\right)^2 \frac{\left(1 - \left(\frac{1-s_b}{1-s_a}\right)^2\right)}{\cos^2 G_2}$$

and

$$\frac{DP_b - DP_a}{\frac{1}{2}\rho V_1^2} = \frac{\cos^2 G_1}{\cos^2 G_2}\left(1 - \left(\frac{1-s_b}{1-s_a}\right)^2\right)$$

A more detailed analysis using a linear velocity profile at inlet to model the actual skewness in V_1 results in an extra term in DP, equal to

$$-\frac{1}{2}\rho V_1^2 \frac{\alpha^2}{4}\left(\frac{\cos^2 G_2}{\cos^2 G_1} - 1\right)$$

where α, defined as

$$\frac{\text{(highest inlet velocity) - (lowest inlet velocity)}}{\text{mean inlet velocity}},$$

is a measure of the skewness in V_1. However, the numerical results from either are within 5% so only the simpler analysis has been presented here.

TABLE A.1
ESTIMATED AND MEASURED DIFFERENCES IN PRESSURE RISE DUE TO SUCTION ALONE

C_x/U	s (%)	Estimated $\frac{DPb-DPa}{0.5\rho U^2}$ ($*10^{-2}$)	Measured $\frac{DPb-DPa}{0.5\rho U^2}$ ($*10^{-2}$)	Estimated $\frac{DPb-DPa}{0.5\rho V_1^2}$ ($*10^{-2}$)	Measured $\frac{DPb-DPa}{0.5\rho V_1^2}$ ($*10^{-2}$)
0.37	5.7	2.4	2.6	7.6	9.0
0.37	3.1	1.3	1.2	4.2	4.8
0.37	2.3	1.0	1.5	3.1	4.2
0.35	6.1	2.3	2.5	7.6	8.9
0.35	3.3	1.3	1.7	4.2	6.0
0.35	2.4	0.9	1.5	3.1	4.5

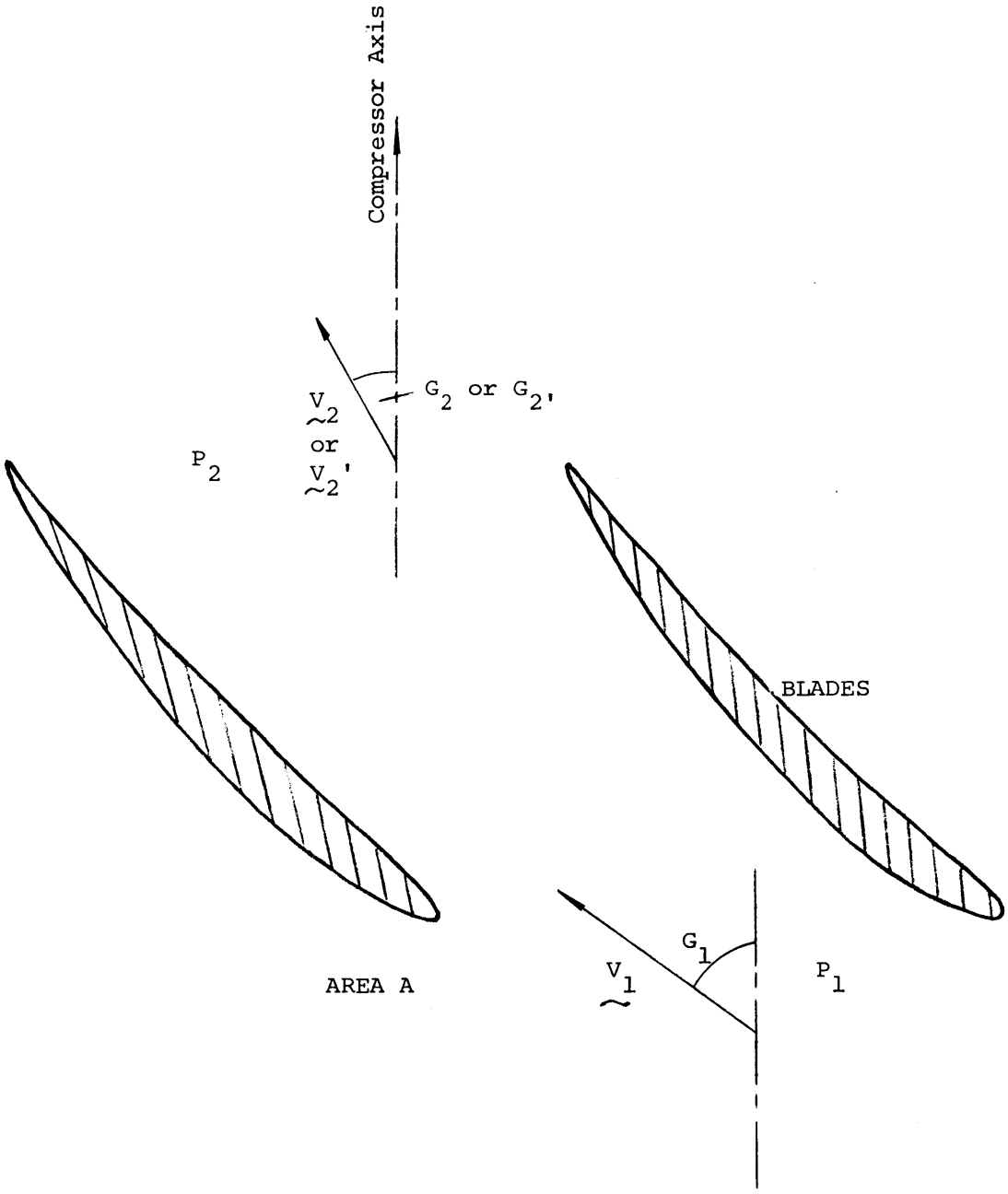

Figure A.1 Plan View of a Typical Stator Passage

APPENDIX B
PRESSURE RISE DUE TO MIXING OF JET WITH COMPRESSOR MAIN FLOW

Nomenclature

For diffuser model:

A	Area normal to velocity
b	Ratio of injection rate to mass flow rate at inlet
$\dot{m}_j$	Mass injection rate
P	Pressure
V	Velocity
V_{abs}	Absolute velocity of jet
β	Angle jet makes with x-axis in x-y plane
ρ	Density
ϕ	Angle jet makes with x-y plane

For compressor:

A_c	Area of compressor normal to its axis
C_x	Average axial velocity through compressor
U	Mean blade speed
α	Angle between stator velocity and compressor axis

Subscripts:

1	Inlet
2	Exit
a	After mixing, before expansion

This appendix contains an estimation of the pressure rise due to mixing of the jet with the compressor flow. The results will be compared with the observed speedline shifts of the characteristic away from stall.

The model is illustrated in Fig. B.1. A simple diffuser is used to model the stator row and the jet is supposed to have mixed out with the main flow upstream of the diverging section. Thus, mixing takes place between stations 1 and a, with diffusion between a and 2.

Continuity from 1 to a to 2

$$\rho A_1 V_1 + \dot{m}_j = \rho A_1 V_a = \rho A_2 V_2 \tag{B.1}$$

X-momentum between 1 and a

$$(P_1-P_a)A_1 = \rho A_1(V_a^2-V_1^2) - \dot{m}_j V_{abs}\cos\phi\ \cos\beta \tag{B.2}$$

Bernoulli between a and 2

$$P_a + \frac{1}{2}\rho V_a^2 = P_2 + \frac{1}{2}\rho V_2^2 \tag{B.3}$$

Solving these equations for P_2-P_1, we get grom Eqs. (B.2) and (B.3)

$$P_2 - P_1 = \frac{\rho}{2}\left(2V_1^2 - V_a^2 - V_2^2\right) + \frac{\dot{m}_j V_{abs}\cos\phi\ \cos\beta}{A_1} \tag{B.4}$$

Equations (B.1) and (B.4) give

$$P_2 - P_1 = \rho\,\frac{V_1^2}{2}\left\{2 - (1+b)^2\left[1 + \left(\frac{A_1}{A_2}\right)^2\right]\right\} + \frac{\dot{m}_j V_{abs}\cos\phi\ \cos\beta}{A_1} \tag{B.5}$$

with $b = \dot{m}_j/(\rho A_1 V_1)$, after simplification.

For

$$V_1 = \left(\frac{C_x}{U}\right)U \;/\; \cos\alpha_1$$

$$A_1 = A_c\cos\alpha_1$$

$$\frac{A_1}{A_2} = \frac{\cos\alpha_1}{\cos\alpha_2}$$

At the following conditions

$$\frac{\overline{C}_x}{U} = 0.345$$

$b = 0.036$ (3.6% injection rate)

$U = 70.9$ m/s

$\alpha_1 = 52°$

$\alpha_2 = 38°$

$A_c = 0.125\ m^2$

$\dot{m}_j V_{abs} \cos\phi \cos\beta = 10\ N$ (from Fig. 45)

So

$V_1 = 39.7\ m/s$

$A_1 = 0.077\ m^2$

$\frac{A_1}{A_2} = 0.781$

Equation (B.5) then gives

$P_2 - P_1 = 408\ N/m^2$

$\frac{P_2 - P_1}{\frac{1}{2}\rho U^2} = 0.126$

at 3.6% injection rate, $\overline{C}_x/U = 0.345$.

Similarly, for the case with no injection,

$b = 0$

$\dot{m}_j = 0$

$P_2 - P_1 = 397\ N/m^2$

$\frac{P_2 - P_1}{\frac{1}{2}\rho U^2} = 0.122$

The increase in normalized pressure rise due to mixing of the jet with the main flow, at 3.6% injection rate, is then

$$\left(\frac{P_2-P_1}{\frac{1}{2}\rho U^2}\right)_{\substack{3.6\% \\ \text{injection}}} - \left(\frac{P_2-P_1}{\frac{1}{2}\rho U^2}\right)_{\substack{\text{no} \\ \text{injection}}} = 0.004$$

This agrees well with the measured value of 0.004 from Fig. 33a. The calculated value is considerably less than that for suction; this is also seen in the speedlines.

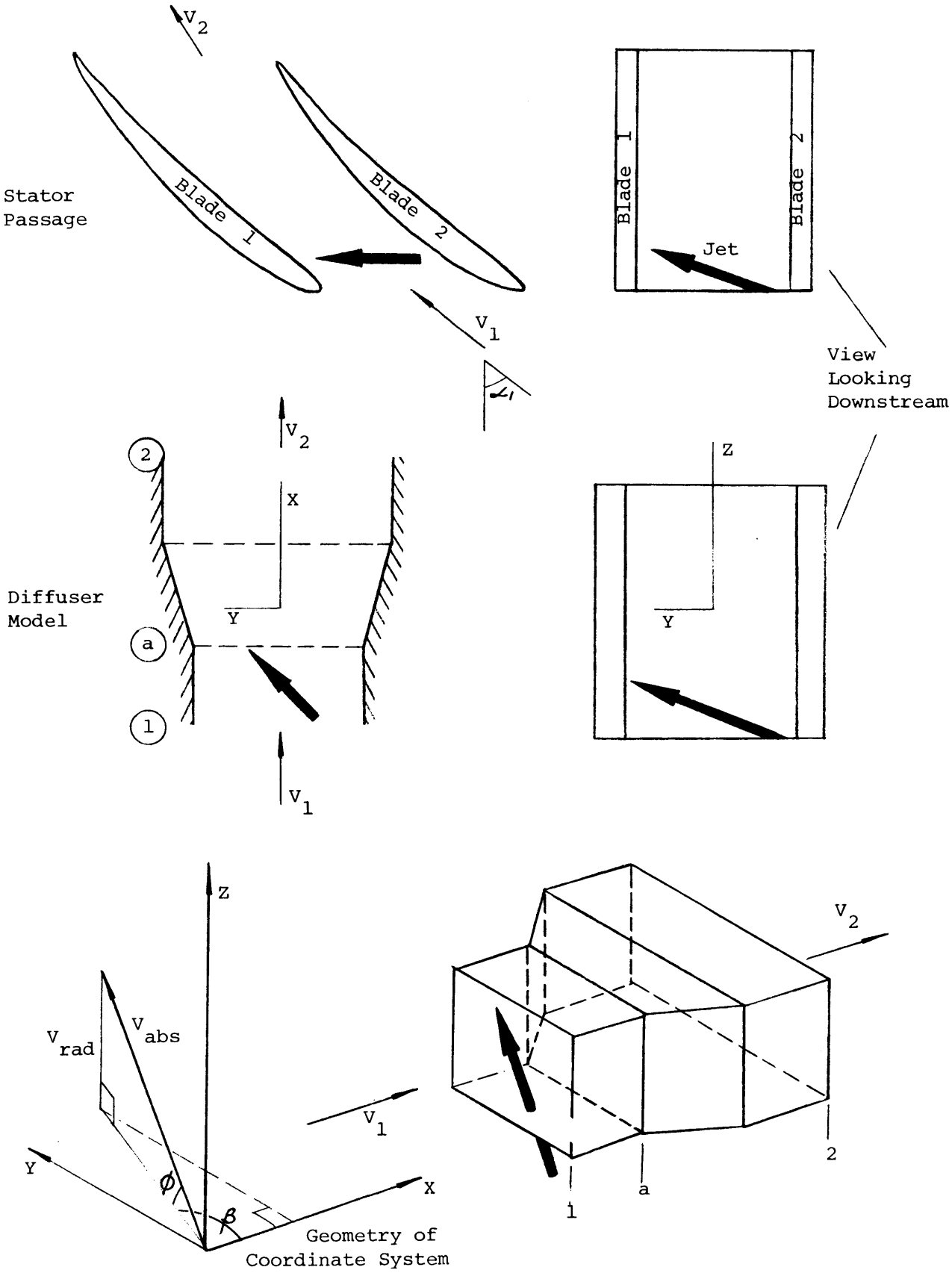

Figure B.1 Difusser Model and Coordinate System

APPENDIX C
VELOCITY ACQUISITION TECHNIQUE*

A single hotwire technique was used to obtain three-dimensional time-averaged velocity vectors. The technique is based on a similar technique presented by Wagner and Okishi [17]. Before the measurement technique can be discussed, some relationships linking probe geometry and hot-wire cooling velocities must be presented.

C.1 Probe Geometry

The hot-wire sensor, the probe coordinate system, pertinent geometry, and a general velocity vector are shown in Fig. 18. The coordinate system is fixed to the probe with the X-Z plane lying on the sensing portion of the probe and the probe axis, and with the Y-axis perpendicular to the X-Z plane and centered on the sensor. The wire is slanted an angle α_0 to the X-axis. The velocity vector V can be resolved into components along X, Y, and Z for each orientation of the wire. When the wire and coordinate system are rotated about the Z-axis, the yaw angle, θ_y, changes by the amount of turning, whereas the pitch angle, θ_p, remains the same. The conventions for θ_y and θ_p are presented in Fig. C.1. As can be seen, the pitch angle, which is the angle between the velocity vector and the X-Y plane, is positive when the velocity comes from below, and the yaw angle is positive when the velocity approaches from the left. The sensor angle, α, which is the pertinent angle for determining heat transfer from the wire, is defined as the angle between the unit slant vector, $\bar{A}$, and the velocity vector, $\bar{V}$. To obtain a relationship between α and α_0, θ_p, and θ_y, the dot product of the two vectors is taken:

$$\bar{A} = \cos\alpha_0 \bar{i} + \sin\alpha_0 \bar{k} \tag{C.1}$$

$$\bar{V} = -|V|\cos\theta_p \cos\theta_y \bar{i} + |V|\cos\theta_p \sin\theta_y \bar{j} + |V|\sin\theta_p \bar{k} \tag{C.2}$$

* This appendix is taken from [9] with minor modifications.

$$\bar{A}\cdot\bar{V} = |A||V|\cos(180-\alpha) = -|V|\cos\alpha_0\cos\theta_p\cos\theta_y + |V|\sin\alpha_0\sin\theta_p \quad (C.3)$$

$$\cos\alpha = \cos\alpha_0\cos\theta_p\cos\theta_y - \sin\alpha_0\sin\theta_p \quad (C.4)$$

C.2 Effective Cooling Velocity Ratio

The hot-wire anemometer output correlates to velocity as the output voltage to the fourth power. To make the signal more meaningful, it is linearized by a signal conditioner (linearizer). Therefore, the conditioned output, i.e., the output from the linearizer, is approximately proportional to the flow velocity. This linearized signal, E_L, is calibrated to velocity with the hot-wire sensor normal to the flow, i.e., the sensor angle, α, equal to 90 degrees. This yields

$$V = A_0 + A_1E_L + A_2E_L^2 \quad (C.5)$$

where V is the absolute fluid velocity and A_0, A_1, and A_2 are constants determined with a least squares curve fit. Whenever the probe is oriented to the flow at other than a sensor angle, 0, of 90°, the velocity calculated from Eq. (C.5) can be considered an effective velocity, V_e, where

$$V_e = A_0 + A_1E_L + A_2E_L^2 \quad (C.6)$$

The measurement technique used was based on knowing a precise relationship for the effective cooling velocity/absolute velocity ratio, V_e/V, for various orientations of the probe in the flow stream.

Experiments conducted by Schmidt and Okishi [18] showed this velocity ratio was strongly dependent on sensor angle, moderately dependent on pitch angle, and very weakly dependent on velocity, V, itself. Several correlations have been presented to describe V_e/V, however the present experiment used an extended correlation which yielded excellent results. The recommended

correlation is as follows:

$$\frac{V_e}{V} = B_0 + B_1\alpha + B_2\theta_p + B_3V + B_4\alpha^2 + B_5\theta_p^2 + B_6\alpha\theta_p + B_7\alpha V + B_8\theta_p V + B_9\alpha^3$$

$$+ B_{10}\theta_y + B_{11}\theta_y\theta_p + \frac{B_{12}\theta_y}{V^2} + B_{13}V^2\theta_p + \frac{B_{14}}{V\theta_p} \qquad (C.7)$$

The coefficients B_0 through B_{14} were determined, for each probe, from a least squares fit of the calibration data as described presently in Section C.5.

C.3 Measurement Technique

To obtain the velocity, three distinct measurements are required. The hot-wire was rotated about its axis to three different orientations as denoted in Fig. C.2. These probe positions relate to three different yaw angles, $\theta_{y,a}$, $\theta_{y,b}$, and $\theta_{y,c}$, which were set as indicated below.

$$\theta_{y,a} = \theta_y \qquad (C.8)$$

$$\theta_{y,b} = \theta_y + mb \qquad (C.9)$$

$$\theta_{y,c} = \theta_y + mc \qquad (C.10)$$

where mb and mc are probe turning angle increments from the a position. It should be emphasized that position a is the primary position, and it is relative to this position that the final θ_y and θ_p are determined. The values of mb and mc are chosen to orient the probe in a position that suits that probe's calibration. For the present experiment, a probe slant angle of 0 degrees was used and it was found that, for this case, values of mb and mc of 30° and -30° respectively worked well. For each orientation of the probe, the anemometer output voltage is measured, and two equations like (C.4) and (C.7) are obtained. Therefore, each physical location generates three sets of equations. These equations are:

For position a:

$$\cos\alpha_a = \cos\alpha_0\cos\theta_p\cos\theta_{y,a} - \sin\alpha_0\sin\theta_p \tag{C.11}$$

$$\frac{V_e}{V} = B_0 + B_1\alpha_a + B_2\theta_p + B_3V + B_4\alpha_a^2 + B_5\theta_p^2 + B_6\alpha_a\theta_p + B_7\alpha_aV + B_8\theta_pV + B_9\alpha_a^3$$
$$+ B_{10}\theta_{y,a} + B_{11}\theta_{y,a}\theta_p + \frac{B_{12}\theta_{y,a}}{V^2} + B_{13}V^2\theta_p + \frac{B_{14}}{V\theta_p} \tag{C.12}$$

For position b:

$$\cos\alpha_b = \cos\alpha_0\cos\theta_p\cos\theta_{y,b} - \sin\alpha_0\sin\theta_p \tag{C.13}$$

$$\frac{V_e}{V} = B_0 + B_1\alpha_b + B_2\theta_p + B_3V + B_4\alpha_b^2 + B_5\theta_p^2 + B_6\alpha_b\theta_p + B_7\alpha_bV + B_8\theta_pV + B_9\alpha_b^3$$
$$+ B_{10}\theta_{y,b} + B_{11}\theta_{y,b}\theta_p + \frac{B_{12}\theta_{y,b}}{V^2} + B_{13}V^2\theta_p + \frac{B_{14}}{V\theta_p} \tag{C.14}$$

For position c:

$$\cos\alpha_c = \cos\alpha_0\cos\theta_p\cos\theta_{y,c} - \sin\alpha_0\sin\theta_p \tag{C.15}$$

$$\frac{V_e}{V} = B_0 + B_1\alpha_c + B_2\theta_p + B_3V + B_4\alpha_c^2 + B_5\theta_p^2 + B_6\alpha_c\theta_p + B_7\alpha_cV + B_8\theta_pV + B_9\alpha_c^3$$
$$+ B_{10}\theta_{y,c} + B_{11}\theta_{y,c}\theta_p + \frac{B_{12}\theta_{y,c}}{V^2} + B_{13}V^2\theta_p + \frac{B_{14}}{V\theta_p} \tag{C.16}$$

By substituting Eqs. (C.8), (C.9), and (C.10) into (C.12), (C.14), and (C.16), the six unknown variables α_a, α_b, α_c, θ_p, θ_y, and V remain in the six equations, (C.11) through (C.16). These equations were solved simultaneously, as will be described presently in Section C.4. The three-dimensional vector is completely described with the variables θ_p, θ_y, and V known relative to orientation a.

The procedure for arriving at the primary position a is an important one. First, the probe is inserted in some known position called the insertion

position. The insertion position, which is shown in Fig. C.2, is at an orientation such that the hot-wire sensor aligns in the traverser operating plane, which is shown in Fig. 16. From this orientation, the probe is turned some angle, called the twist angle, to orient the probe into the velocity vector. This twist angle is determined by monitoring the output of the hot-wire anemometer. When the anemometer output is at a minimum that indicates the probe is headed into the flow (θ_y=0), that location fixes the twist angle. From the discussions above, it is clear that position a is at an orientation that aligns the sensing wire into the flow and is an angle θ_t away from the insertion position. In practice, it was found that position a didn't need to align exactly into the flow and that one setting of the twist angle would do for a whole region of the flow field.

C.4 Velocity Transformation

Once the values of θ_y, θ_p, and V are determined at a given location, the three-dimensional velocity vector is known in the probe coordinates (see Fig. 18). To relate this to the velocity vector in compressor coordinates, a rather involved velocity transformation is required. This transformation involves several rotations of the coordinate system about certain axes and results, as would be expected, in a series of matrix multiplications where the components of the matrices are trigonometric functions of certain angles.

To begin with, define the velocity in probe coordinates as (V_x, V_y, V_z) with values given by

$$V_x = -V\cos(\theta_p)\cos(\theta_y)$$

$$V_y = V\cos(\theta_p)\sin(\theta_y)$$

$$V_z = V\sin(\theta_p)$$

Then, the velocity in compressor coordinates is given by Table C.1.

This equation is, of course, programmed into a data reduction program

where the transformation is done automatically.

C.5 Calibration Procedure

As mentioned previously, there are two parts to the calibration procedure, the calibration of effective velocity, V_e, versus linearizer output, E_L, and the calibration of V_e/V for a range of pitch angle, yaw angle, and velocity. The former is referred to as the linear calibration (since V_e is approximately linear with E_L) and the latter is called the directional calibration. In each calibration, the air is supplied by a compressor and is delivered to a calibration nozzle. This nozzle generates a controllable jet of air which is used for calibration.

To perform the linear calibration, which is relatively easy, one inserts the probe into the calibration jet at a yaw angle of 90°. This yields a sensor angle of 90°. Then the jet velocity is adjusted to different values and the output voltage recorded. Typically, twenty points are sufficient and the velocity is curve fitted with a second-order equation as given in Eq. (C.6).

The calibration for V_e/V is much more demanding. In this case, the jet absolute velocity V is kept constant while the wire is rotated to various orientations. The positioning of the wire is done in a systematic way. First, the pitch angle is fixed, then the yaw angle is varied from -60 to +60 degrees in increments of 10. For each yaw angle, the linearizer output is recorded. This procedure is repeated for a range of pitch angles, thus yielding output voltages for a matrix of pitch and yaw angles for that preset velocity. The entire procedure is then repeated for a second velocity. The two calibration velocities are chosen to represent the range of velocities expected in the actual experiment. Finally, all the data is used to generate a least squares curve fit in Eq. (C.7). This curve fit generates the coefficients B_0 - B_{14}.

In practice, it was found that particles in both the injection air and the hot-wire calibration jet were detrimental to the hot wire at high velocities. Consequently, to prevent breakage of the hot wire, calibration velocities were limited to within 270 ft/sec.

The choice of pitch angles used in the above calibration is a crucial one. As mentioned previously, different probes with different slant angles, α_0, have different ranges of calibration. In general, the minimum pitch angle cannot position the probe such that the short prong is obstructing the oncoming flow. Therefore, for a probe with α_0=45, the minimum pitch angle is -45 and, for a probe with α_0=0, the minimum pitch angle is 0. The maximum pitch angle is determined by looking at calibration data. To illustrate this, consider Figs. C.3 and C.4. Figure C.3 presents a typical calibration curve for a wire with α_0=0, and Fig. C.4 presents a typical calibration curve for α_0=45. In each figure, the points represent calibration data and the solid lines are the curve fit. There are several important points to be observed in the plots. To begin with, each probe has a totally different range of pitch angles over which it is useful. For the probe with α_0=0, which is what was needed for the present experiment, the range is +10 to +60 (actually the upper limit could easily be extended to +70) and, for the probe with α_0=45, the range of pitch angles is -30 to +20 (actually the calibration could have extended from -40 to +30). Therefore, one has to choose a probe that has a calibration range that is suited to his experiment. Another item to notice is that the probe with α_0=0 has a more limited range of yaw angles than does the probe with α_0=45. Lastly, since the probe with α_0=0 has larger spaces between successive pitch angles (for yaw angle equal to zero), it has greater pitch angle resolution.

C.6 Data Acquisition and Reduction

There are a few points that should be considered when taking the hot-wire data. Firstly, the linear calibration mentioned above may drift with time so that each time before data is taken, this calibration must be set. This precaution is not necessary for the directional calibration because it is expressed as a ratio V_e/V and is only a function of probe geometry. Secondly, the anemometer controls should be checked before each data acquisition session. This includes checking the bridge resistance, the linearizer coefficients, the zero offset and the span.

In the present experiment, all data was stored in direct access memory for later reduction. This reduction, which involves the solution to the six non-linear equations (C.11) through (C.16), was accomplished by a numerical root-solving routine.

TABLE C.1
VELOCITY TRANSFORMATION

$$\begin{Bmatrix} V_\theta \\ V_r \\ V_z \end{Bmatrix} = \begin{bmatrix} \cos(\theta_{Pr}-\theta_0) & -\sin(\theta_{Pr}-\theta_0) & 0 \\ -\sin(\theta_{Pr}-\theta_0) & -\cos(\theta_{Pr}-\theta_0) & 0 \\ 0 & 0 & 1 \end{bmatrix} \begin{bmatrix} 1 & 0 & 0 \\ 0 & \cos\theta_B & \sin\theta_B \\ 0 & -\sin\theta_B & \cos\theta_B \end{bmatrix}$$

$$\begin{bmatrix} \cos\phi & 0 & \sin\phi \\ 0 & 1 & 0 \\ -\sin\phi & 0 & \cos\phi \end{bmatrix} \begin{bmatrix} \cos\theta_t & \sin\theta_t & 0 \\ -\sin\theta_t & \cos\theta_t & 0 \\ 0 & 0 & 1 \end{bmatrix} \begin{Bmatrix} V_x \\ V_y \\ V_z \end{Bmatrix}$$

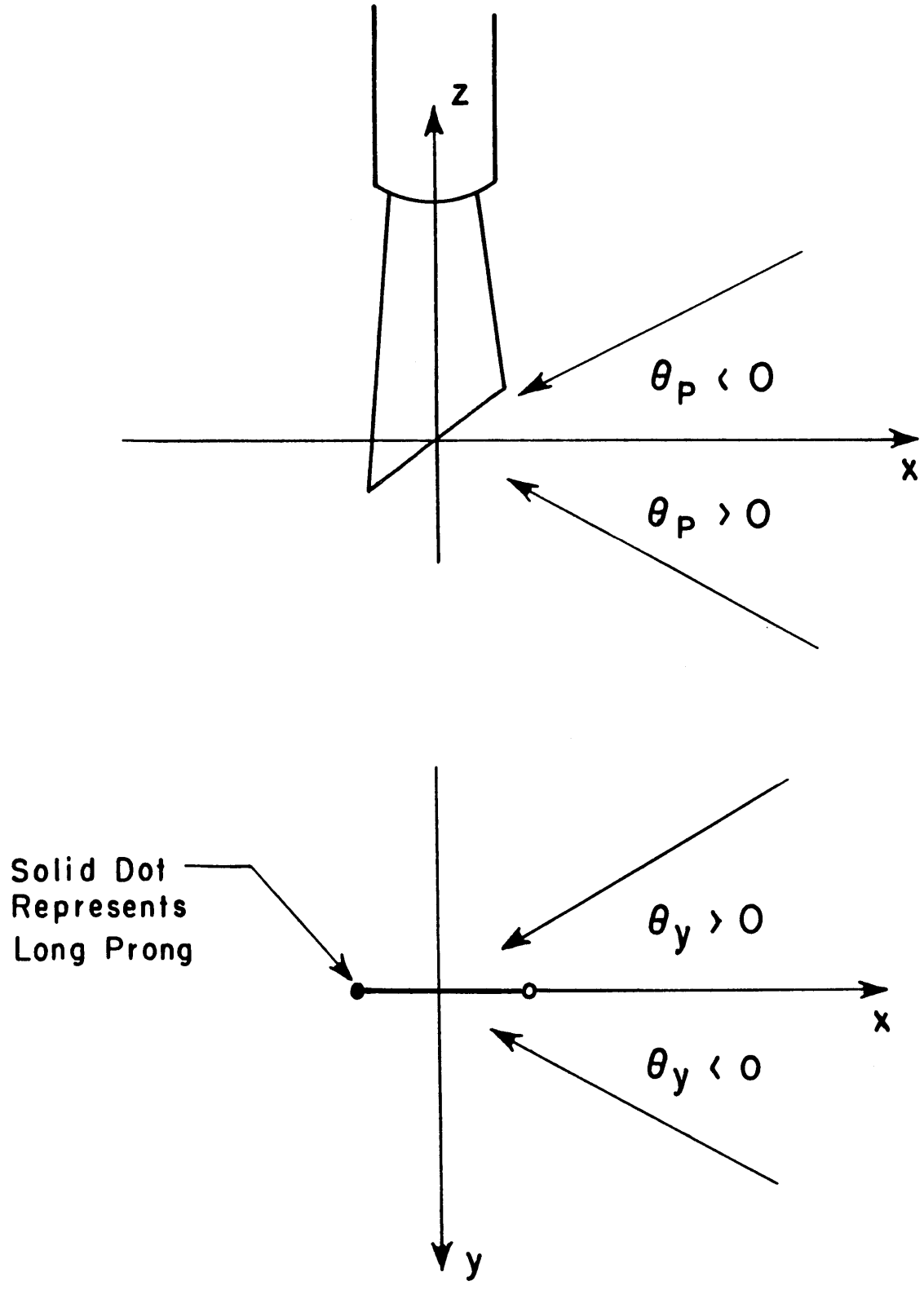

Fig. C.1: Conventions for pitch and yaw angles

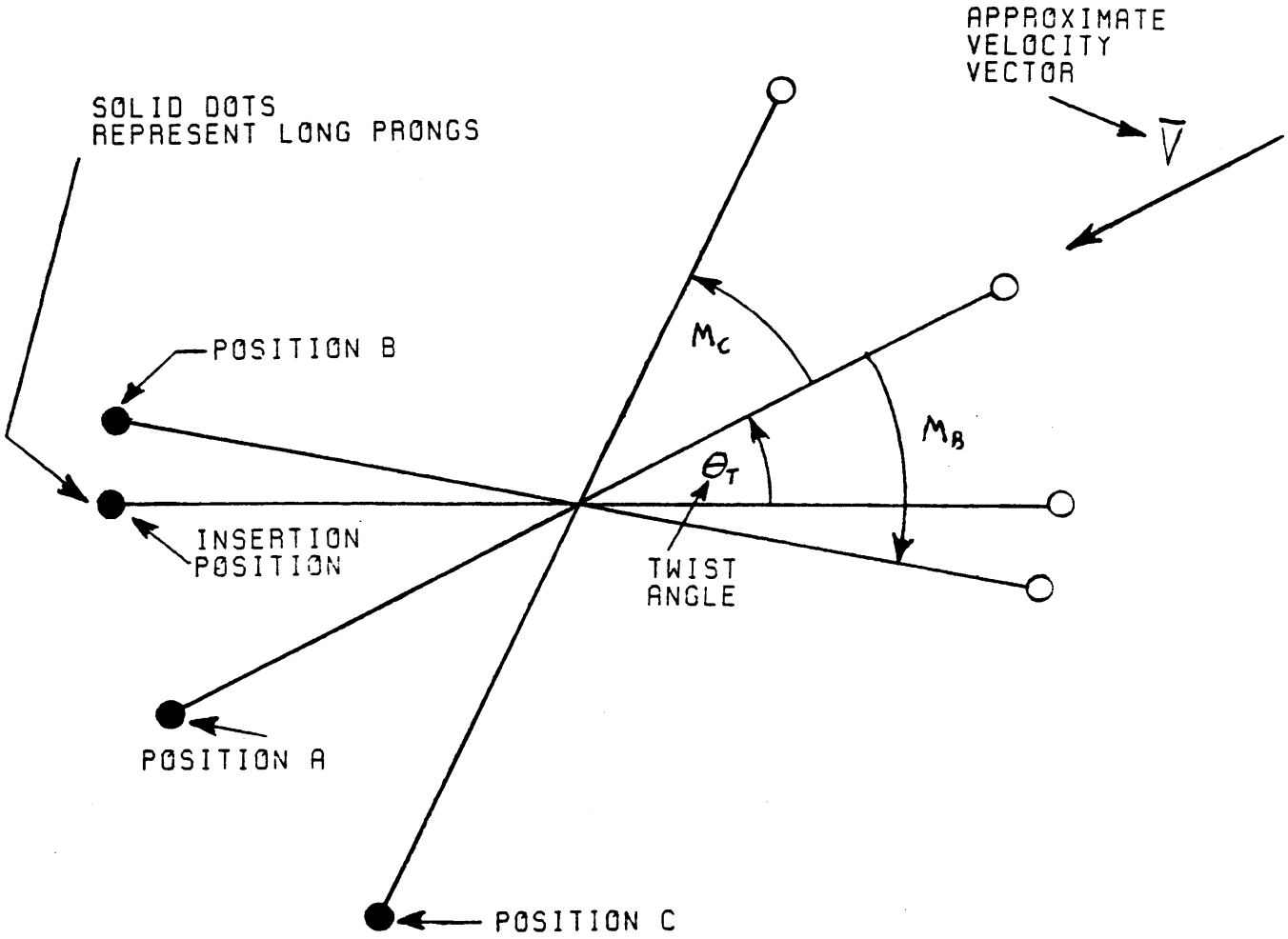

Fig. C.2: Different orientations of the hotwire

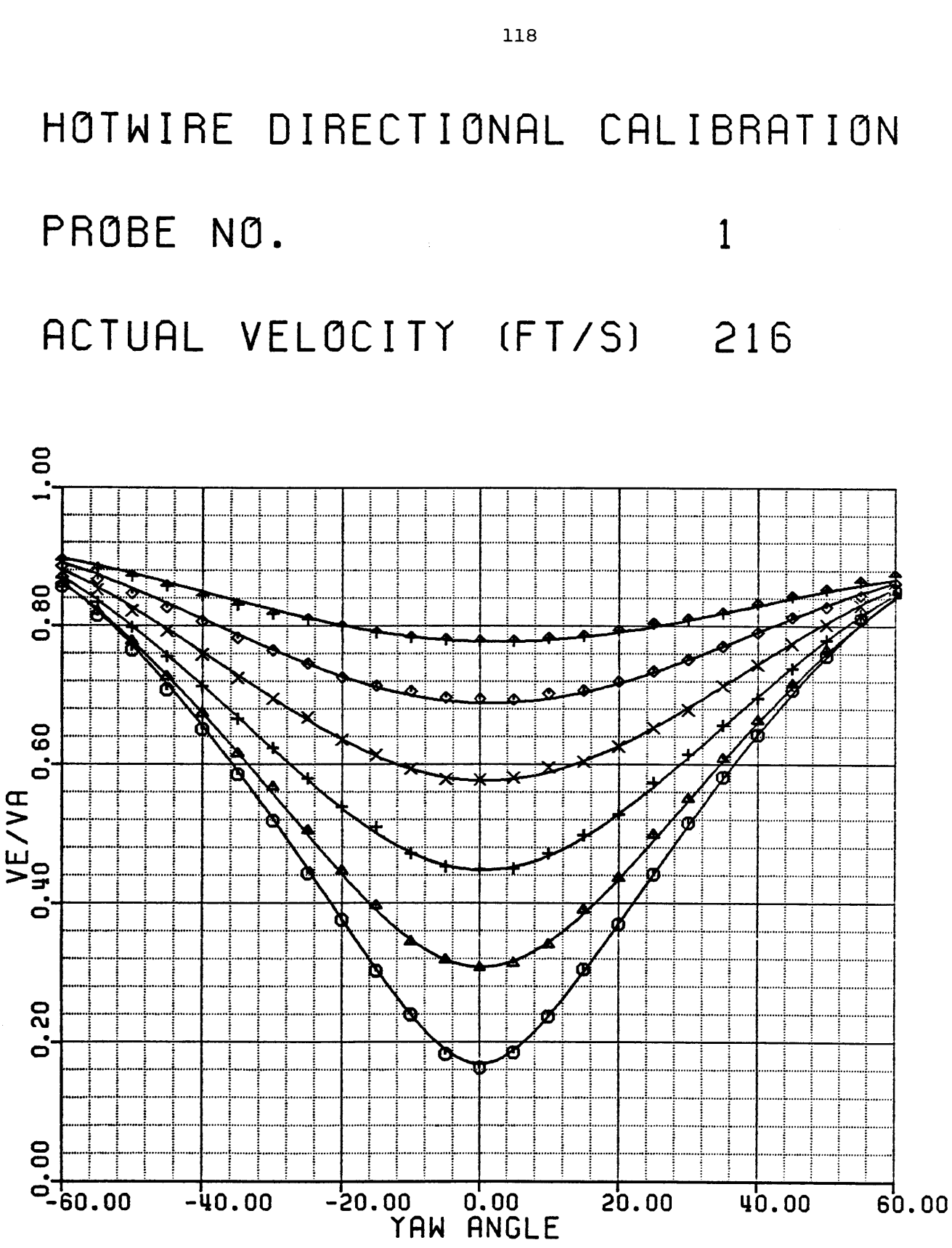

Fig. C.3: Typical directional calibration for 0° of slant

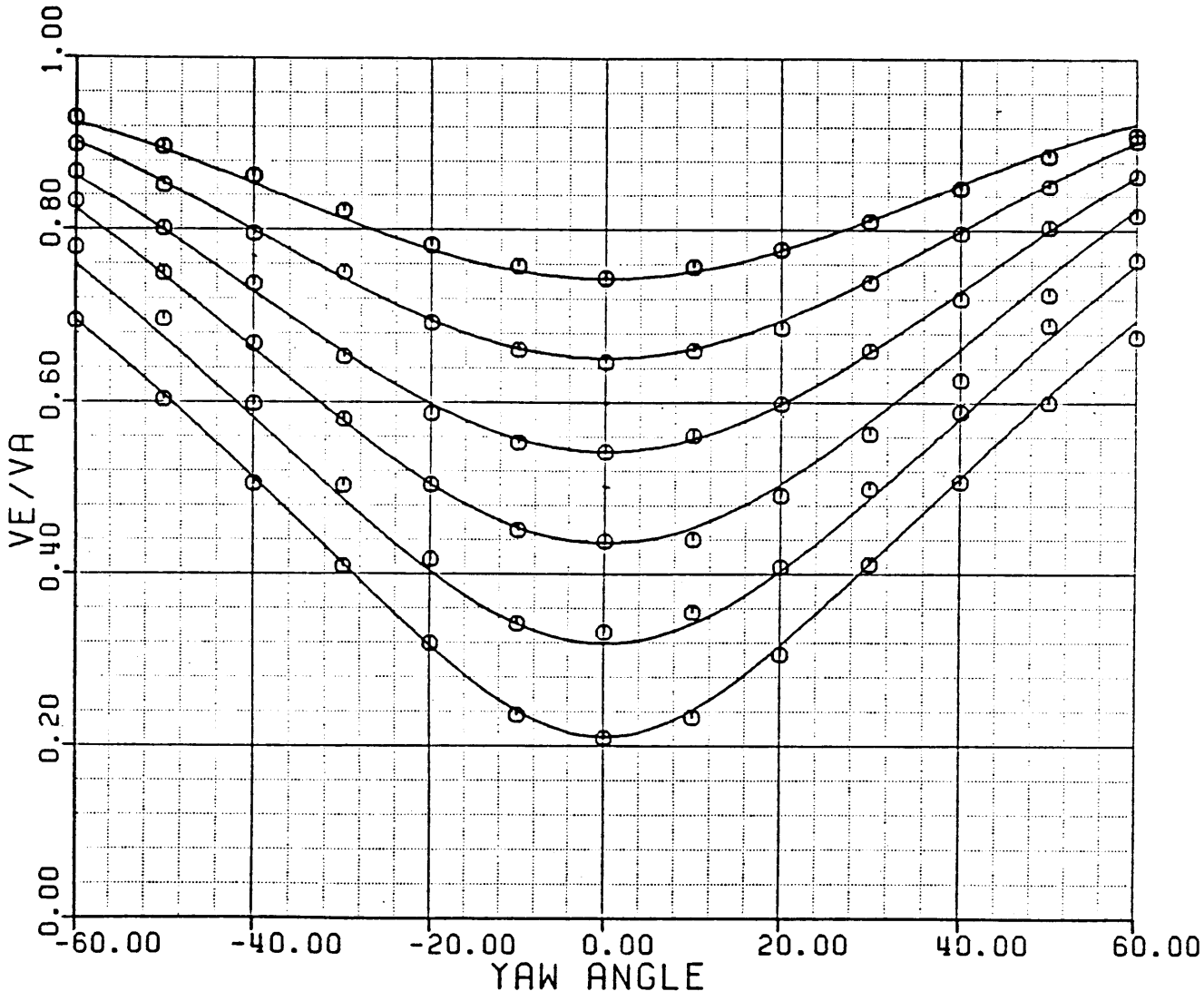

Fig. C.4: Typical directional calibration for 45° of slant

APPENDIX D
CALCULATION OF MOMENTUM INFLUX FOR ANY GIVEN MASS INJECTION RATE

Nomenclature

D	Diameter of hub
$\dot{m}_j$	Overall mass injection rate
M_t	Total flux of momentum injection per rotor passing
$\hat{s}$	Unit vector in the direction of the main flow at a flow coefficient of 0.342
V_{absj}	Jet velocity in the stator reference frame
V_{hub}	Hub velocity
V_{rad}	Radial velocity measured at a stationary point close to the rotating hub surface
V_{radj}	Radial velocity of each jet
V_{relj}	Jet velocity relative to the moving hub
β	Angle jet makes with the OXY plane
θ	Angle between the component of the jet in the OXY plane and the x-axis
ρ	Density of air
σ	Ratio of open area to hub surface area
ℓ	Length of slots (in z direction)

This appendix contains an analysis that estimates the amount of momentum flux injected into the blade passage for a given mass injection rate. Results are used to generate Figs. 43, 44, and 45.

Figure D.1 shows the time variation of V_{rad}, the radial velocity, at a point close to the hub surface in the stationary reference frame. $V_{rad} = V_{radj}$ corresponds to the passing of a jet. Now for each jet, the relative and absolute velocity vectors are

$$\underset{\sim}{V}_{relj} = \frac{V_{radj}}{\tan\theta}\,\underset{\sim}{i} + V_{radj}\,\underset{\sim}{j} + \frac{V_{radj}\tan\beta}{\sin\theta}\,\underset{\sim}{k} \tag{D.1}$$

$$\underset{\sim}{V}_{absj} = \left(V_{hub} + \frac{V_{radj}}{\tan\theta}\right)\underset{\sim}{i} + V_{radj}\,\underset{\sim}{j} + \frac{V_{radj}\tan\beta}{\sin\theta}\,\underset{\sim}{k}$$

All angles are defined in Fig. D.2. The total amount of momentum flux injected into the stator passage at any instant is

$$\underset{\sim}{M}_t = \int \rho \, \underset{\sim}{V}_{absj} (\underset{\sim}{V}_{absj} \cdot \underset{\sim}{dA})$$

$$= \dot{m}_j \, \underset{\sim}{V}_{absj} \tag{D.2}$$

Assuming a uniform jet velocity,

$$V_{radj} = \frac{\dot{m}_j}{\rho \pi D \sigma \ell} \tag{D.3}$$

So Eqs. (D.1), (D.2), and (D.3) give $\underset{\sim}{M}_t$ as a function of σ, ℓ, $\dot{m}_j$, and β.

$\underset{\sim}{M}_t$ is the total, or absolute, momentum influx. Its component in the streamwise direction is simply $\underset{\sim}{M}_t \cdot \hat{\underset{\sim}{s}}$, where $\hat{\underset{\sim}{s}}$ is a unit vector in the direction of the main flow at the location of injection.

In this calculation, the main flow is assumed to turn linearly from inlet to exit in the -z direction and the inlet and exit angles are those at the flow coefficient of 0.342. With these approximations, $\hat{\underset{\sim}{s}} = \sin\alpha \underset{\sim}{i} - \cos\alpha \underset{\sim}{k}$ can be calculated, where α is the angle betwen the main flow and the compressor axis, as shown in Fig. D.2.

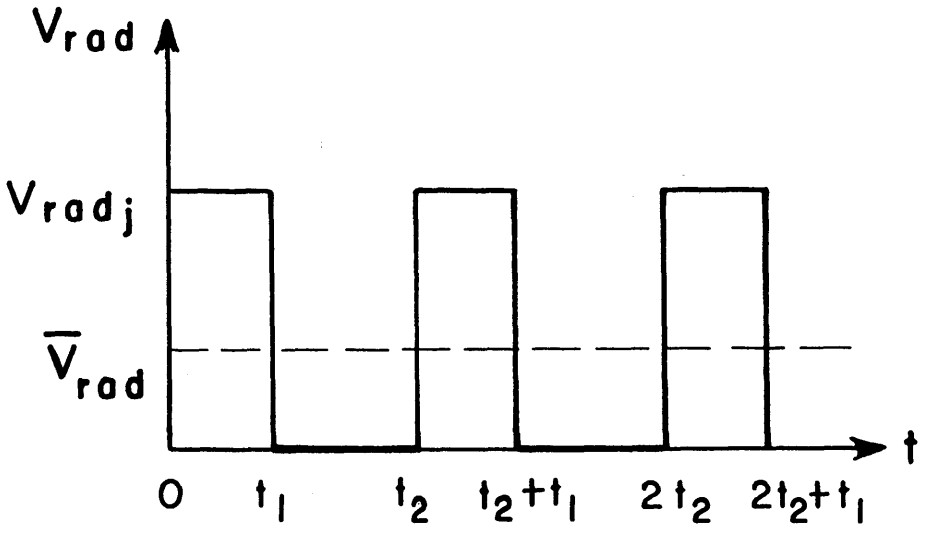

- V_{radj} is radial velocity of each jet
- $\overline{V}_{rad}$ is time-averaged radial velocity as seen by the hotwire
- t_2 is the period of jet passing
- $t_1 = \sigma t_2$ is the duration of each jet

Fig. D.1: Variation of radial velocity with time at a point close to the hub surface

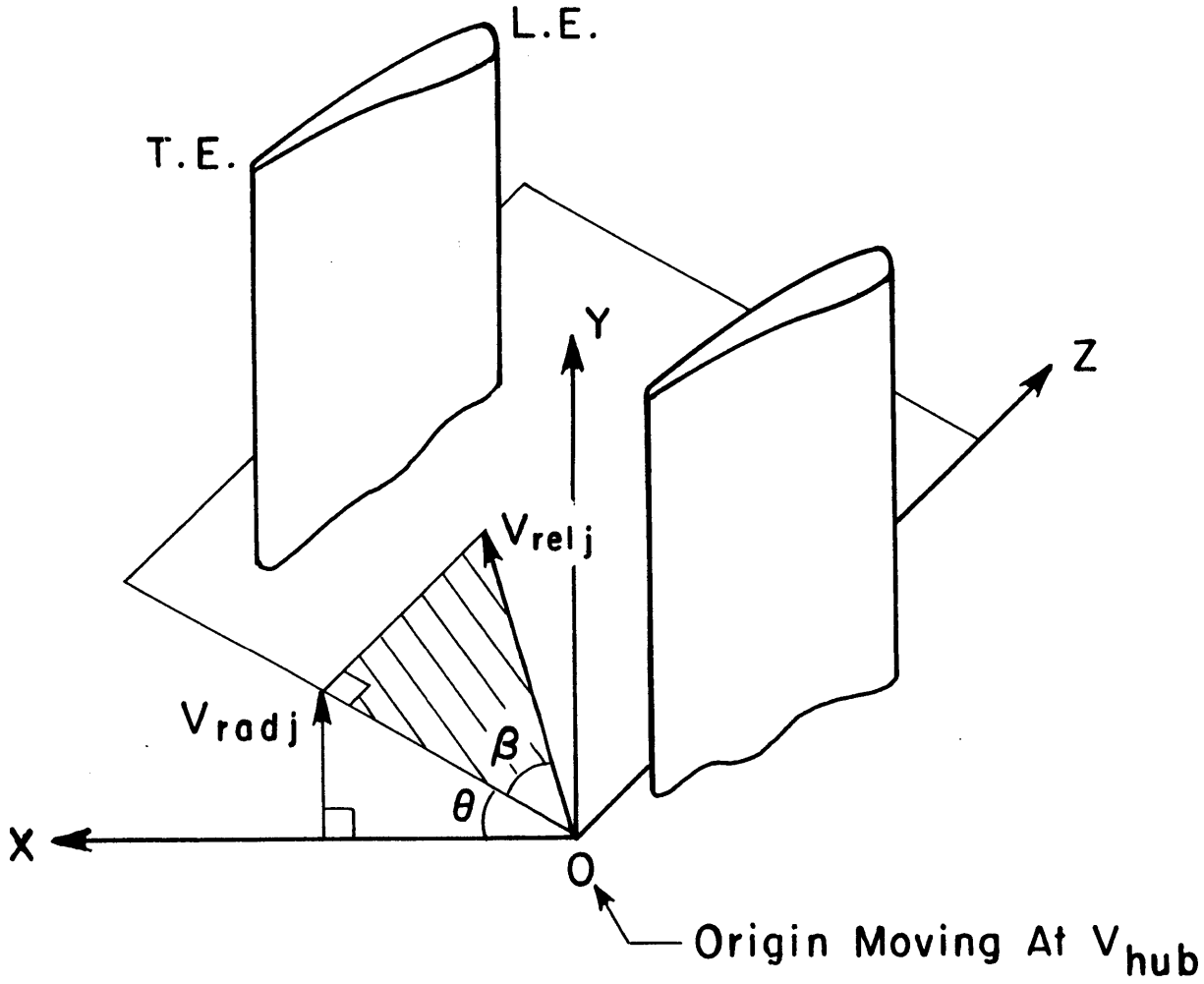

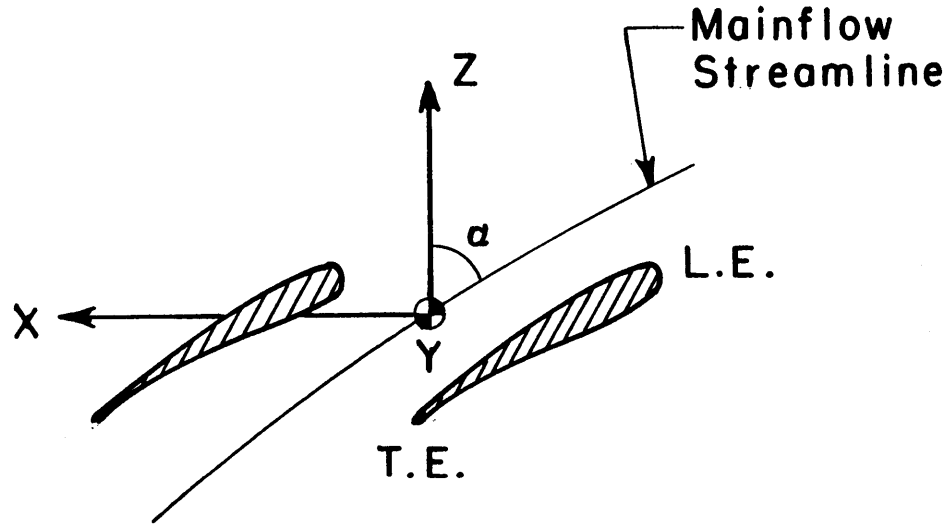

Fig. D.2: Coordinate system, OXYZ, moving at velocity V_{hub} past stator blades